

Charles University in Prague
Faculty of Mathematics and Physics

DOCTORAL THESIS



Mgr. Andrii Rednyk

**High pressure CO and methanol oxidation study over
nanopowders Rare Earth Oxides and platinum thin film
catalysts**

Department of Surface and Plasma Science

Supervisor of the doctoral thesis: Prof. RNDr. Vladimír Matolín, DrSc.

Prague 2016

Acknowledgements

Firstly, I would like to express my sincere gratitude to my supervisor Prof. RNDr. Vladimír Matolín DrSc. for the continuous support of my study and related research, for his patience, motivation, and immense knowledge. Besides my supervisor, I would also like to thank my consultant Doc. RNDr. Iva Matolínová Dr. for useful advises.

My sincere thanks, also goes to RNDr. Viktor Johánek PhD, Mgr. Michal Václavů, Mykhailo Vorokhta PhD, Ivan Khalakhan PhD, Mgr. Andrii Tovt, Mgr. Stefan Wild and Björn Neumann PhD - without they precious support it would not be possible to conduct this research. Furthermore, I would like to thank all my colleagues who warmly accepted me in their surface science team. Last but not the least, I would like to thank my family: my mother and my brother for supporting me spiritually throughout writing this thesis and my life in general.

I declare that I carried out this doctoral thesis independently, and only with the cited sources, literature and other professional sources.

I understand that my work relates to the rights and obligations under the Act No. 121/2000 Sb., the Copyright Act, as amended, in particular the fact that the Charles University in Prague has the right to conclude a license agreement on the use of this work as a school work pursuant to Section 60 paragraph 1 of the Copyright Act.

In..... date.....

signature

Název práce: *Studium oxidace CO a metanolu za vysokého tlaku na katalyzátorech ve formě nanoprášků oxidů kovů vzácných zemin a tenkých vrstev na bázi platiny*

Autor: *Mgr. Andrii Rednyk*

Katedra / Ústav: *Katedra fyziky povrchů a plazmatu*

Vedoucí doktorské práce: *Prof. RNDr. Vladimír Matolín, DrSc.
matolin@mbox.troja.mff.cuni.cz*

Abstrakt:

Tato práce se zaměřuje na studium katalytické aktivity oxidů kovů vzácných zemin (REO) ve formě nanoprášků a tenkých vrstev na bázi platiny s využitím mikroreaktoru s vysokotlakou reakční komorou. Nanočástice REO byly připraveny novým přístupem založeným na sol-gelové chemické metodě. Tenkovrstvé vzorky byly připraveny magnetronovým naprašováním.

V první části je studována reakce oxidace oxidu uhelnatého (CO oxidation) na REO a na tenkých vrstvách Pt, PtO_x. Z připravených nanopráškových oxidů kovů vzácných zemin vykazují velmi dobrou aktivitu oxidy ceru stabilizované aluminou, hlavně z důvodu většího aktivního povrchu. Vrstvy Pt i PtO_x deponované na křemíkové podložky vykazují srovnatelnou aktivitu. Když se jako podložka použije uhlík (grafitová folie nebo uhlíková mezivrstva), aktivita Pt vrstvy poklesne, kdežto PtO_x si zachovává vysokou aktivitu.

Obsahem druhé části je parní reformace metanolu (SRM) a částečná oxidace metanolu (POM) s katalyzátory na bázi tenkých vrstev s obsahem platiny. Ukazuje se, že tenké vrstvy PtO_x vykazují mnohem větší aktivitu než ostatní vzorky se stejnou tloušťkou. Důvodem je redukce oxidů platiny na kovovou platinu (Pt⁴⁺ → Pt⁰). Vysoká aktivita při reakci POM byla demonstrována také s 1 nm silnou vrstvou Pt-CeO₂. Přítomnost stopového množství oxidů ceru v takové vrstvě je klíčovým faktorem ve formaci zrnité povrchové struktury, která vede k větší aktivitě a stabilitě katalyzátoru.

Klíčová slova: *CO oxidace, oxidace metanolu, REO, oxid platiny.*

Title: *High pressure CO and methanol oxidation study over nanopowder Rare Earth Oxides and platinum thin film catalysts*

Author: *Mgr. Andrii Rednyk*

Department: *Department of Surface and Plasma Science*

Supervisor: *Prof. RNDr. Vladimír Matolín, DrSc.
matolin@mbox.troja.mff.cuni.cz*

Abstract:

This doctoral thesis focuses on reactivity study of nanopowder rare earth oxides (REOs) and platinum based thin film catalysts using microreactor with high pressure reaction cell. REOs nanoparticles were prepared by new approach based on sol-gel chemistry. Magnetron sputtering technique was used for preparation of thin film samples.

In the first part of the thesis CO oxidation on REOs and on Pt, PtO_x thin films were performed. Among prepared REOs catalyst better activity exhibited alumina stabilized ceria, due to higher surface area. Both Pt and PtO_x deposited on silicon substrate exhibited similar activity. When carbon (G-foil or C interlayer) is used as support, activity of Pt thin film decreases while PtO_x preserves high activity.

In the second part of the thesis steam reforming of methanol (SRM) and partial oxidation of methanol (POM) were performed on Pt thin films. It was shown that PtO_x thin film exhibited superior activity compared to other samples with the same thickness. It is due to the reduction of platinum oxide to metallic platinum (Pt⁴⁺ → Pt⁰). Also high POM activity was demonstrated by 1 nm thick Pt-CeO₂ thin film. Presence of trace amount of ceria in such layer has been found to be a key factor in formation of granular surface structure, resulted in better activity and stability of such catalyst.

Keywords: *CO oxidation, methanol oxidation, REOs, platinum oxide.*

Preface

The present doctoral thesis is based on experimental work carried out at the Department of Surface and Plasma Science of Charles University in Prague and at the Institute of Applied and Physical Chemistry, University of Bremen, Germany. The main results presented in this work are based on the following original publications, which are already published or will be published soon:

1. B. Neumann, T. M. Gesing, A. Rednyk, V. Matolín, A. E. Gash, and M. Bäumer, “Sol–gel preparation of alumina stabilized rare earth areo- and xerogels and their use as oxidation catalysts,” *J. Colloid Interface Sci.*, vol. 422, pp. 71–78, 2014.
2. A. Rednyk, V. Johánek, I. Khalakhan, M. Dubau, M. Vorokhta, V. Matolín, “Methanol oxidation on sputter-coated platinum oxide catalyst”, *International Journal of Hydrogen Energy*, vol. 41, pp. 265-275, 2016.
3. A. Rednyk, V. Johánek, A. Ostroverkh, V. Matolín, “Methanol oxidation on platinum oxide thin film catalyst: influence of various methanol to oxygen molar ratios”, will be submitted (2016).
4. A. Ostroverkh, V. Johánek, A. Rednyk, P. Kúš, R. Pavlíková, V. Matolín, “Methanol oxidation on ceria-platinum inverse catalyst”, will be submitted (2016).

The following is a list of papers (already published or will be published soon) and patent in which Mgr. Andrii Rednyk is a co-author:

5. R. Fiala, M. Vaclavu, A. Rednyk, I. Khalakhan, M. Vorohta, J. Lavkova, V. Potin-Heurtaux, I. Matolínova, and V. Matolín, “Pt-CeO_x thin film catalysts for PEMFC” *Catalysis today*, vol. 240 (part B), pp. 236-241, 2015.
6. R. Fiala, A. Figueroba, A. Bruix, M. Vaclavu, A. Rednyk, I. Khalakhan, M. Vorokhta, J. Lavkova, F. Illas, V. Potin, I. Matolínova, K. Neyman, V. Matolín, “High efficiency Pt²⁺-CeO₂ novel thin film catalyst as anode for proton exchange membrane fuel cells”, submitted to *Applied Catalysis B: Environmental*, 2015.

7. I. Bieloshapka, P. Jiricek, M. Vorokhta, A. Rednyk, K. Jurek, M. Perekrestov, E. Uktaintsev, B. Lesiak, “Analysis of thin films Pd-catalysts prepared for DFAFC”, submitted to *Applied Surface Science*, 2015.

8. Japanese Patent applications:

T. Mori, A. Rednyk and A. Suzuki, “Anode of solid oxide fuel cells, its fabrication process and solid oxide fuel cell device”, filing number 2015-119900, pp. 1 - 14, supplement including figures pp. 1 - 4, 2015.

Contents

1. Goals, objectives and structure of the thesis.....	1
2. Description of the used experimental techniques.....	2
2.1. Magnetron sputtering technique.....	2
2.2. X-ray photoelectron spectroscopy (XPS).....	3
2.3. Scanning electron microscopy (SEM).....	6
2.4. Microreactor system.....	8
3. CO oxidation.....	13
3.1. Motivation	13
3.2. CO oxidation mechanisms.....	14
3.3. CO oxidation on Pt thin film catalysts.....	17
3.4. CO oxidation on rare earth oxides (REOs) nanoparticles.....	27
3.5. CO oxidation on samaria nanoparticles.....	33
4. Methanol oxidation	40
4.1. Motivation.....	40
4.2. Steam reforming of methanol (SRM).....	42
4.2.1. SRM on Pt, PtO _x and Pt-CeO ₂ thin film catalyst.....	43
4.3. Partial oxidation of methanol (POM).....	49
4.3.1. POM on PtO _x and Pt thin film catalysts.....	50
4.3.2. POM on PtO _x deposited on carbonaceous interlayers.....	56
4.3.3. POM on PtO _x under different methanol to oxygen molar ratios.....	62
4.3.4. POM on Pt-CeO ₂ layers with different Pt loading	68
4.3.5. POM on very thin Pt/CeO ₂ , Pt-CeO ₂ and Pt layers.....	74
5. Conclusions.....	83
Bibliography.....	86
List of Tables.....	93
List of Abbreviations.....	94

1. Goals, objectives and structure of the thesis

The thesis is focused on the experimental study of two important chemical reactions: oxidation of CO and methanol oxidation over REOs nanopowders and platinum thin film catalysts. Such reactions were investigated at high pressure conditions using special home-made laboratory microreactor system. The design of microreactor allows us to perform activity tests on catalysts, which are either in form of nanopowders or thin film samples. X-ray photoelectron spectroscopy (XPS) and scanning electronic microscopy (SEM) techniques were used for chemical composition and morphology investigation of samples at different stages of the reaction (before, during and after the reaction).

The content of this thesis is divided into five chapters. Thesis starts from short explanations of goals, objectives and structures (*Chapter 1*). The *Chapter 2* gives brief description of used experimental techniques in this work. Investigation of CO oxidation on powder and thin film samples are described in *Chapter 3*, which is divided into five subchapters. It starts from motivation (3.1) followed by CO oxidation mechanisms (3.2), where general aspects of CO oxidation process are described. In the following subchapters we showed experimental results: investigations of CO oxidation on platinum thin film catalyst (3.3), on REOs nanoparticles (3.4) and on samaria nanoparticles made from different precursors (3.5). *Chapter 4* is devoted to methanol oxidation study on platinum thin film catalysts. This chapter has three parts: motivation (4.1), steam reforming of methanol (4.2) and partial oxidation of methanol (4.3). In subchapter 4.2.1 the experimental results obtained from SRM on Pt, PtO_x and Pt-CeO₂ thin films are described. Subchapter 4.3.1 describes POM study on PtO_x and Pt thin films. The POM on PtO_x deposited on carbonaceous interlayers, PtO_x under different methanol to oxygen molar ratios, Pt-CeO₂ with different Pt loading and very thin Pt/CeO₂, Pt-CeO₂ and Pt layers are described in subchapters 4.3.2 - 4.3.5. In the last *Chapter 5* summary and conclusions of the thesis are shown.

2. Description of the used experimental technique

2.1. Magnetron sputtering technique

Magnetron sputtering has developed rapidly over the last decade and becomes one of leading processes for the sputtering of a large variety of materials with a precious control over film thickness and uniformity for industrial and laboratory needs [1]. During the conventional sputtering process (*Fig. 1a*), ions of working gas (usually Argon) out of plasma, are accelerated toward to the target material and bombard it.

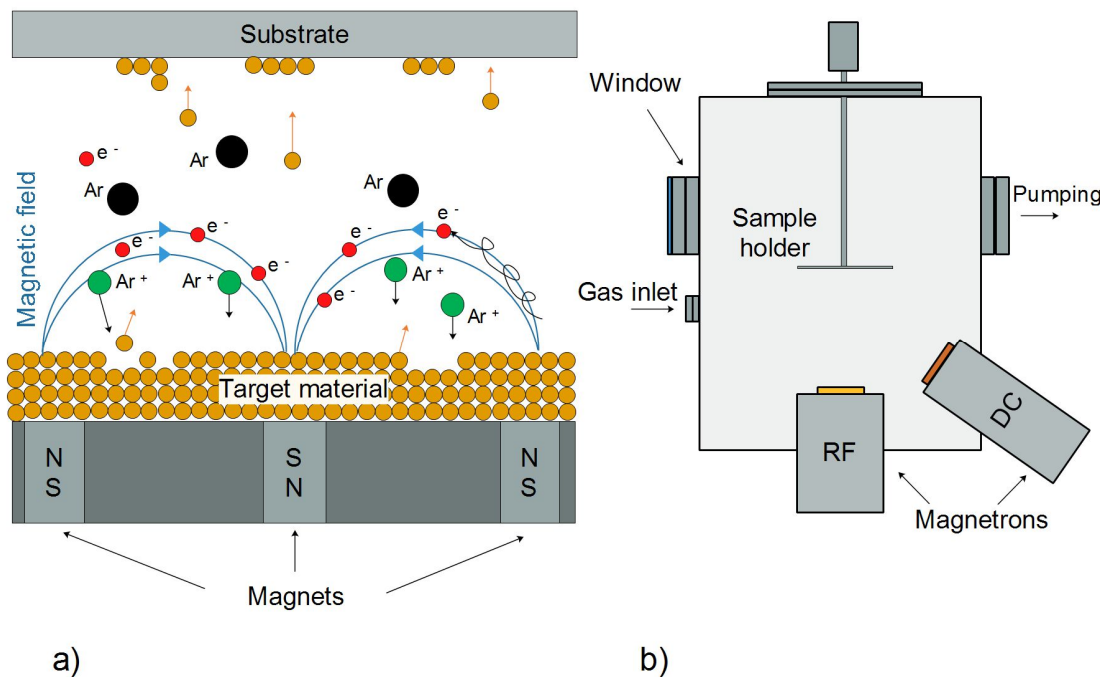


Fig. 1. The principle of sputtering process (a) and schematic illustration of magnetron sputtering technique using different magnetrons (b).

Material is detached (i.e. sputtered) from the target and then deposited on the substrate in the vicinity. Such process takes place in vacuum chamber, which is pumped down to base vacuum pressure before starting the deposition procedure. At direct current (DC) sputtering, negative potential is applied to the target, thus, positively charged Ar^+ ions bombard it. Within sputtering process secondary electrons form as well and create plasma by bombarding Ar atoms. Ring magnets located below the target are used for increasing the ionization rate. One pole of the magnet is positioned at the central axis of the target while the second one is formed by a ring of magnets that surround the external region of the target. In such

arrangement the electrons in magnetic field are trapped in cycloids and circulate over the target surface. It increases the ionization probability and makes the plasma ignitions under lower operation pressure.

DC sputtering method allows deposition only from conductive target materials. Deposition of non conductive materials is possible by using radio frequency (RF) sputtering. In this case alternating current (AC) with frequency about 13.56 MHz is applied to the target. Within RF sputtering, during the one phase ions are accelerated to the target material and then at the other phase charge neutrality is achieved. In such way surface of non conductive material would not be charged at all.

Instead of inert gases, chemical reactive gases such as oxygen or nitrogen can be used to perform reactive sputtering. In this case oxidic or nitridic layers will be grown during deposition procedure.

In this work thin films were prepared using apparatus schematically presented in *Fig. 1b*. The device consists of RF and DC magnetrons with 2'' platinum and ceria targets. Magnetrons are mounted in vacuum chamber at the angle of 45° between them. Rotated sample holder is located in 90 mm and 200 mm away from RF and DC magnetrons respectively. Deposition in all cases was carried out at room temperature with base pressure of working gas about 4×10^{-1} Pa. Platinum and platinum oxide thin films were prepared in argon and oxygen atmospheres respectively by applying of 10 W to DC magnetron. At such conditions deposition rate was approximately 2 nm/min for platinum oxide and 3 nm/min for metallic platinum. Pt-CeO₂ films were prepared by simultaneous deposition from both Pt and CeO₂ targets (RF-DC sputtering). In this case the power of 10 W was applied to DC magnetron, while the power of RF magnetron was adjusted to 30 W and 90 W in order to obtain low and high ceria content in Pt-CeO₂ composite film. Inverse Pt/CeO₂ thin films were prepared by deposition first, CeO₂ material from RF magnetron on SiO₂ substrate, then Pt material from DC magnetron on ceria interlayer.

2.2. X-ray photoelectron spectroscopy (XPS)

X-ray photoelectron spectroscopy (XPS) is the most widely used surface analysis technique [2]. It can be applied to a broad range of materials and provides valuable quantitative and chemical state information about it. XPS was developed by research group of K. Siegbahn in the mid of 1960s. Such method is based on the

photoelectric effect where the concept of the photon was used to describe the ejection of electrons from a surface when photons fall on it (*Fig. 2a*).

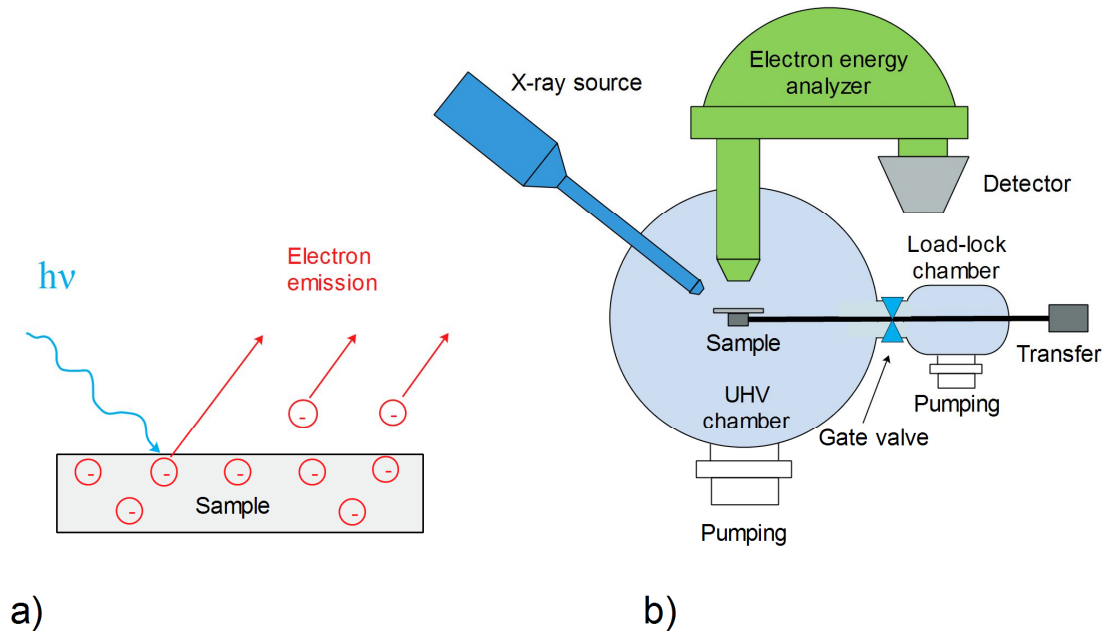


Fig. 2. Basic principle of X-ray photoelectron spectroscopy (a) and schematic of laboratory XPS apparatus (b).

Electrons escaping from the analyzed material can be monitored by energy analyzer, which determines the number of such electrons and their binding energies (BE). From this data a spectrum of intensity of emission versus BE of electrons can be obtained (*Fig. 3*).

The binding energy of the emitted electrons E_b is given by equation:

$$E_b = h\nu - E_k - \Phi_s \quad (1)$$

where $h\nu$ – photon energy; E_k – kinetic energy of ejected electrons; Φ_s – the work function of the spectrometer.

For each element, there will be a characteristic binding energy associated with each core atomic orbital i.e. each element will give rise to a characteristic set of peaks in the photoelectron spectrum at kinetic energies determined by the photon energy and the respective BEs. The presence of peaks at particular energies therefore indicates the presence of a specific element in the sample studied. Furthermore, the intensity of the peaks is related to the concentration of the element within the sampled region. Since the photoionization process results in both core-level electron and

Auger electron emission in addition to the XPS peaks, measured spectrum also contains Auger peaks.

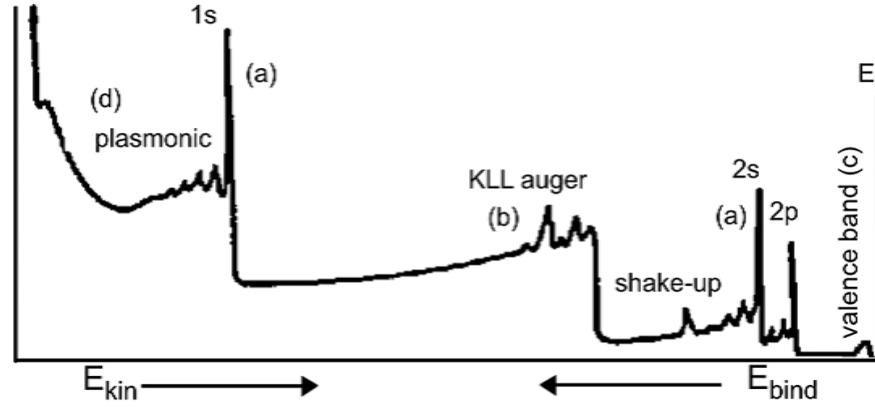


Fig. 3. A typical XPS spectra obtained from solid material: (a) emission from core level; (b) auger processes; (c) emission from the valence band; (d) secondary electron excitation and energy losses by inelastic scattering of the electrons [3].

The relation between the intensity of the photoelectron peaks and the element concentration gives the quantitative information of the analyzed sample. In the typical case of a homogeneous solid, the relative atomic concentration of some chosen element is obtained from:

$$C_A = \frac{\frac{I_A}{S_A}}{\sum_n \frac{I_n}{S_n}} \quad (2)$$

where C_A is chosen element (expressed as atomic %). The n is number of elements which give intensities (peak areas) of I_A, \dots, I_n measured using relative sensitivity factors S_A, \dots, S_n .

The XPS apparatus used in this work is presented in *Fig. 2b*. It consists of the main ultra high vacuum (UHV) chamber with the base pressure of 5×10^{-8} Pa and load-lock vacuum chamber pumped down to 10^{-6} Pa. The load-lock chamber is separated from the main chamber by the gate valve. Also it is equipped with a long transfer which allows inserting the sample in main UHV without disturbing the vacuum. Main UHV chamber is pumped down by means of dry scroll and a turbomolecular pumps while pre-vacuum chamber is evacuated using a combination of a rotary and turbo pumps. A hemispherical electron energy analyzer (Phoibos 150,

supplied by SPECS) as well as $Al\ K\alpha_{1,2}$ (1486.6 eV) and $Mg\ K\alpha_{1,2}$ (1253.6 eV) X-ray sources were mounted in main UHV chamber. Total energy resolution of analyzer is $\Delta E = 1\text{ eV}$. For measurements described in this thesis only $Al\ K\alpha_{1,2}$ X-ray source was chosen. This is because the lower photon energy of the $Mg\ K\alpha_{1,2}$ source would lead fundamentally to higher and more inclined non linear Ce 3d spectrum background resulted in lower peak fitting precision.

2.3. Scanning electron microscopy (SEM)

The scanning electron microscopy (SEM) is the most versatile instrument available for the microstructure analysis and chemical composition characterizations. SEM uses a focused beam of electrons (100 eV - 30 keV) to produce a variety of signals from the surface of the sample, which further reveals information about morphology, chemical composition and crystalline structure. The resolution of SEM depends on the spot size of the electron beam. Thus, the better image resolution can be archived when operated with smaller spot size of the beam. Modern SEM apparatus can distinguish details on the surface less than 1 nm in size.

When the incident electrons are decelerated in the solid sample, it produces different signals (*Fig. 4a*) such as secondary electrons (SE), backscattered electrons (BSE), Auger electrons, photons (characteristic X-rays) and visible light (cathodoluminescence). SE and BSE are commonly used for imaging of the samples. Low-energy (<50 eV) SE emitted due to inelastic electron scattering are most valuable for imaging of morphology and topography of the samples. The topography of the surface affects the number of emitted electrons that enters the electron detector from analyzed surface. Such difference in electron intensities creates the image contrast that reveals the surface morphology. High-energy BSE (~20 keV) produced by the elastic interactions are used for illustrating contrasts in composition in multiphase samples. The intensity of the signal of emitted BSE is proportional to the atomic number of the sample material. Higher atomic number material appears brighter while low atomic number material becomes darker, due to higher electron reflections of heavier elements. Accordingly, image contrast as a function of composition can be observed.

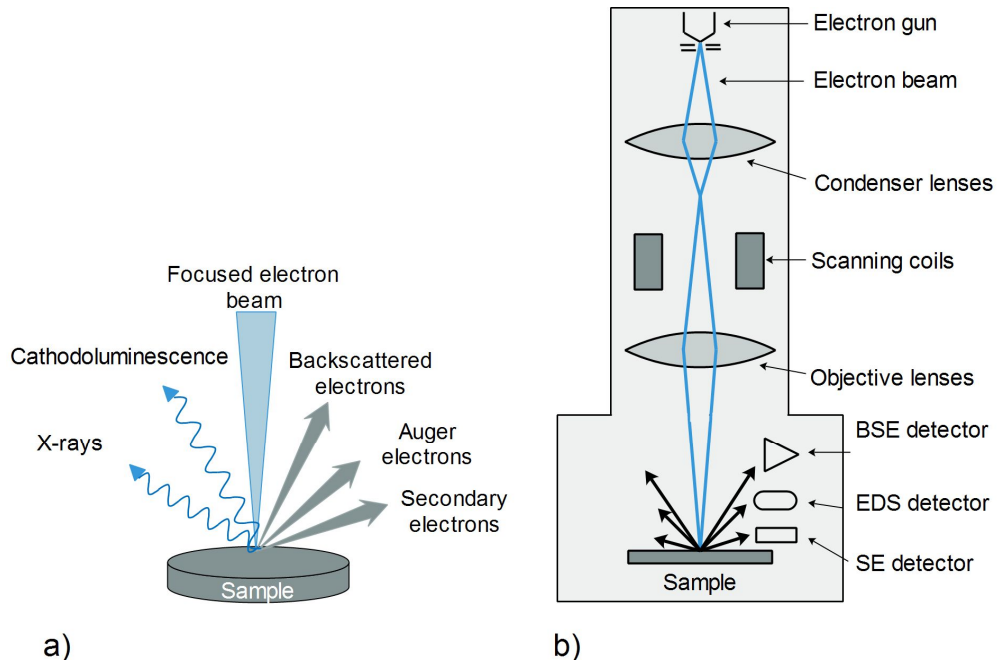


Fig. 4. Emission of different electrons and electromagnetic waves at electron - sample interaction (a); schematic of SEM apparatus (b).

X-rays emitted from the sample are used for chemical analysis. Energy of X-rays is characteristic of the atomic structure of the element from which they were emitted. The number and energy of such X-rays can be measured with an energy dispersive X-ray spectrometer (EDS).



Fig. 5. Overall view of TESCAN-MIRA scanning electron microscope.

The typical SEM apparatus consists of optical system, sample chamber and different detectors surrounded by UHV of 10^{-3} to 10^{-4} Pa (*Fig. 4b*). Optical system includes an electron gun, condenser and objective electromagnetic lenses to produce a focused electron probe and scanning coils to scan the electron probe. During the observation process, emitted electrons are collected by SE and BSE detectors over a selected area by scanning of the surface with further generating of a 2-dimensional image. Also quantitative and qualitative chemical analysis of selected point locations on the sample can be done by using EDS detector.

In this work morphology of REOs powders as well as Pt, PtO_x and Pt-CeO₂ thin films were observed with SEM apparatus (TESCAN-MIRA) equipped with SE, BSE and EDS detectors (*Fig. 5*). Among available detectors only SE detector was used for imaging. The measurements were done at 1×10^{-2} Pa working pressure in the sample chamber and 30 keV of electron beam energy.

2.4. Microreactor system

In order to perform catalytic activity tests on nanopowder and thin film samples at high pressure conditions a laboratory microreactor system was designed (*Fig. 6*). Such apparatus consists of ex-situ reaction cell connected to UHV analytic chamber equipped with differentially pumped quadruple mass spectrometer (QMS, Pfeiffer Prisma 200). Analytic chamber was pumped down to 10^{-5} Pa by combination of turbomolecular and rotary vane pumps.

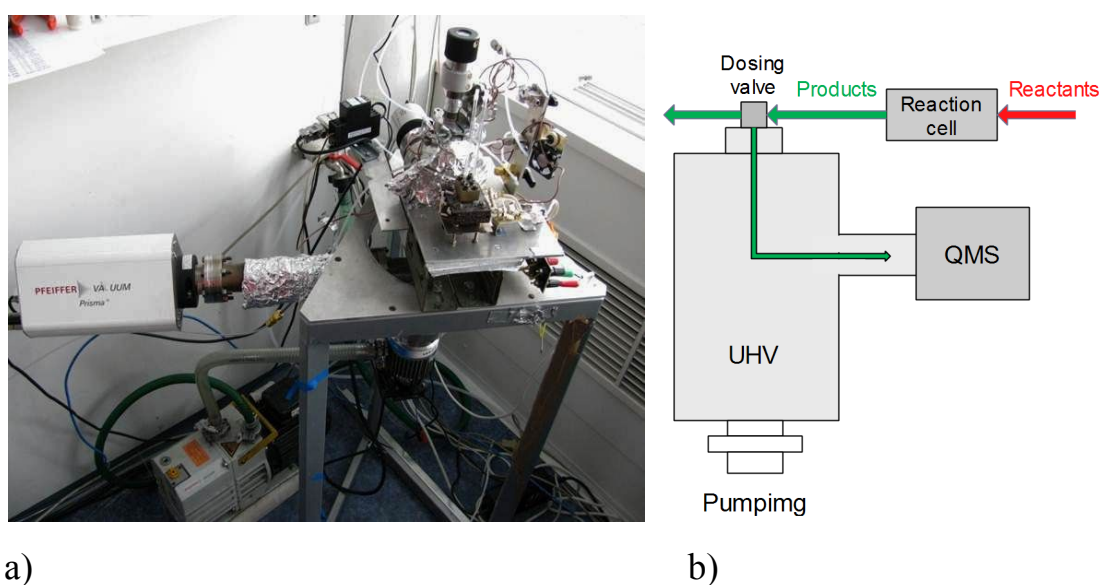


Fig. 6. The laboratory microreactor system: overall view (a) and schematic (b).

Reaction cell is mounted on a proportional-integral-derivative (PID) regulated resistive heater with two the K-type thermocouples, one of them placed inside the heater and another one located under the reaction cell. During the activity test, gas mixture of reactants adjusted to desirable composition and rate by mass flow controllers (Alicat Scientific) and flows through the reaction cell with catalyst, while a heating program is applied to it. A product of the reaction passes through the dosing valve and enters the UHV analytical chamber, where change of concentration of it is analyzed online by QMS. In such design there is ability to perform various activity tests at atmospheric pressure and temperatures, which are close to practical usage of catalysts.

CO oxidation reaction over thin film and nanopowder catalysts was done using the microreactor setup schematically presented in Fig. 7a.

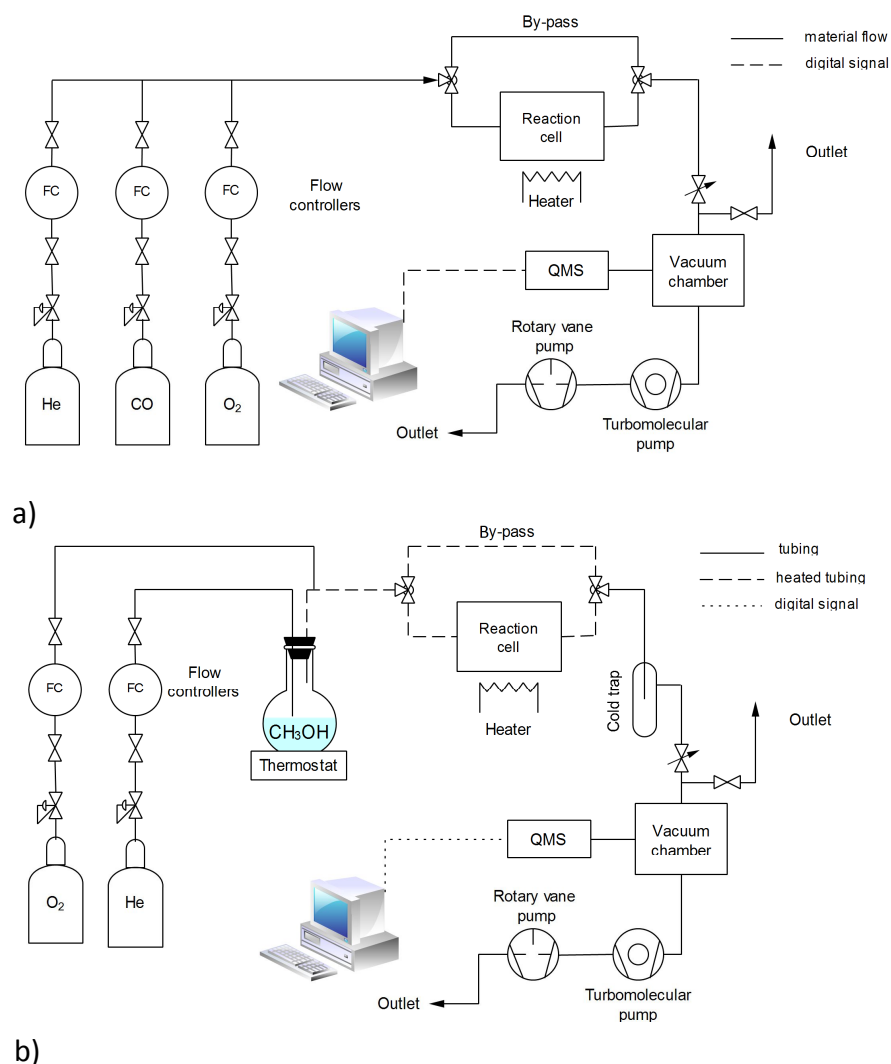


Fig. 7. Schematic drawing of the microreactor setup for CO oxidation (a) and methanol oxidation (b) experiments.

During the reaction, gas mixture of carbon monoxide (Linde Gas, 4.7 purity) and oxygen (Linde Gas, 5.0 purity) as reactants together with a helium buffer gas (Linde Gas, 4.6 purity) enters the reaction cell. Helium is used as main carrier gas flow (it is not involved in surface reaction at all). After passing the reaction cell, product gas mixture flows to the UHV chamber with QMS.

In order to perform methanol oxidation experiments on thin film catalysts we used microreactor setup presented in *Fig. 7b*. Methanol vapor was created by bubbling of helium buffer gas through the saturator filed with methanol (Penta, 99.8% purity). Oxygen was added to the methanol steam prior to reaction cell to avoid undesirable interaction of the reactants in the saturator. Stainless-steel tubing between saturator and reaction cell were heated (up to 130 °C) to prevent condensation of reactants before reaching the sample. Ratio of methanol to oxygen was adjusted to a desirable level by changing parameters such as temperature of saturator and flow rates of helium and oxygen. Before entering the UHV chamber the product stream was passed through a laboratory cold trap immersed in Dewar flask, filled with freezing mixture (liquid nitrogen + ethanol, $T = -80\text{ °C}$) to remove water and unreacted methanol.

Reactivity tests on thin film catalyst were done using low temperature sample holder schematically illustrated in *Fig. 8*.

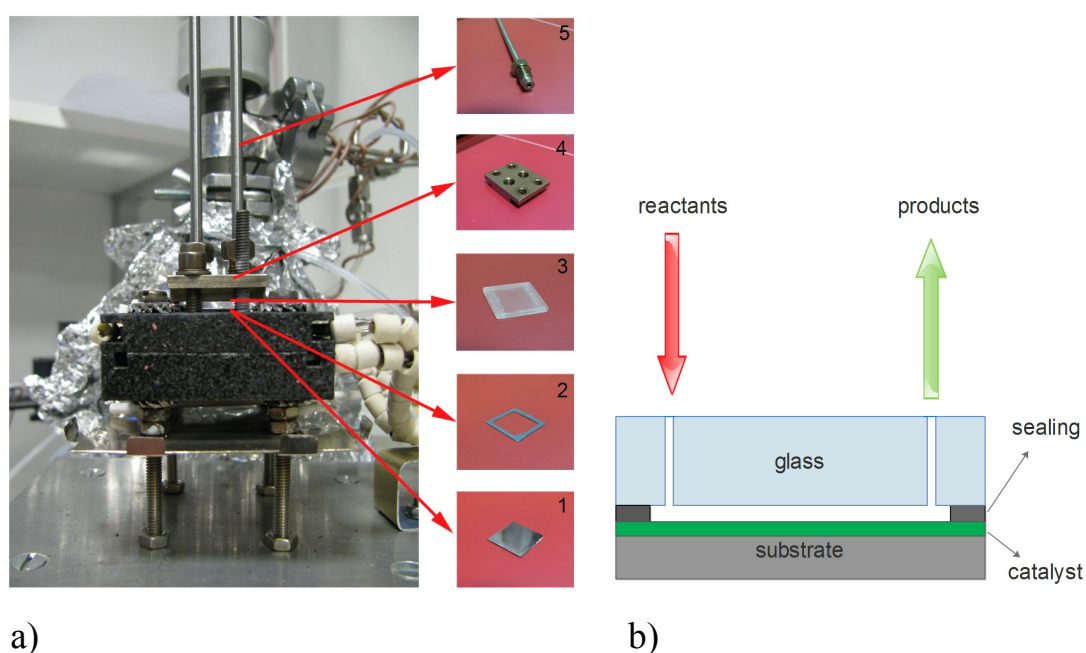


Fig. 8: (a) low temperature sample holder for thin film catalyst: 1 - thin film sample; 2 - rubber sealing; 3 - upper glasses with holes; 4 - metal fastener; 5 - tubes; (b) schematic drawing of reaction cell formed by sample, upper glass and rubber sealing.

Here, the reaction cell is formed by 16×16 mm flat sample at the bottom and quartz glass with inlet and outlet holes at the top. In order to retain the reaction cell tight a silicone rubber sealing (100 μm thick) is sandwiched between the upper glass and the sample (*Fig. 8b*). Since the reaction cell is mounted directly at the top of the heater, there are advantages such as good heating control and temperature stability of all catalyst content. This leads to the disappearance of hysteresis in analyzed data between heating up and cooling down procedure. Disadvantage of such cell in some cases could be not high enough operating temperature (approximately 350 °C) due to temperature limitation of sealing parts, hence, it can be used only for low-temperature reactions.

In order to perform high-temperature activity tests over thin film and nanopowders samples a sample holder shown in *Fig. 9* has been designed.

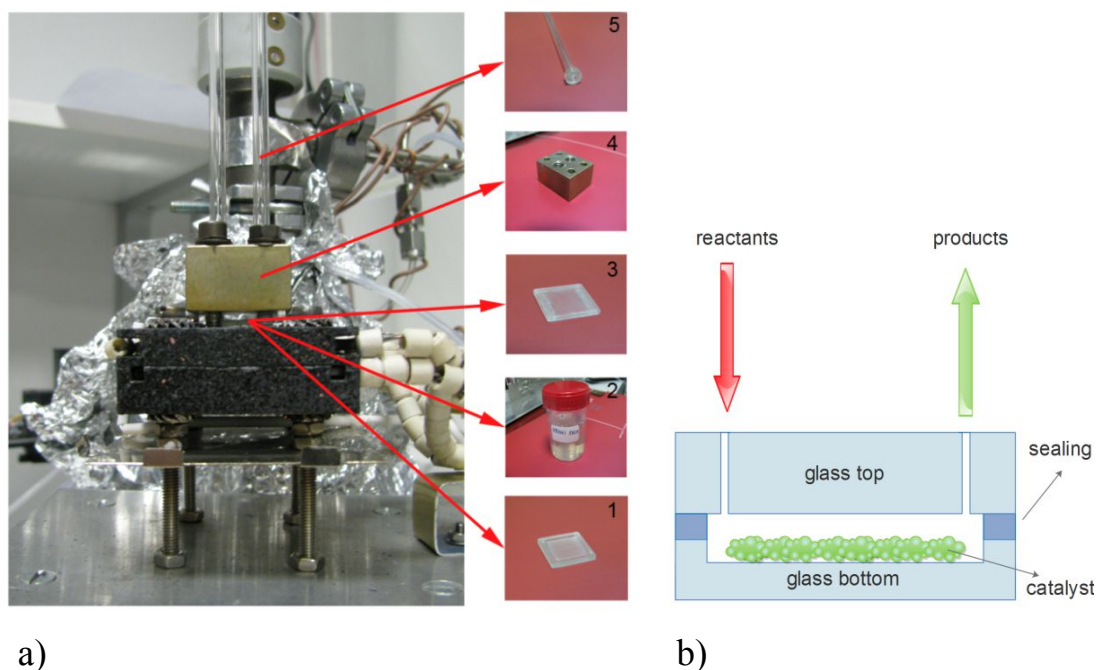


Fig. 9: (a) high temperature sample holder for powder catalyst: 1 - bottom quartz glass with groove; 2 - sealing; 3 - upper glasses with holes; 4 - metal fastener; 5 - silica tubes; (b) schematic drawing of reaction cell formed by bottom and upper glasses sealed by “water glass”.

In this case the reaction cell is formed by bottom quartz glass with groove for catalyst and top glass, which is the same as for the aforementioned cell. We used “water glass” ($\text{Na}_2\text{O} (\text{SiO}_2)_n$) for sealing the glass parts of the cell as well as attaching silica tubes to the top glass. Such design allows heating the reaction cell up to 650 °C, which opens an opportunity to study reactions at higher temperature. Beside this, we

need only 1-2 mg of powder catalyst for proper measurement in contrary to the usual bad flow reactors, which requires about 100 mg of it. Also due to good the temperature control of the reaction cell there is no need to dilute the powder catalyst.

QMS was used for online analyzing the products of the reactions. Such device generates multiple ions from the sample under investigation with further separation according to their specific mass-to-charge ratio (m/z). Thereafter it records the relative abundance of each type of ion. Basically QMS consists of ion source, quadrupole analyzer and detector (*Fig. 10*).

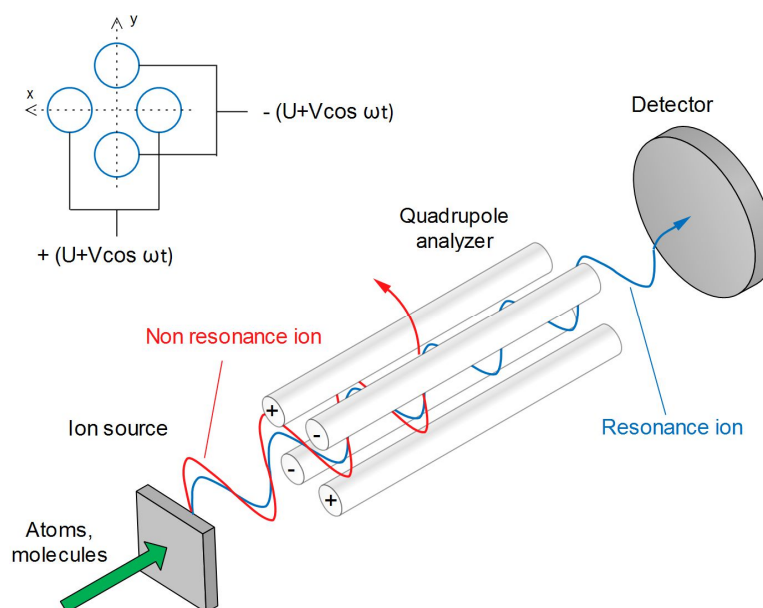


Fig. 10. Basic principle of QMS.

In the ion source, electrons ejected from a hot filament are bombarding atoms and molecules of analyzed gas, causing ionization. Then charged ions are accelerated to the quadrupole analyzer. Quadrupole analyzer consists of four parallel metal rods of hyperbolic or circular cross-section. Opposite rods are electrically connected. A voltage including a DC component U and a RF component $V_0 \cos(\omega t)$ is applied to the adjacent rods. The applied voltages affect the trajectory of ions moving down according to flight path centered between the four metal rods. For given DC and RF voltages, only ions with a certain m/z ratio pass through the quadrupole filter and reach the detector. All other ions do not have a stable trajectory. Thus, such ions will collide with the quadrupole rods. Ions that successfully passed the quadrupole filter enter the ion detector. A mass spectrum is obtained by monitoring the ions passing through the quadrupole filter, when voltages on the rods are changed.

3. CO oxidation

3.1. Motivation

Nowadays, questions concerning protection of environment became more and more actual due to worsening ecological situation worldwide. Air in big cities contains harmful pollutants, which cause adverse impact on flora and fauna. Also it results in negative long-time processes such as decreasing of average human lifespan and global warming [4]. The major sources of the man-made urban emission are fossil-fuel power stations and internal combustion engines of cars. When petrol or diesel fuel (which mainly consists of hydrocarbons (C_xH_x)), burns in the cylinders of a car engine, the main products are nitrogen N_2 (67-71%), water vapor H_2O (11-12%) and carbon dioxide CO_2 (12-14%). Due to the incomplete combustion of hydrocarbons and excessive temperatures of burning the exhaust from engine also contains some CO (0.045-1%), unburned hydrocarbons (0.03-0.25%) and nitrogen oxides NO_x (0.15-0.25%) which are toxic [5]. Small amount of sulfur dioxide SO_2 (<0.03%) can be present as additive in emissions from fossil-fuel power stations. In many countries the most common type of fatal air poisoning is caused by CO [6].

In the early seventies catalytic converters for cars and smoke stack scrubbers for factories were first introduced to overcome the problems caused by air pollutants [7]. These systems could convert toxic pollutants as C_xH_x , NO_x , and CO into less harmful products such as carbon dioxide, water and nitrogen by using catalysts, which speed a chemical reaction without being permanently altered itself. Such process takes place via oxidation-reduction reactions, in particularly carbon monoxide (CO) oxidation:



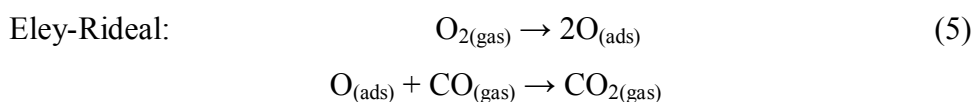
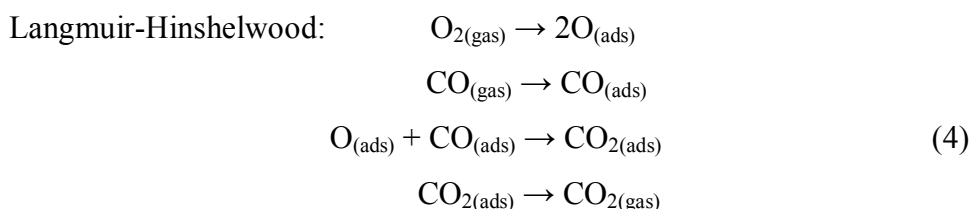
CO oxidation is widely adopted not only for convert exhaust gases but also plays a key role in CO_2 lasers and gas sensors [8,9,10]. Another important application is selective CO oxidation for the production of CO free hydrogen-rich gas for fuel-cells (FC). For instance, *proton exchange membrane fuel-cell* (PEMFC) cannot withstand more than several ppm (parts per million) of CO in feed gas stream. Higher concentration of carbon monoxide deactivates the platinum catalyst which reduces

efficiency and durability of PEMFC [11]. Thus, reducing CO content by selective CO oxidation is a necessary step for hydrogen FC technology.

Platinum group metals (Pt, Pd, Rh, Ru) are known as good catalysts for CO oxidation [12]. Since the mid-1980s, gold (Au) has been considered as an effective catalyst [13]. Limited availability and high cost of such catalysts motivated to search less expensive alternative with equal or even better reactivity. Novel CO oxidation catalysts, which are precious metals or their oxides, use either “active” (TiO₂, Fe₂O₃, NiO_x, CoO_x) or inert (different type of carbon) support materials [14,15]. REOs, in particularly CeO₂ doped by platinum group metals, also exhibits high activity and stability as CO oxidation catalyst [16]. Challenge in catalytic industry requires lower content of precious metals with higher surface area to obtain cheaper and more efficient catalyst. Nowadays, there are many methods and techniques available for preparation of catalyst that will meet above mentioned demands. In this chapter we will show new sol-gel approach for preparation of novel REOs catalysts. Also Pt based thin film samples will be prepared by magnetron sputtering method, which is simply, fast and most promising method for thin films preparation. CO oxidation reaction at ambient pressure condition will be checked over prepared specimens by using microreactor system.

3.2. CO oxidation mechanisms

Oxidation of carbon monoxide (3) is a heterogeneous catalyst reaction, which is one of the most widely studied process in surface chemistry at both high and low pressure conditions. Such reaction takes place on the surface of transition metal catalyst via Langmuir-Hinshelwood (4) or Eley-Rideal (5) mechanisms [17]:



Langmuir-Hinshelwood (L-H) mechanism (Fig. 11a) consists of the following consecutive steps: adsorption of both oxygen and carbon monoxide from the gas phase on the surface of the catalyst; dissociation of oxygen molecule followed by the reaction with chemisorbed carbon monoxide; desorption of carbon dioxide from the catalyst surface as a product of the reaction.

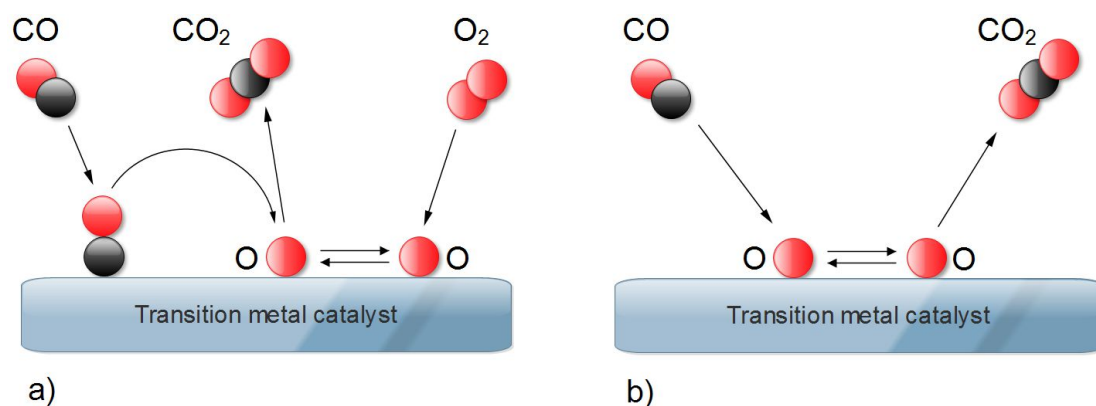


Fig. 11. Schematic description of the mechanisms of CO oxidation reaction on transition metal catalyst: Langmuir-Hinshelwood (a) and Eley-Rideal (b).

Eley-Rideal (E-R) mechanism (see Fig. 11b) includes: adsorption of reactants CO and O₂; reaction between molecules CO from gas phase and dissociative adsorbed oxygen; desorption of CO₂ from the surface of catalyst.

While surface reaction in L-H mechanism takes place only between adsorbed species, E-R mechanism involves in reaction CO molecules from the gas phase which strikes the atoms of adsorbed oxygen and desorbs from the surface in the form of CO₂. Since CO is strongly bounded to the metal surface via donor-acceptor mechanism, thus, L-H mechanism is much more plausible than E-R one for CO oxidation reaction over transition metal catalysts [18].

An alternative *Mars van Krevelen (MvK) mechanism* has been proposed in the mid 50's, which is suitable for description of CO oxidation reaction over metal oxide catalyst [19]. MvK mechanism (Fig. 12) includes following steps: forming the metal oxide surface by oxygen exposure at the elevated temperature; adsorption molecules of CO from gas phase onto oxide; reaction between adsorbed CO and oxygen from the metal oxide; desorption of CO₂ as product of reaction; refilling of oxygen vacancy formed on the surface of catalyst by oxygen from gas phase. The important feature of MvK mechanism is that the product of the reaction leaves the solid catalyst's surface with constituent of lattice and forms the vacancy. Such

instability of the surface leads to high probability of forming protrusions on it by unoccupied metal atoms, before oxygen adsorbs from the gas phase. Thus, catalyst plays more active role in CO oxidation process.

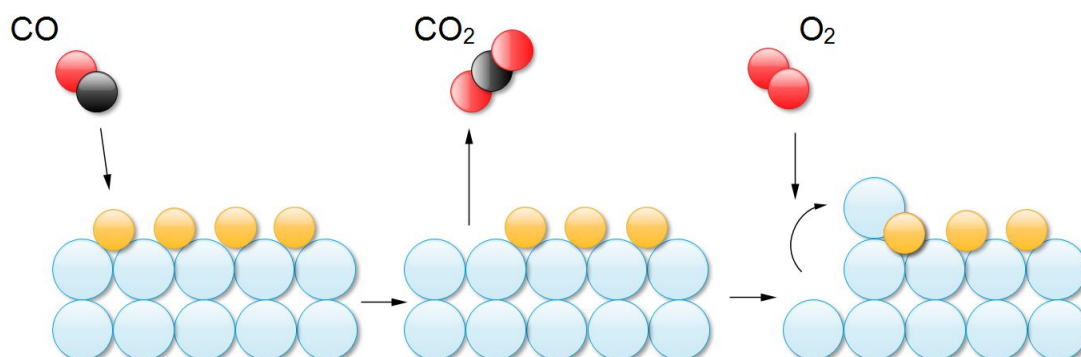


Fig. 12. Mars van Krevelen mechanism of CO oxidation reaction. Blue balls represent metal atoms. Small orange balls correspond to oxygen atoms of metal oxide.

CO oxidation reaction can be performed in two regimes called “steady-state” and “transition - state”. “Steady-state” regime is when the concentration of reactants (CO and O₂) is constant as well as the temperature. In this case CO₂ production can be monitored at selected constant temperatures by applying “heating steps” procedure. Other way is heating the catalysts with slow rate in order to obtain each measurement point near to isothermal (so-called “quasi steady-state”). In case of the “transition - state” regime, CO₂ production is monitored after fast change of one parameter (temperature, concentration of O₂ or CO).

Traditionally kinetics of CO oxidation over transition group metals has been well-studied on single crystal surface at low pressure condition ($< 10^{-5}$ Pa) using the UHV chamber with the different surface science probes [20]. There is a “pressure gap” between practical catalytic condition and UHV (10^2 vs. 10^{-6} Pa). In this case some important surface processes that occur during practical catalytic usage may not be obtainable in UHV studies. In addition, reactivity of two identical catalysts performed in both high and ambient pressure conditions can be different [21]. Another important difference between UHV study and realistic catalytic conditions is form of the catalyst – i.e. “material gap”. Catalysts for UHV study is mostly well-defined single crystal surfaces of metal. For practical usage, catalyst is dispersed on high surface area supports to obtain better efficiency. Also interaction that occurs between the metal and its support (metal-support interaction) can alter the

activity [22,23]. In order to overcome “pressure gap” and “material gap” a laboratory microreactor system has been used for CO oxidation tests. Hence, reactivity can be studied at conditions close to the practical usage, which makes such researcher more valuable for industrial catalysis.

3.3. CO oxidation on Pt thin film catalysts

In order to compare CO oxidation mechanism on metallic and oxidized Pt we prepared Pt and PtO_x thin films using magnetron sputtering technique (see *subchapter 2.1*). Thin film catalysts were deposited on commercial Graphite foil (G-foil, Alfa Aesar, 0.254 mm thick, 99.8% (metal basis)) and on naturally oxidized Si (110) wafer (SiO₂) by using magnetron sputtering technique. Such substrates were chosen for their flat morphology, inert properties and sintering stability. Also for comparison, PtO_x and Pt were deposited on carbon interlayer (C, thicknesses about 20 nm) grown on SiO₂ wafer by means of commercial modular high vacuum coating system MED020 (BALTEC). Deposition procedure of films was carried out at room temperature using DC magnetron (DC power - 10 W) from a 2” diameter platinum (99.95% purity) target placed 90 mm away from the substrate. In order to grow PtO_x layers we used O₂ atmosphere in the magnetron chamber with constant pressure of 4×10^{-1} Pa, while metallic Pt layers were obtained in pure Ar atmosphere. Following six samples with the same thickness of platinum (10 nm) were prepared: Pt/SiO₂; Pt/G-foil; Pt/C/SiO₂; PtO_x/SiO₂; PtO_x/G-foil and PtO_x/C/SiO₂.

CO oxidation tests over prepared samples were done in the microreactor system using the setup illustrated on *Fig. 7a* and the sample holder for thin film catalysts (*Fig. 8*). During the experiments we used stoichiometric working gas mixture: 3 sccm (standard cubic centimeter) of CO and 7 sccm of O₂ diluted by 30 sccm of helium buffer gas. Since CO oxidation on platinum takes place at relatively low temperatures, thus, we examined samples in temperature region between 50 and 300 °C. The heating rate was set to sufficiently low 2 °C/min in order to obtain each measured point near to isothermal. Three consecutive temperature programmed reactions (TPR) were done on each sample under equal experimental conditions. Obtained QMS data were used for plotting conventional and Arrhenius graphs. The plots were used for analyzing the effect of temperature on the reaction rate which is proportional to the QMS signal intensity. Conventional graphs have

been done by plotting QMS CO₂ intensity versus temperature (T, °C). Arrhenius graphs at selected temperature regions have been done by plotting a logarithm of CO₂ QMS intensity versus 1000/T (K⁻¹). Activation energies (E_a) of reaction (i.e. the minimum energy required before a reaction can occur) were calculated from selected linear regions of Arrhenius graph using Arrhenius equation:

$$k = Ae^{-\frac{E_a}{RT}} \quad (6)$$

where k is a rate constant, A is frequency factor, E_a activation energy, R - characteristic gas constant, T - absolute temperature (expressed in Kelvin).

Since Arrhenius graph is expressed in logarithmic scale we modified the equation (6):

$$\ln k = \ln A - \frac{E_a}{R} \cdot \frac{1}{T} \quad (7)$$

By using Origin™ software we made a linear fit from the selected parts of the Arrhenius plot. Linear fit is the line equation $y = a + b \cdot x$, where a corresponds to $\ln A$ (from equation 7), constant b (i.e. slope of line) corresponds to $-\frac{E_a}{R}$ and x corresponds to $\frac{1}{T}$. To obtain E_a expressed in kJ/mol we multiplied obtained b value by $-\frac{R}{1000}$.

Surface morphology of the samples (as prepared and after CO oxidation cycle TPR3) was investigated by SEM (*Fig. 13, 14*). As prepared Pt/SiO₂ sample exhibited nearly flat and continuously morphology (*Fig. 13a*), which did not change much after TPR3 stage, only sintering effect is apparent forming grains and patches sized about ten nanometers in diameter (*Fig. 13d*). As prepared Pt/G-foil sample demonstrated flat morphology similar to the Pt/SiO₂, but has a pattern which replicates the G-foil substrate (*Fig. 13b*). The surface of Pt/G-foil specimen after TPR3 stages (*Fig. 13e*) exhibited grains and patches sized up to 100 nm in diameter. Also, rare holes with visible G-foil substrate are presented. Morphology of as prepared Pt/C/SiO₂ specimen is flat and homogeneous (*Fig. 13c*) similar to the Pt/SiO₂. After the CO oxidation

TPR3 (*Fig. 13f*) specimen exhibited similar patches and grains as Pt/G-foil one, but differ in more area with uncovered C interlayer (approx. 50% of analyzed surface).

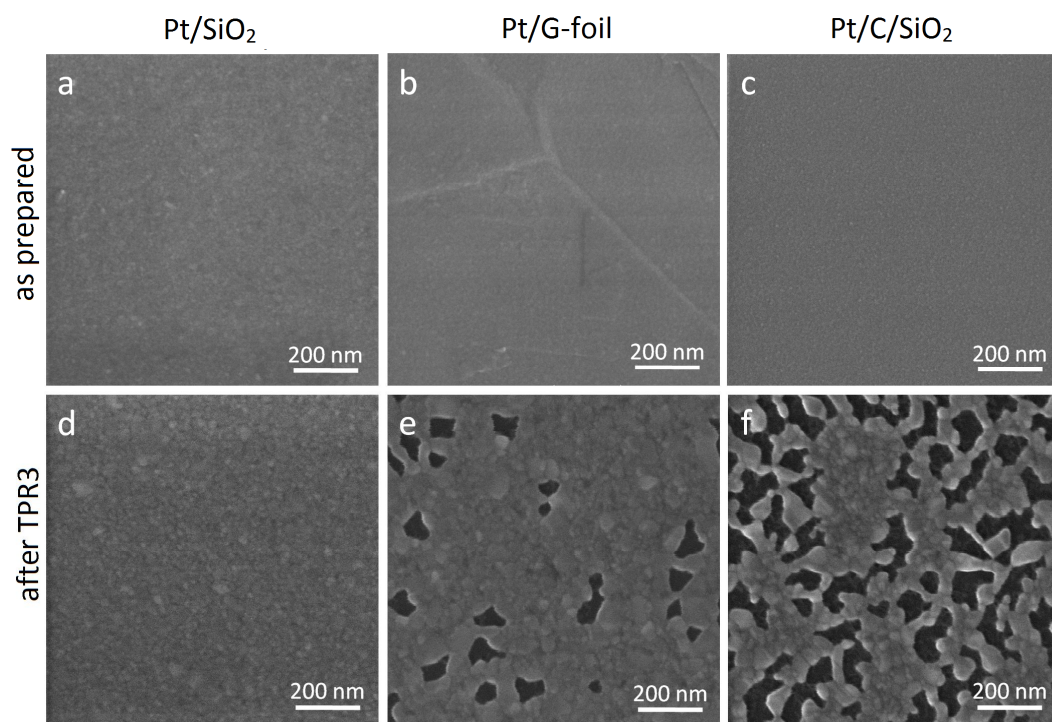


Fig. 13. SEM images of 10 nm thick Pt layers deposited on SiO₂, G-foil and C/SiO₂ substrates: Pt/SiO₂ sample as prepared (a) and after TPR3 (d); Pt/G-foil as prepared (b) and after TPR3 (e); Pt/C/SiO₂ as prepared (c) after TPR3 (f).

As prepared PtO_x/SiO₂, PtO_x/G-foil and PtO_x/C/SiO₂ samples (*Fig. 14a, b, c*) demonstrated similar flat and continuous morphology. After CO oxidation (TPR3) each sample exhibited granular structures with well-defined grains sized 40 nm in diameter (*Fig. 14c, d, e*) surrounded by corresponding substrates (SiO₂, G-foil, C interlayer).

Catalytic activity of Pt/SiO₂ sample is presented in *Fig. 15*. During TPR1 CO₂ started to produce (CO₂ onset) around 240 °C. At TPR2 and TPR3 CO₂ onsets were shifted to 190 °C. The relative CO₂ productions during both TPR2 and TPR3 were observed up to 1.5 higher compared to TPR1 at highest reaction temperature (300 °C). Arrhenius plot of TPR1 (inset in *Fig. 15*) exhibited slightly curved behavior at initial temperatures and becomes linear at the end of TPR1. During TPR2 and TPR3 the behavior of Arrhenius plot is linear across the whole temperature range.

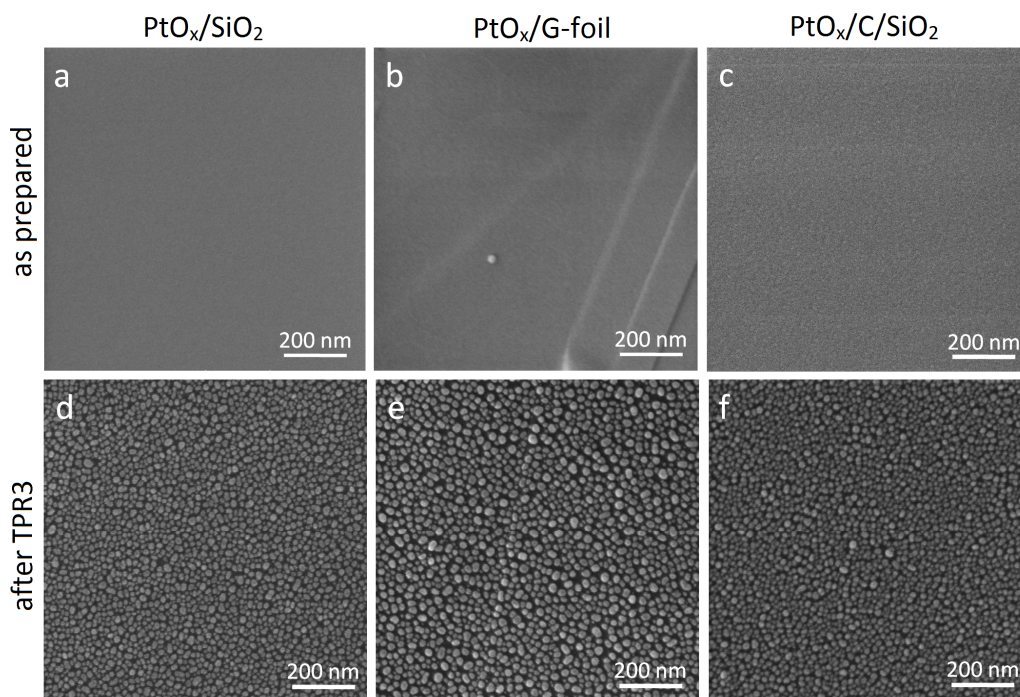


Fig. 14. SEM images of 10 nm thick PtO_x layer deposited on different substrates: PtO_x/SiO₂ as prepared (a) and after TPR3 (d); PtO_x/G-foil as prepared (b) and after TPR3 (e); PtO_x/C/SiO₂ as prepared (c) after TPR3 (f).

Calculated E_a from Arrhenius plots of each TPR in 180 - 220 °C linear region (such region was chosen in order to compare activation energies at point, where CO₂ started to produce) were as follows: TPR1: $E_a = 58 \pm 0.5$ kJ/mol; TPR2: $E_a = 95 \pm 2.5$ kJ/mol; TPR3: $E_a = 85 \pm 2$ kJ/mol.

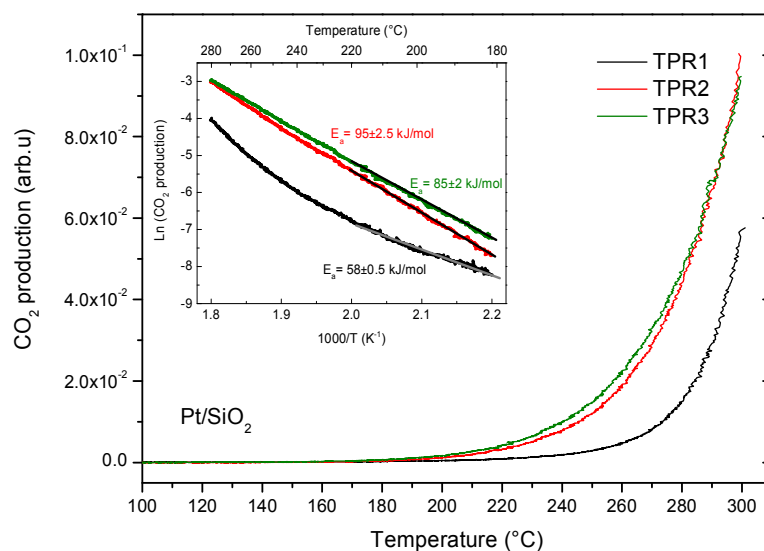


Fig. 15. CO oxidation activity of Pt/SiO₂ sample: CO₂ production plotted versus temperature (comparison of TPR1, TPR2 and TPR3); inset: Arrhenius graph of TPR1, TPR2 and TPR3 in 180 - 280 °C region.

CO oxidation activity of Pt deposited on G-foil substrates presented on *Fig. 16*. During TPR1 CO₂ onset was detected at 240 °C, while at TPR2 and TPR3 it shifted to 200 °C. Also each consecutive TPR exhibited 50% higher CO₂ yield than previous one in whole temperature range. Behavior of Arrhenius plots during each TPR was similar to the previous sample.

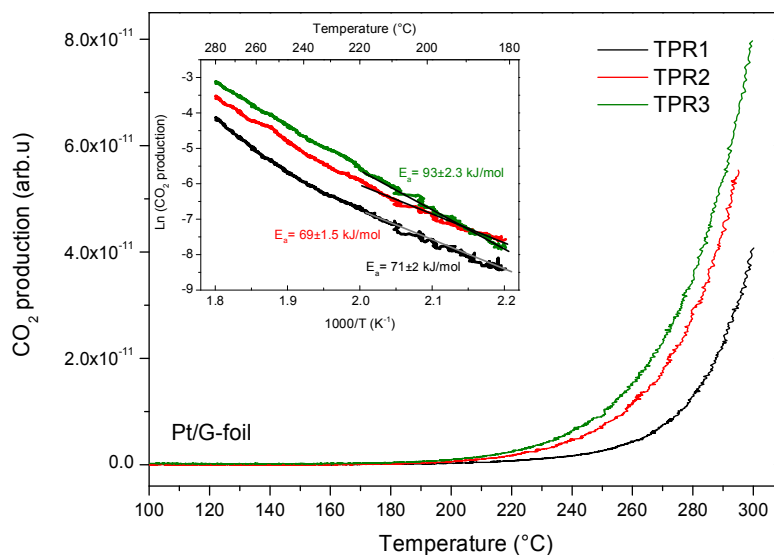


Fig. 16. CO oxidation activity of Pt/G-foil sample: CO₂ production plotted versus temperature (comparison of TPR1, TPR2 and TPR3); inset: Arrhenius graph of TPR1, TPR2 and TPR3 in 180 - 280 °C region.

The Pt/C/SiO₂ sample (*Fig. 17*) demonstrated similar activity as previous specimens, only differ in lower CO₂ yields (approx. 50%) during each TPR in whole temperature range.

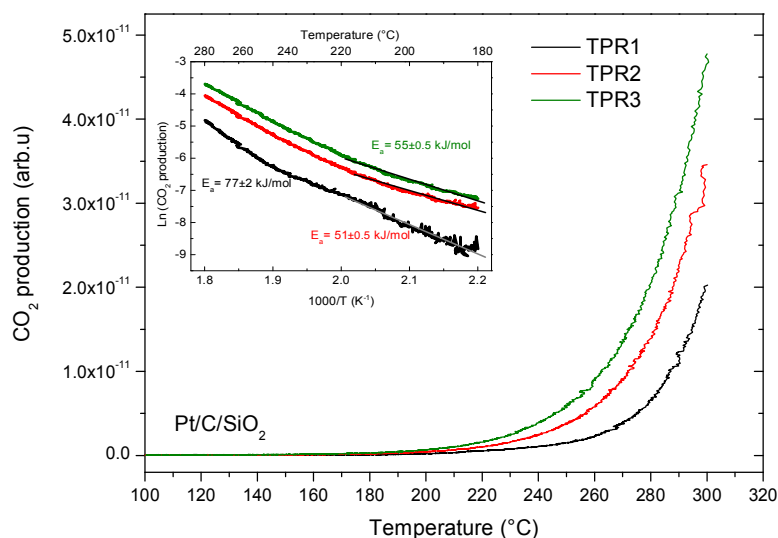


Fig. 17. CO oxidation activity of Pt/C/SiO₂ sample: CO₂ production plotted versus temperature (comparison of TPR1, TPR2 and TPR3); inset: Arrhenius graph of TPR1, TPR2 and TPR3 in 180 - 280 °C region.

Catalytic activity of $\text{PtO}_x/\text{SiO}_2$ specimen is presented on *Fig. 18*. During TPR1, CO_2 onset was detected at 180 °C, while at TPR2 CO_2 started to produce around 200 °C.

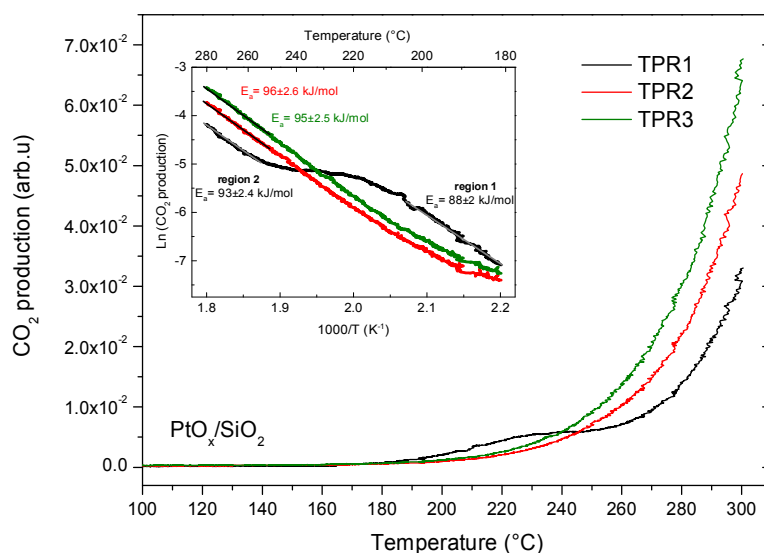


Fig. 18. CO oxidation activity of $\text{PtO}_x/\text{SiO}_2$ sample: CO_2 production plotted versus temperature (comparison of TPR1, TPR2 and TPR3); inset: Arrhenius graph of TPR1, TPR2 and TPR3 in 180 - 280 °C region.

At TPR1, we observed the elevated CO_2 production between 180 and 260 °C compared to same region of TPR2. Arrhenius plot of TPR1 (inset in *Fig. 18*) can be divided to the two linear regions with the different slopes, named region 1 (180 - 200 °C) and region 2 (260 - 280 °C). At initial temperatures the Arrhenius plot demonstrated linear behavior (region 1) followed by the non-linear region around 200 - 260 °C. Above 260 °C the TPR curve continues as a different exponential yielding second linear region (region 2). Calculated activation energies of region 1 and region 2 are $E_a = 88 \pm 2$ kJ/mol and $E_a = 93 \pm 2.4$ kJ/mol respectively. Arrhenius plots of both TPR2 and TPR3 exhibited linear character in whole temperature range and have the following activation energies (calculated from 260 - 280 °C regions): TPR2 $E_a = 96 \pm 2.6$ kJ/mol; TPR3 $E_a = 95 \pm 2.5$ kJ/mol. Also after each TPR CO_2 productions were increased 1.5 times at highest reaction temperature (300 °C).

CO oxidation activity of PtO_x/G -foil sample is presented on *Fig. 19*. Conventional plots of three TPRs demonstrated similar behavior as $\text{PtO}_x/\text{SiO}_2$ sample, only differ in less pronounced CO_2 production between 180 - 250 °C at TPR1. Also Arrhenius plot of each TPR cycles demonstrated similar behavior as in

case with $\text{PtO}_x/\text{SiO}_2$ sample. Activation energies calculated from Arrhenius plots of three TPRs are shown on the inset of *Fig. 19*.

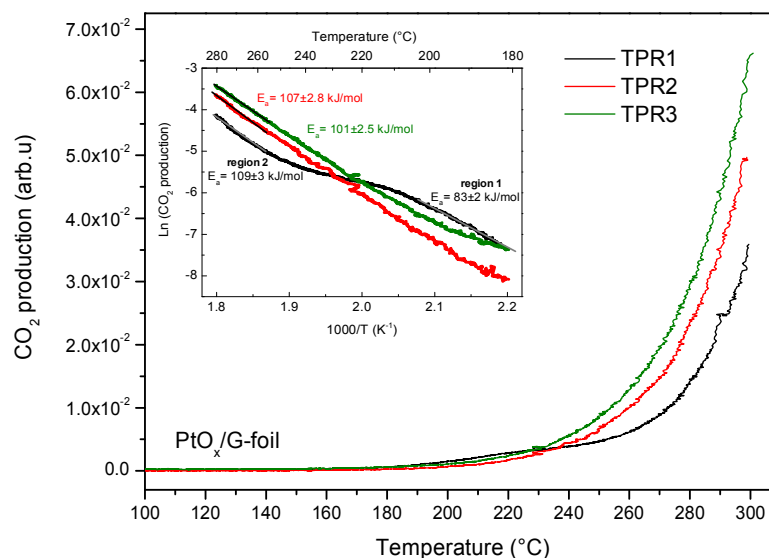


Fig. 19. CO oxidation activity of PtO_x/G -foil sample: CO_2 production plotted versus temperature (comparison of TPR1, TPR2 and TPR3); inset: Arrhenius graph of TPR1, TPR2 and TPR3 in 180 - 280 °C region.

Platinum oxide deposited on carbon interlayer ($\text{PtO}_x/\text{C}/\text{SiO}_2$) showed similar reaction behavior during three TPRs as aforementioned PtO_x thin films (*Fig. 20*). Such sample exhibited the highest CO_2 yield during TPR3 compared to other PtO_x system (at TPR3 cycle).

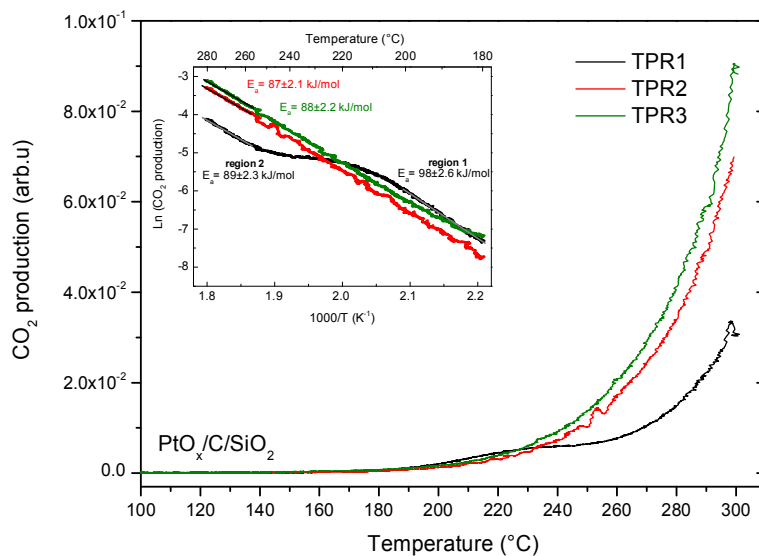


Fig. 20. CO oxidation activity of $\text{PtO}_x/\text{C}/\text{SiO}_2$ sample: CO_2 production plotted versus temperature (comparison of TPR1, TPR2 and TPR3); inset: Arrhenius graph of TPR1, TPR2 and TPR3 in 180 - 280 °C region.

Direct comparison of CO oxidation activities of prepared specimens during TPR3 is presented in *Fig. 21*. We choose TPR3 run for comparison purpose, because at TPR1 and TPR2 the catalysts are not stabilized enough - i.e. activity was changed after repeated TPR procedure.

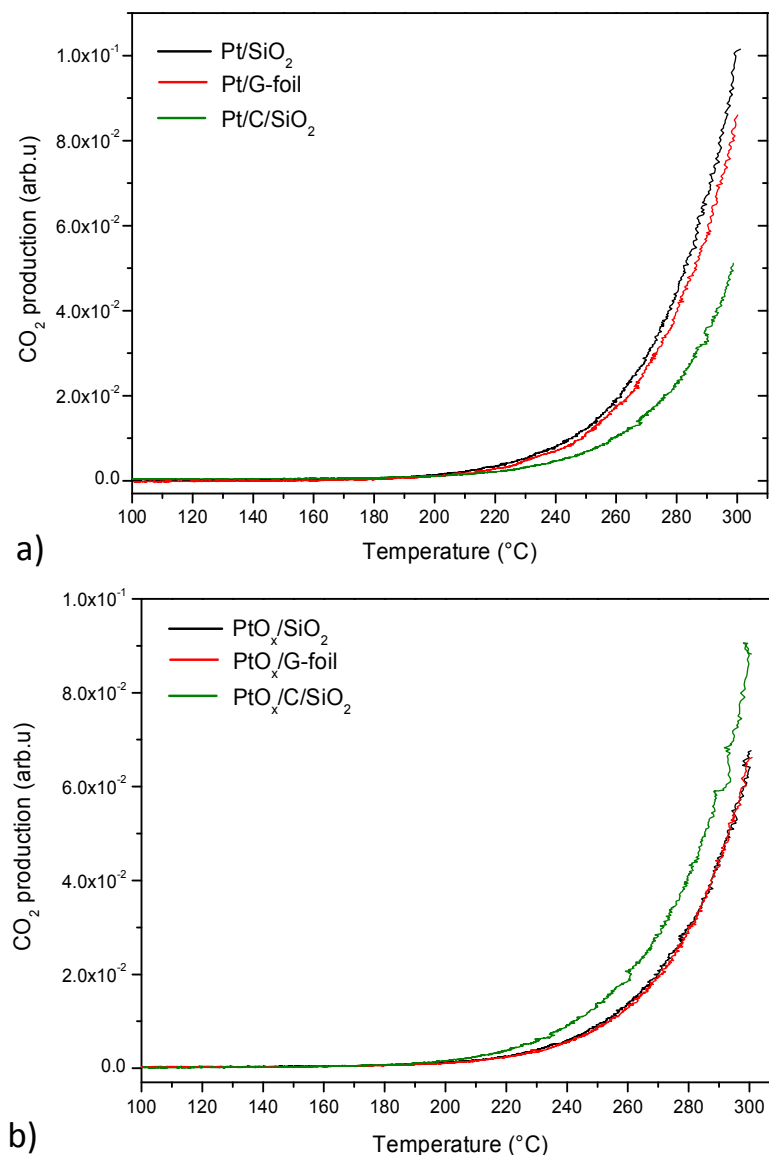


Fig. 21. Comparison of CO oxidation activities at TPR3 stages of the following samples: a) metallic platinum deposited on different substrates (Pt/SiO₂, Pt/G-foil and Pt/C/SiO₂); b) platinum oxide deposited on the same substrates (PtO_x/SiO₂, PtO_x/G-foil and PtO_x/C/SiO₂).

Among Pt thin films the highest CO oxidation activity exhibited Pt/SiO₂ (*Fig. 21a*). Since the deposition procedure of specimen was carried out in the argon atmosphere, we obtained growth of metallic platinum layer which consists of Pt⁰ species as confirmed by XPS (see subchapter 4.3.1). It is well agreed that CO

oxidation on metallic platinum surfaces takes place via L-H mechanism [24], where chemisorbed CO molecules react with dissociatively adsorbed O₂ to produce CO₂ (Fig. 11a). As prepared Pt/SiO₂ specimen has flat and homogeneous morphology, but after CO oxidation TPR3 the nanoparticles and patches have appeared on the surface of the specimen (Fig. 13a, d). We supposed that such rough morphology leads to a higher activity at TPR2 compared to TPR1. This is because nanoparticles generally demonstrated higher activity than the corresponding flat surface [25]. CO₂ yields at TPR2 and TPR3 stages of such sample are almost the same and demonstrated higher value compared to the TPR1 (Fig. 15). Also activation energies of TPR2 ($E_a = 95 \pm 2.5$ kJ/mol) and TPR3 ($E_a = 85 \pm 2$ kJ/mol) are similar and have higher values compared to those of TPR1 ($E_a = 58 \pm 0.5$ kJ/mol). Therefore, we assumed that stabilization process of Pt/SiO₂ takes place within TPR1 cycle.

Regarding platinum deposited on G-foil substrate (Pt/G-foil) it exhibited 9% lower CO₂ yield than Pt/SiO₂ sample during TPR3 stage (Fig. 21a). Also from Fig. 16 it can be seen that CO₂ yields of TPR2 and TPR3 are not similar – i.e. sample is not stabilized after TPR1 unlike the Pt/SiO₂ one. Morphology of Pt/G-foil sample after TPR3 stages exhibited coalescence of Pt in grains which resulted in uncovered G-foil substrate (Fig. 13e). Since G-foil is not active for CO oxidation, thus, we observed lower activity compared to Pt/SiO₂, where coalescence of platinum was not accompanied with uncovering the SiO₂ substrate (Fig. 13d). Among metallic platinum specimens, the Pt/C/SiO₂ sample exhibited lowest activities, which produce about 2 times less CO₂ compared to Pt/SiO₂ (Fig. 21a). After the TPR3 run on Pt/C/SiO₂ sample, the surface Pt coalesced in clusters (Fig. 13f), which resulted in opening the C interlayer even more (approx. 50%) compared to other Pt specimens. The morphology observation is well agreed with the activity data – i.e. Pt/C/SiO₂ sample, which has about 50% of surface covered by active platinum exhibited two times less CO₂ yield compared to Pt/SiO₂ one during TPR3 stage (Fig. 21a).

The CO oxidation behavior of PtO_x deposited on aforementioned substrates is different compared to metallic Pt. Since deposition procedure carried out in O₂ atmosphere, we obtained platinum oxide layer (PtO_x). The key feature of such layer is because it contains lattice oxygen, which can be easily removed (i.e. reduction of PtO_x) by exposing the catalyst with CO, H₂ or methanol or by simply thermal decomposition [26]. XPS analysis of thermal decomposition of PtO_x layer in UHV conditions is reported in [26], where surface of the as prepared sample at room

temperature exhibits platinum in Pt⁴⁺ oxidation states (in form of PtO₂ and Pt(OH)₄). During the heating up procedure oxide layer gradually started to reduce (at 150 °C) from Pt⁴⁺ state to almost completely metallic phase Pt⁰ (upon 380 °C). Furthermore, complete reduction of such layer (Pt⁴⁺ → Pt⁰) in a gas flux containing CO is completed at the temperature near 230 °C. Since, we observed the activity of the same PtO_x layers, so we expected similar reduction process during the realistic CO oxidation condition in the microreactor. Regarding the activity of PtO_x/SiO₂ sample we can see the elevated CO₂ production between 180 °C and 260 °C at TPR1 (*Fig. 18*). The linear parts of Arrhenius plot (region 1, region 2) reflect the stability regions of CO oxidation, while non-linear transition region within 200 - 260 °C indicates change of the reaction conditions. We suppose that at such temperature (200 - 260 °C) CO₂ production is enhanced by oxygen from oxidized Pt, which promotes oxidation of CO adsorbed preferentially on metallic Pt. Above 260 °C (and in the following TPR2 and TPR3), CO oxidation presumably proceeds via MvK mechanism where platinum layer is alternately reduced and re-oxidized, which leads to roughening of the surface of catalysts (*Fig. 12*). During TPR1 activation energy at region 1 ($E_a = 88 \pm 2$ kJ/mol) is lower than at region 2 ($E_a = 93 \pm 2.4$ kJ/mol), which suggests easier formation of CO₂ when oxygen is present in catalyst layer (inset in *Fig. 18*). TPR2 takes place on already reduced metallic platinum surface (Pt⁰), therefore no elevated CO₂ production in 180 - 260 °C region was observed. Activation energies of TPR2 and TPR3 in 280 - 260 °C region are similar to the same region of TPR1 (see inset in *Fig. 18*) which confirms our assumption that TPR2 and TPR3 takes place on the metallic Pt. Also we observed 1.5 times higher CO₂ yield after repeating the TPR procedure on PtO_x/SiO₂. We supposed that it is due to forming the Pt grains, which results in increasing the active surface area of thin film (*Fig. 14d*).

CO oxidation activity of PtO_x/G-foil sample (*Fig. 19*) is very similar to the PtO_x/SiO₂ one, only E_a were slightly different, because various supports had been used (SiO₂ and G-foil). Also morphology of such samples after the TPR3 stage is nearly the same (*Fig. 14 d, e*). Among prepared PtO_x system the highest CO₂ yield at TPR3 stages exhibited Pt/C/SiO₂ specimen (*Fig. 21b*). Such sample demonstrated similar surface morphology (*Fig. 14e*) and CO oxidation behavior during three TPRs as previous PtO_x system. Higher activity during TPR3 can be explained by influence

of C interlayer on forming the smaller Pt grains in size compared to other samples (Fig. 14c, d, e).

In this chapter we compared the mechanism of CO oxidation reaction on Pt and PtO_x deposited on SiO₂, G-foil and C/SiO₂ substrates. CO oxidation on metallic Pt layer proceeded through L-H mechanism and depends on type of the substrates. Platinum deposited on SiO₂ substrate (Pt/SiO₂) showed higher CO₂ yield compared to Pt supported by G-foil and especially C interlayer. It is due to the stability of Pt/SiO₂ system after TPR1 stages. In contrary, using G-foil and C/SiO₂ as substrates leads to coalescence of platinum film in grains and uncovering inert carbon substrates. Such substrates are inactive for CO oxidation reaction, thus, lower CO₂ yields were observed compared to Pt/SiO₂. Different CO oxidation behavior demonstrated PtO_x layer deposited on aforementioned substrates. During TPR1, PtO_x reduced to metallic Pt (Pt⁴⁺ → Pt⁰) which accompanied with an increasing of the surface area of the sample. Lattice oxygen in PtO_x promotes CO oxidation below 250 °C. Above 250 °C (and in the following TPRs) the surface of the catalyst is reduced and re-oxidized via MvK mechanism. Regarding the substrates, PtO_x supported by either substrate performed similar, with minor advantage when PtO_x deposited on C interlayer. Both 10 nm thick Pt and PtO_x thin films exhibited similar CO oxidation activity. But PtO_x layer has advantages such as lower Pt content, ability to self-activation and independency of the type of substrates.

3.4. CO oxidation on rare earth oxides (REOs) nanoparticles

Nowadays, REOs have wide usage in many applications such as automobiles, wind turbines and computers [27]. Due to unique properties of REOs materials they can be used as a solid electrolyte with good ionic conductivity for solid oxide fuel cell (SOFC), laser materials and in catalysis field [28,29]. Regarding catalysis, it is well known that using pure materials is too expensive. Therefore, it is a usual practice to disperse active catalyst in the inert material with high surface area. Sol-gel chemistry allows preparing a unique hybrid catalyst material, where catalytically active material is dispersed in cheap inert oxide matrix. This leads to the decrease of the cost of the material, while keeping the same or even better catalytic activity.

Through the collaboration between Charles University and Institute for Applied and Physical Chemistry (IAPC) in Bremen (Germany), alumina stabilized

ceria, praseodymia, samarium and terbium (both xero- and aerogels (AG)) were prepared with help of sol-gel method using alumina support matrix [30]. The ratio of the precursors was adjusted in such way that the prepared catalyst contained 20% (wt) of REOs and 80% (wt) of alumina. Then, each catalyst was calcined (heated in air) at 650 °C and 1000 °C. Ambient pressure CO oxidation tests over REOs xerogels and reference corresponding pure REOs samples were done on continuous flow fixed bed reactor at IAPC. In order to better understand the heat and mass transfer of the catalysts, CO oxidation tests were performed on the alumina stabilized aerogel samples (Ce/Al AG 650 °C, 1000 °C; Pr/Al AG 650 °C, 1000 °C; Sm/Al AG 650 °C, 1000 °C and Tb/Al AG 650 °C, 1000 °C) as well as reference pure REOs powders (CeO₂ 650 °C, 1000 °C; Pr₆O₁₁ 650 °C, 1000 °C; Sm₂O₃ 650 °C, 1000 °C and TbO₂ 650 °C, 1000 °C) using laboratory microreactor system at Department of Surface and Plasma Science in Prague. For this purpose we used the high temperature sample holder for powder catalysts (*Fig. 9*). Its construction permits a reliable measurement of the small amount of the catalyst (1-2 mg) without dilution ensuring good temperature control of it. Working gas mixture was 6% (vol.) CO + 20% (vol.) O₂ diluted with helium buffer gas with total the flow rate of the gas feed mixture of 5 sccm. All catalytic tests were done in temperature range between 200 °C and 550 °C, because CO oxidation over REOs takes place above 300 °C [31]. In order to obtain a steady-state condition of products at each analyzed temperature, a temperature steps heating procedure (10 min per temperature; 25 °C steps with heating rate of 10 °C per min) was applied. For each measurement we used 1 mg of catalyst attached by a drop of acetone to the bottom glass of sample holder. The results are reported as CO conversion (*CO%*, i.e. - the percentage of CO converted to CO₂ in the reaction cell) versus temperature (*T*, °C). CO conversion was defined as:

$$CO\% = \frac{CO_2(signal)}{CO(signal) + CO_2(signal)} \times 100 \quad (8)$$

where *CO₂ (signal)* and *CO (signal)* are QMS signal intensities of the CO and CO₂ respectively.

The specific surface area (SSA) for pure ceria and praseodymia as well as its aerogels were determined by nitrogen adsorption at 77 K. As we can see in *Table 1*,

generally SSA of samples calcined at 650 °C is higher than 1000 °C. Also each alumina stabilized REOs has higher surface area than corresponding pure REOs catalyst.

Notation	Temperature (°C)	BET specific surface area (m ² /g)
CeO ₂	650	45
CeO ₂	1000	1
Ce/Al AG	650	261
Ce/Al AG	1000	100
Pr ₆ O ₁₁	650	12
Pr ₆ O ₁₁	1000	1
Pr/Al AG	650	204
Pr/Al AG	1000	19

Table 1. Specific surface area of the alumina stabilized ceria and praseodymia aerogels and reference ceria and praseodymia calcined at different temperatures [30].

SEM images of the prepared samples (*Fig. 22*) demonstrated the morphology differences between pure praseodymia, samaria, terbia and corresponding alumina stabilized samples calcined to 650 °C.

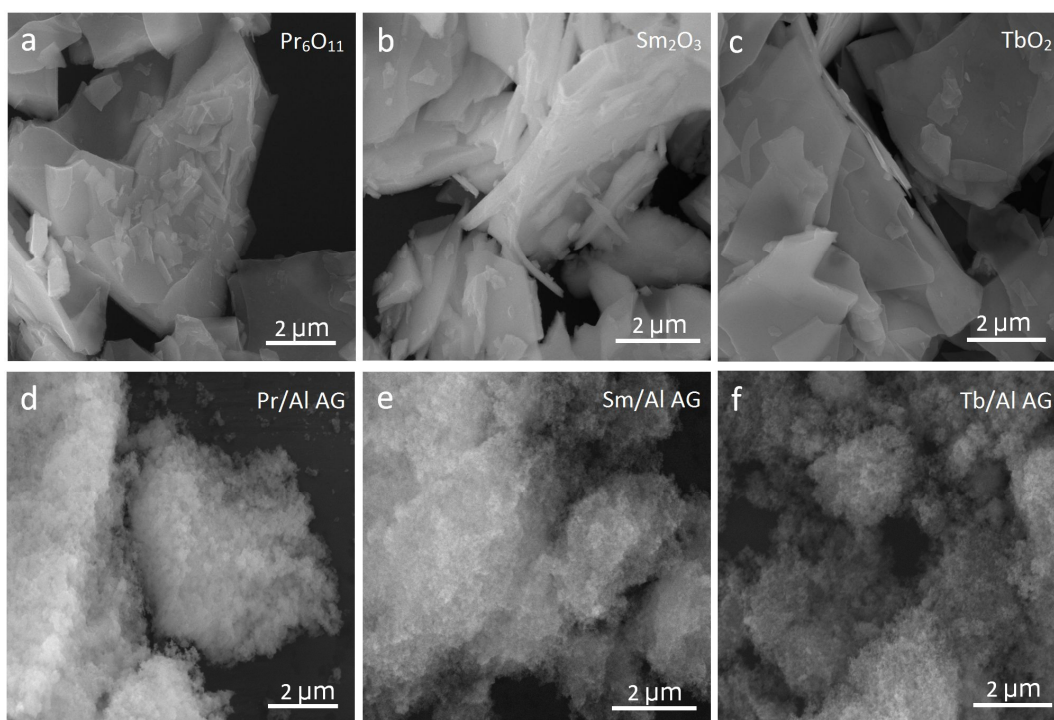


Fig. 22. SEM images of pure REOs and corresponding alumina stabilized samples each calcined at 650 °C: Pr₆O₁₁ powder (a) and Pr/Al AG (d); Sm₂O₃ powder (b) and Sm/Al AG (e); TbO₂ powder (c) and Tb/Al AG (d).

Pure Pr_6O_{11} specimen exhibited about 10 μm particles with sharp edges, while Pr/Al AG sample demonstrated similar size of particles, but with very porous, wadding structure (*Fig. 22 a, d*). Such morphology difference was observed for all pure REOs and corresponding aerogels calcined to 650 $^\circ\text{C}$ and 1000 $^\circ\text{C}$ (1000 $^\circ\text{C}$ samples not shown due to similar morphology differences as 650 $^\circ\text{C}$ ones between pure and alumina stabilized REOs), which well agreed with SSA data.

Transmission electron microscopy (TEM) images of Pr/Al AG specimen exhibited open-cell morphology with 4 - 6 nm ligaments, which are separated by pores (*Fig. 23a*). Regarding the Ce/Al AG specimen (*Fig. 23b*), it exhibited distinctly more dense morphology with shorted ligaments in size (about 2 - 4 nm) compared to the praseodymia aerogel.

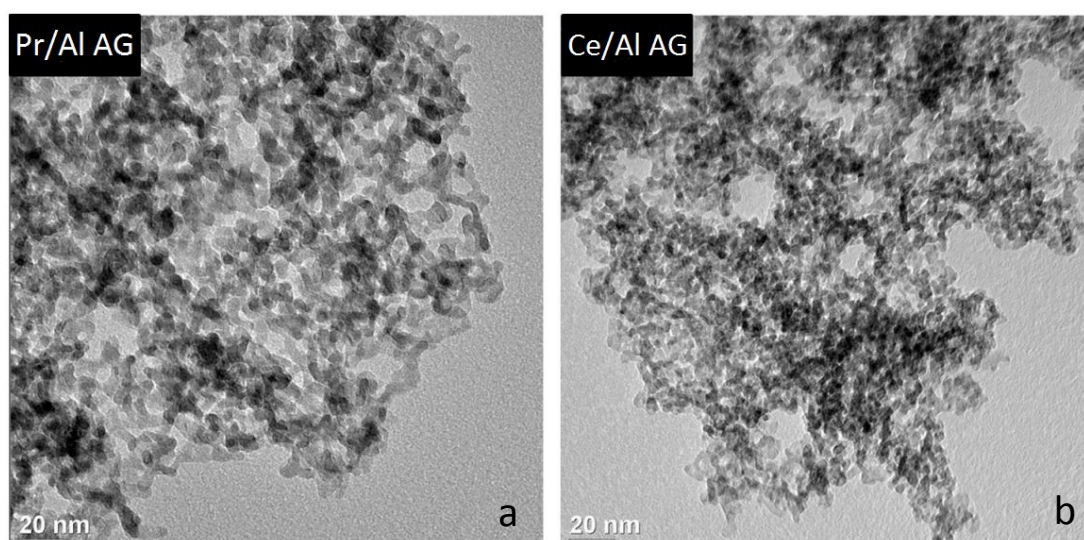


Fig. 23. TEM micrographs of Pr/Al AG (a) and Ce/Al AG (b) samples [30].

CO oxidation activity comparison between alumina stabilized ceria aerogels (Ce/Al AG 650 $^\circ\text{C}$; Ce/Al AG 1000 $^\circ\text{C}$) and reference pure ceria samples (CeO_2 650 $^\circ\text{C}$; CeO_2 1000 $^\circ\text{C}$) are presented in *Fig. 24a*. For both ceria aerogels and pure ceria samples activity was higher when calcination temperature was lower. The CeO_2 650 $^\circ\text{C}$ specimen demonstrated 50% of CO conversion at highest reaction temperature, while CeO_2 1000 $^\circ\text{C}$ showed almost no activity (around 3% of CO conversion). In contrary Ce/Al AG 1000 $^\circ\text{C}$ demonstrated up to 25% of CO conversion, while Ce/Al AG 650 $^\circ\text{C}$ specimen exhibited comparable CO conversion to the pure CeO_2 650 $^\circ\text{C}$. The catalytic activity of pure and alumina stabilized praseodymia is higher for samples which were calcined at 650 $^\circ\text{C}$ (*Fig. 24b*).

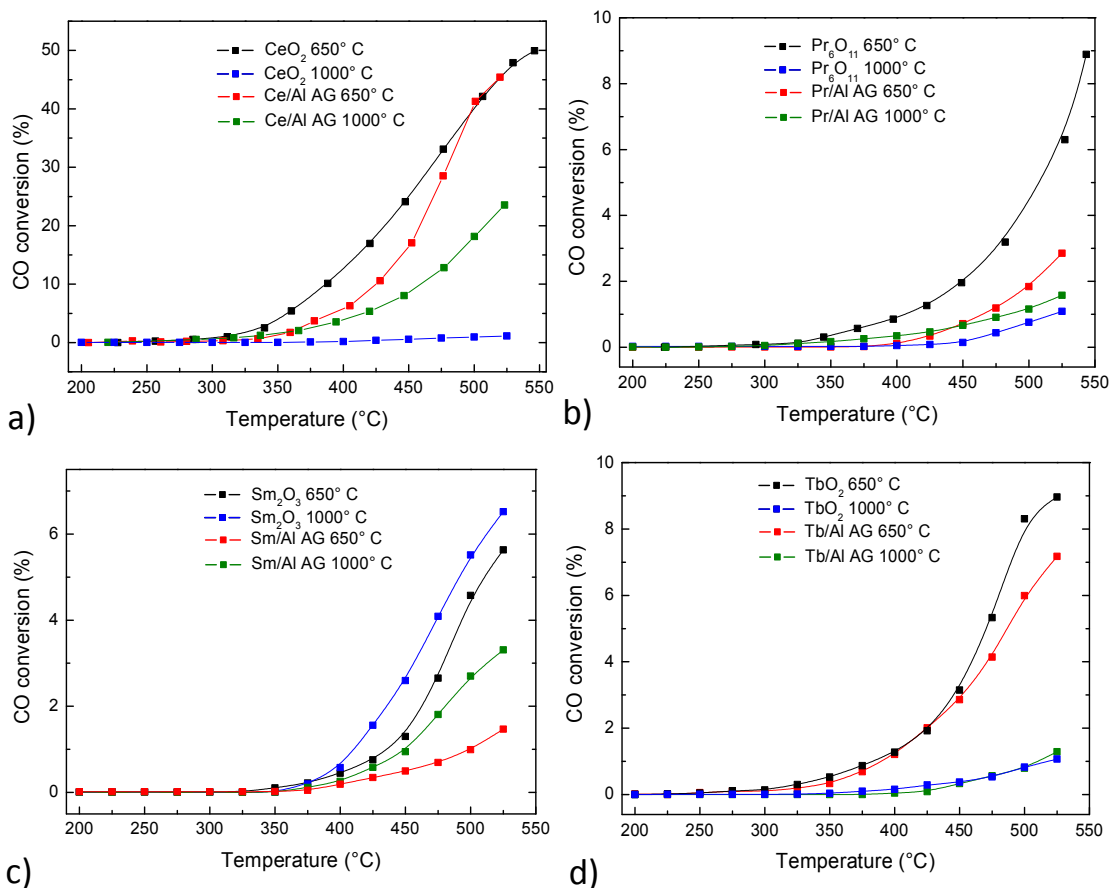


Fig. 24. Conversion of CO as a function of temperature of pure REOs and alumina stabilized REOs both calcined at 650 °C and at 1000 °C: pure CeO₂ and corresponding Ce/Al AG (a); pure Pr₆O₁₁ and corresponding Pr/Al AG (b); pure Sm₂O₃ and corresponding Sm/Al AG (c); pure TbO₂ and corresponding Tb/Al AG (d).

Pure praseodymia calcined at 650 °C demonstrated up to 2 time higher catalytic activity than alumina stabilized praseodymia. Regarding samples calcined at 1000 °C, both Pr₆O₁₁ and Pr/Al AG exhibited similar CO conversions (around 2%). From Fig. 24c we can see that pure samarium catalyst (Sm₂O₃ 650 °C and Sm₂O₃ 1000 °C) exhibits about two time higher CO conversion than alumina stabilized samples (Sm/Al AG 650 °C and Sm/Al AG 1000 °C). In contrary to previous measurements, CO conversion of samaria samples calcined at 1000 °C (both pure and alumina stabilized) are higher than samples calcined at 650 °C. Catalytic behavior of terbium samples do not depend much on the form of the catalyst. Both pure and aerogel samples demonstrated almost same CO conversions in whole temperature range (Fig. 24d). However, samples calcined at 650 °C showed about 8% of CO conversion, while at 1000 °C exhibited only 2% of CO conversion.

Among prepared alumina stabilized REOs, the most favorable catalytic activity demonstrated ceria aerogels calcined at 650 °C compared to pure reference ceria (*Fig. 24a*). First of all, Ce/Al aerogels together with pure CeO₂ samples (both calcined at 650 °C), exhibited 50% of CO conversion at highest reaction temperature (at 550 °C), which is around 5 times higher than other REOs catalysts. Taking into account, that the amount of active ceria in Ce/Al AG catalyst was 20% (wt), it is an advantage compared to reference pure ceria catalyst. Morphology observation together with BET surface area data confirmed, that the key factor of the high activity of ceria aerogel is increased of SSA compared to ceria reference sample (see *Table 1*: 261 → 45 m²/g). Increasing the calcinations temperature of the ceria samples (from 650 °C to 1000 °C) leads to a loss of SSA, resulting in activity decline. Weak CO oxidation activity of CeO₂ 1000 °C sample can be explained by drastically decreasing of SSA compared to CeO₂ 650 °C (45 → 1 m²/g), while ceria aerogels demonstrated only 2.6 time decreasing of SSA (261 → 100 m²/g). Thus, Ce/Al AG 1000 °C showed about 30% of CO conversion at highest reaction temperature. In addition to good activity of Ce/Al aerogels, such catalyst demonstrated a good stability against sintering. This means that even after calcining the Ce/Al AG sample to 1000 °C, it exhibited some activity (25% of CO conversion), while pure CeO₂ 1000 °C sample demonstrated weak activity (*Fig. 24a*).

All pure and alumina stabilized praseodymia samples showed lower CO oxidation activity (about 5 times) than ceria ones (*Fig. 24b*). In case of 650 °C catalysts, aerogel exhibits 3 times lower value of CO conversion than pure praseodymia (*Fig. 24b*). Measured BET surface area of Pr/Al AG 650 °C is higher than pure Pr₆O₁₁ 650 °C (204 → 12 m²/g). From such observation we can conclude that Pr/Al AG with higher surface area is not as active as the pure praseodymia. Regarding 1000 °C samples, BET area is 1 m²/g for pure catalyst and 19 m²/g for alumina stabilized one. In this case, higher surface area of alumina stabilized sample leads to very small improvement of CO oxidation activity.

Samaria samples exhibit completely different activity behavior compared to previous REOs (*Fig. 24c*). At first, both aerogels and pure samarium calcined at 1000 °C has higher CO conversion compared to samples calcined at 650 °C. At second, alumina stabilized samples are worst in case of activities than reference pure samaria. It is due to intrinsic low activity, which leads to approximately similar

reactivity for both 650 °C and 1000 °C samples. In case of aerogels, here, increased sintering temperature leads to increasing the CO oxidation activity.

Regarding terbia catalysts (*Fig. 24d*), practically no activity differences were observed between aerogels and pure terbia samples. Only calcination temperature of samples was an important factor. Increasing calcination temperature to 1000 °C resulted in 4 times loss of CO oxidation activity. However, taking into account, smaller amount of terbia in Tb/Al aerogels (only 20% (wt)), it is a clear advantage compared to the pure terbium material.

In this chapter we prepared alumina stabilized REOs by sol-gel method and compared their CO oxidation activities to the pure REOs catalysts using laboratory microreactor system. Among prepared samples only Ce/Al AG exhibited superior CO oxidation activities compared to corresponding pure CeO₂ material. The Ce/Al AG contained only 20% (wt) of pure ceria which is dispersed in alumina matrix. High surface area of such material resulted in great catalytic activities (in regards to ceria content) and good sintering stability.

3.5. CO oxidation on samaria nanoparticles

Through the collaboration between Charles University and University of Bremen (under short-term scientific mission STSM), we synthesized different shaped samarium oxide (Sm₂O₃) nanoparticles and compared their CO oxidation activities. Such catalysts were prepared and characterized by infrared diffraction (IR) method at IAPC in Bremen, while morphology characterizations and reactivity tests were done at Department of Surface and Plasma Science in Prague.

Generally samarium oxide has two different stable phases: monoclinic and cubic. We tried to synthesize these two crystal phases. As we can see from *Fig. 25* the monoclinic phase should be obtained by applying the calcination procedure (heating in air) for catalyst above 800 °C, while cubic phase should be obtained below 800 °C [32]. The more important role plays the morphology and particle size. The influence of different morphologies of the Sm₂O₃ was carried out by using different precursors. Therefore, we started the calcinations of two different precursors at four different temperatures, in attempt to obtain different phases as well as different particles sizes and morphology of samaria. Moreover, a crystal sample of samarium oxide was included as reference.

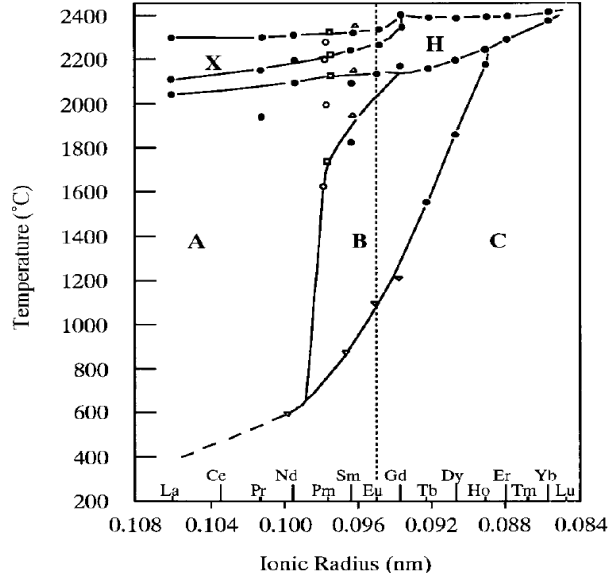
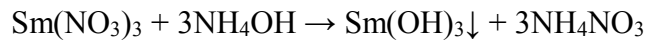
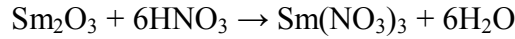
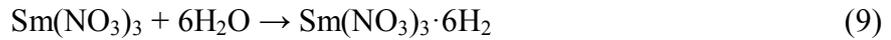


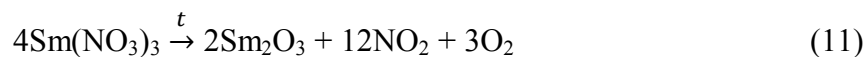
Fig. 25. The two different phases of stable samarium oxide: monoclinic (a) and cubic (b) and their dependence on temperature [32].

At first $\text{Sm}(\text{OH})_3$ as one of the precursors needs to be synthesized. We focused on two different ways:



The first way (reaction 9) was simply cooking the samarium oxide for 12 h in water to obtain crystal particles of the hydroxide. The second way (reactions 10) involving urea ($\text{CO}(\text{NH}_3)_2$) was quite more difficult, since the molar amounts were unknown and less information given. Besides the second way is more suitable because a samarium hydroxide nanopowder could be obtained. This is because of the in situ forming and the reaction of small amounts of hydroxide ions formed from the urea using heating [33].

The precursors and the reference were calcined at 500, 600, 700, 800, 900 and 1000 °C respectively, for 48 h to obtain the samarium oxide. The following reactions appeared while heating:



During calcination procedure the reference sample (Sm_2O_3) should simply change its crystals phase. The hydroxide ($\text{Sm}(\text{OH})_3$) and especially the nitrate ($\text{Sm}(\text{NO}_3)_3$) should form nanoparticles because of the gases and the water released.

To make sure that the synthesized samples were the correct and pure compounds IR spectra were measured (*Fig. 26*).

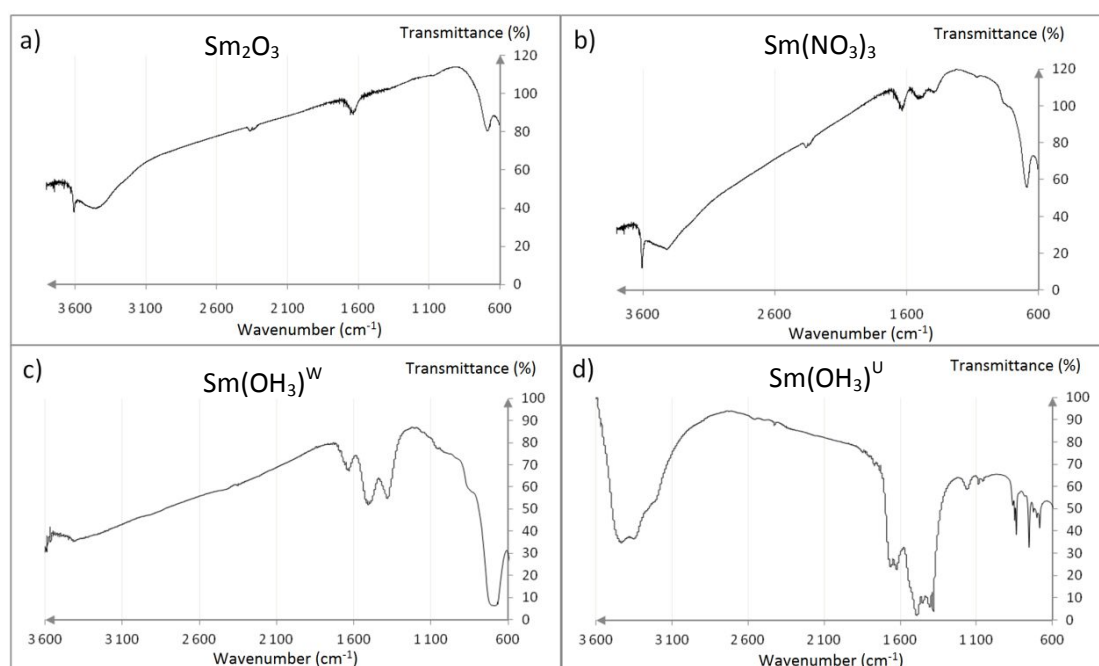


Fig. 26. IR-spectra obtained from samarium oxide crystal reference sample (a), nitrate precursor (b), samarium hydroxide obtained from oxide boiled in water (c) and samarium hydroxide obtained by using urea as precursors (d).

The spectra show in two cases a high transmittance that is mainly decided by the used potassium bromide reference which was weak. Still one can qualitatively analyze the result. The reference Sm_2O_3 (see *Fig. 26a*) shows the main vibration of either Sm-O probably at 620 cm⁻¹ and water at 1620 cm⁻¹ as well as at around 3400 cm⁻¹ [34]. The single absorption around 3600 cm⁻¹ might belong to the bonded

O-H groups on the surface. The weak adsorption at around 2400 cm^{-1} belongs to CO_2 from the air surrounding the sample. By comparing the samarium oxide obtained from the nitrate precursor ($\text{Sm}(\text{NO}_3)_3$) has additional absorptions at $1400\text{-}1500\text{ cm}^{-1}$ (see *Fig. 26b*) which belongs to N-O vibration [35]. Although the whole nitrate should be decomposed these might belong to still existing nitrate species or to nitrate from the nitric acid, with which the crucible was cleaned. As a result, nearly pure samaria was obtained by calcination the nitrate.

Further research has been made on the two synthesized samarium hydroxides; the spectra of the synthesized compounds are quite different. The spectrum of the hydroxide obtained by boiling the oxide in water ($\text{Sm}(\text{OH}_3)^{\text{W}}$) presented in *Fig. 26c*, indicates that the hydroxide was not obtained. It is very similar to the oxide samples and there seems to be no characteristic O-H vibration excluding from water. The hydroxide which was synthesized by using urea ($\text{Sm}(\text{OH}_3)^{\text{U}}$) seems to be quite good result (see *Fig. 26d*). One can see a lot of water in addition very intensive absorption around 1600 cm^{-1} . This absorption belongs to N-O vibration and water. This is because the sample was synthesized by using nitric acid. Very interesting is that the absorption around 620 cm^{-1} which belongs to the Sm-O vibration almost disappear, whereas new absorption occurred which should belong to the O-H vibration and its Sm-O connection around $700, 800$ and 1200 cm^{-1} respectively [34].

Morphology of prepared samples (Sm_2O_3 , $\text{Sm}(\text{OH})_3$ made by using urea and $\text{Sm}(\text{NO}_3)_3$) was observed by SEM technique. In order to estimate clear morphology differences, only specimens calcined to $500\text{ }^\circ\text{C}$ and $1000\text{ }^\circ\text{C}$ were observed. Pure reference Sm_2O_3 powder calcined to $500\text{ }^\circ\text{C}$ exhibits approx. $0.1\text{ }\mu\text{m}$ particles merged to large clusters, while samaria calcined to $1000\text{ }^\circ\text{C}$ has particles with size of $0.5\text{ }\mu\text{m}$ (see *Fig. 27a, d*). From *Fig. 27b* it can be seen that $\text{Sm}(\text{OH})_3$ calcined to $500\text{ }^\circ\text{C}$ exhibited a wired structure with approx. $5\text{ }\mu\text{m}$ long wires. But after calcination procedure to $1000\text{ }^\circ\text{C}$ lengths of $\text{Sm}(\text{OH})_3$ wires decreased to about $1\text{ }\mu\text{m}$ and catalyst exhibited more like particle structure (*Fig. 27e*). Samarium oxide made from nitrates precursor ($\text{Sm}(\text{NO}_3)_3$) calcined to $500\text{ }^\circ\text{C}$ exhibited plate-like morphology with clusters sized varies from 1 to $10\text{ }\mu\text{m}$ in diameter (*Fig. 27c*). After increasing the calcination temperature ($1000\text{ }^\circ\text{C}$) morphology of catalyst did not change much, only slightly larger clusters (up to $20\text{ }\mu\text{m}$) were observed (*Fig. 27f*).

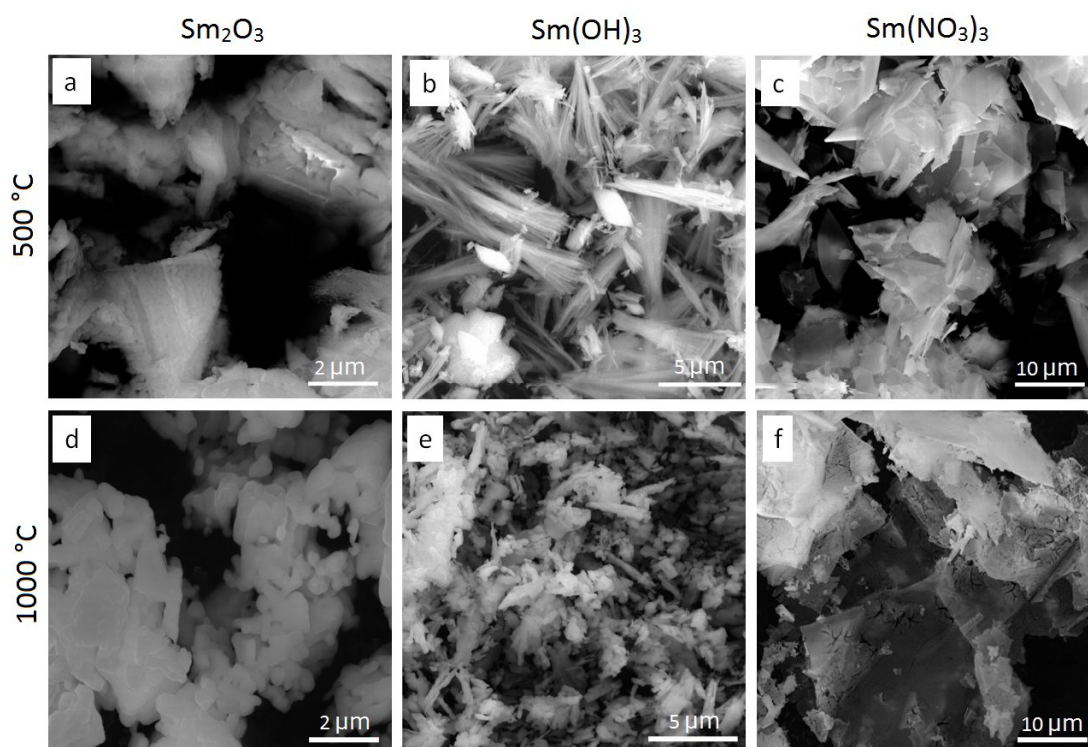


Fig. 27. SEM micrographs of samaria made from different precursors calcined to 500 °C and 1000 °C: reference Sm_2O_3 samples calcined to 500 °C (a) and 1000 °C (d); $\text{Sm}(\text{OH})_3$ calcined to 500 °C (b) and 1000 °C (e); $\text{Sm}(\text{NO}_3)_3$ calcined to 500 °C (c) and 1000 °C (f).

The most REOs are catalytic active including samarium oxide but different suggestions have been made. Samaria as catalysts for CO oxidation usually used as a dopant [36,37] and have not been used as a single catalyst component. So it is important to check CO oxidation on reference Sm_2O_3 and compare the activities with samaria made from different precursors i.e. - $\text{Sm}(\text{NO}_3)_3$ and $\text{Sm}(\text{OH})_3$. If activities of samaria prepared from different precursors will be better compared to pure samaria, then such catalysts could replace the Sm_2O_3 dopant in catalysts composition. Therefore CO oxidation tests were performed on the laboratory microreactor system. Similar experimental conditions as for previous experiments (*subchapter 3.4*) were applied.

From *Fig. 28a* we can see that reference Sm_2O_3 catalyst calcined to 500 °C and 600 °C exhibited almost the same CO conversion, but both reached only 5% level at highest reaction temperature (550 °C). Sm_2O_3 calcined to 900 °C and 1000 °C demonstrated only 2% of CO conversion at 550 °C. CO conversion of $\text{Sm}(\text{OH})_3$ powders reached 5% level and decrease with increasing the calcination temperatures (*Fig. 28b*). Catalytic activity of samaria made from nitrate precursor ($\text{Sm}(\text{NO}_3)_3$)

calcined to 500 °C exhibits 18% of CO conversion (Fig. 28c). Rest of prepared $\text{Sm}(\text{NO}_3)_3$ powders has a similar catalytic activities as reference ones (up to 4% of CO conversion).

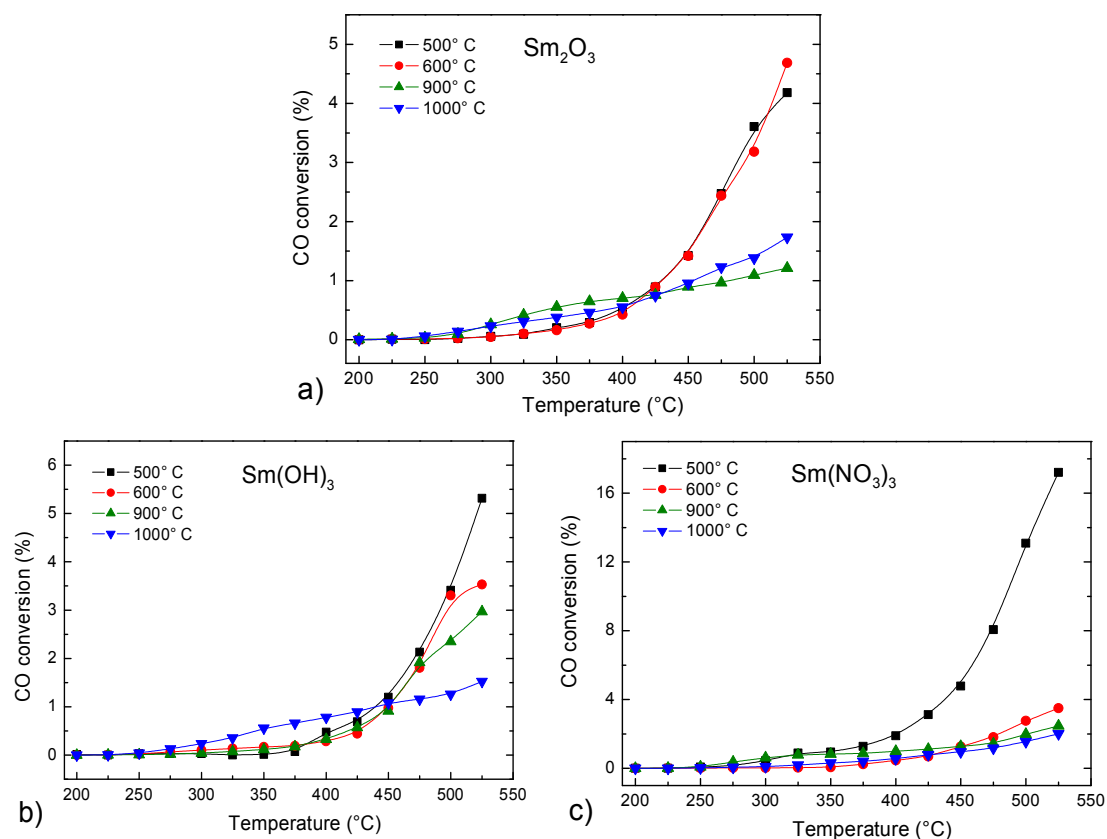


Fig. 28. Conversion of CO as a function of temperature of Sm_2O_3 (a), $\text{Sm}(\text{NO}_3)_3$ (b) and $\text{Sm}(\text{OH})_3$ (c) catalysts, all calcined to 500, 600, 900 and 1000 °C.

From the activity plots two conclusions can be made. First, we observed the decrease of the catalytic activities with the increasing of the calcination temperatures on each catalyst. It is due to increased size of clusters and grain of catalytic powder, which leads to drastically losses of active surface area (see Fig. 27). Lower surface area leads to decreasing the amounts of active sides on which molecules of both CO and O_2 adsorbs and reacts to form CO_2 . Second, samaria samples prepared from different precursors as well as reference Sm_2O_3 exhibited similar CO oxidation activity. Only $\text{Sm}(\text{NO}_3)_3$ calcined to 500 °C demonstrated relatively high 18% level of CO conversion. Such high activity can be explained by nanocrystal structure of $\text{Sm}(\text{NO}_3)_3$ whereas reference Sm_2O_3 has bigger crystal size. Besides, $\text{Sm}(\text{OH})_3$ has a wired morphology which generally has a lower surface area compared to nanopowders. As a result, samaria made from nitrate precursor ($\text{Sm}(\text{NO}_3)_3$)

outperformed reference pure samaria in CO oxidation activity tests. Such catalyst can be recommended as a potential candidate to replace the Sm_2O_3 dopant in composite catalyst for CO oxidation reaction.

4. Methanol oxidation

4.1. Motivation

Since the problems concerning air pollutants (described in *subchapter 3.1*) became more pronounced, humanity increasingly begins to invest renewable energy sources that replace conventional fuels, thus, reduce the environmental impact of the use of energy. Solar battery, wind and hydro power stations are options in case of production of electricity. But inconstancy of such sources (sunlight, wind) and expensiveness of technology still makes it hard to compete with traditional thermal power stations [38]. In the small-scale applications, particularly in transport, alternative fuel vehicle becomes an object of investigation. Such vehicle runs on “cleaner” alternative fuels and offers the technology of powering an engine without the usage of petroleum. Among those technologies stand out a FC devices, that can generate electricity by electrochemical oxidation of fuel [39]. There are several types of FC that differ in consumed fuel, working temperature and application side. Things that unite them are production of only electricity and environmentally friendly waste, such as water vapor and CO₂. Widespread application of FC may lead to a reduced consumption of oil and contribute to a reduction of environmental pollution. In case of PEMFC, thermal efficiency (35-40%) is higher than that of petrol-fueled combustion engines (25-30%) [40]. When PEMFC using in cars, disadvantages concerning hydrogen fuel are safety, refueling, and storage. One of the solutions to overcome these problems is on-board hydrogen generation from a suitable liquid fuel. Among them methanol (CH₃OH) is the best candidate for such purpose due to high hydrogen to carbon ratio, high energy density and good availability [41]. Moreover methanol has low boiling point and no C-C bound, thus, it can be reformed at relatively low temperature. The most common methods of converting methanol to hydrogen are partial oxidation of methanol (POM), methanol decomposition (MD) and steam reforming of methanol (SRM) (see *Table 2*).

MD reaction yields hydrogen and carbon monoxide, also known as synthesis gas. Such reaction is not suitable for PEMFC without further pretreatment, because of CO poisoning of the noble-metal electrodes (see *subchapter 3.1*).

Name of the reaction	Reaction route	T, °C	By-products	ΔH° (kJ · mol ⁻¹)
POM	$\text{CH}_3\text{OH} + \frac{1}{2} \text{O}_2 \rightarrow 2\text{H}_2 + \text{CO}_2$	150-275	CO, CH ₄ , H ₂ O	-192,2
MD	$\text{CH}_3\text{OH} \rightarrow 2\text{H}_2 + \text{CO}$	over 300	CO, CH ₄ , H ₂ O	91
SRM	$\text{CH}_3\text{OH} + \text{H}_2\text{O} \rightarrow 3\text{H}_2 + \text{CO}_2$	250-300	CO, CH ₄ , H ₂ O	49,4

Table 2. Methanol reforming reactions.

SRM produces more favorable H₂/CO₂ ratios, but it is an endothermic reaction which requires a heat supply. This is typically realized by burning a fuel, which accounts for additional environmental contamination and degrades the overall efficiency. POM is an exothermic reaction which does not need an extra heat. It uses oxygen or air instead of steam and does not require water vapor compared to SRM, which results in smaller reactor volume and simpler reactor setup. However, POM and SRM reactions both are widely used for conversion of methanol to hydrogen, depending on the application.

Generally, the catalyst for methanol oxidation reactions is in form of nanoparticles and is based on transitional metals supported on various metal oxides. For POM reaction the common studied catalytic systems are Cu, Pd supported on ZnO, CuO, Al₂O₃ [42,43,44]. Methanol decomposition catalysts are mainly Pt, Cu, Ni with various supports such as SiO₂, CeO₂, TiO₂, Pr₂O₃ [45,46,47]. Catalysts for SRM are mostly Pd or Cu as active metal supported on Al₂O₃, ZnO or ZrO₂ [48,49,50].

Competition in the catalyst industry and wide range of methods and techniques available in modern laboratories results in increasing the number of reports concerning new preparation approaches for catalysts. In case of the catalyst for methanol oxidation reactions, in addition to classical demands (cheapness, low working temperature, good durability and high efficiency), high selectivity toward hydrogen and minor one toward CO are essential to meet FC requirements. Besides this, the total price of the catalyst includes not only the price of precious metals in its composition, but also the price for production process of such catalysts. Increasing the numbers of sub-operation in production process generally leads to a higher cost of such catalyst. Among different methods for catalyst preparation magnetron sputtering has advantages such as simple setup, fast deposition procedure without any sub-operation compared to wet chemical methods. In this part of the thesis we will check SRM and POM reactions on deposited platinum and platinum-ceria thin film catalysts by using microreactor system.

4.2. Steam reforming of methanol (SRM)

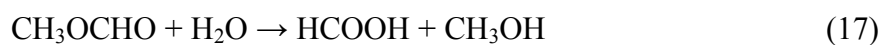
SRM reaction (13) is used for a conversion of methanol to hydrogen rich gas mostly for the fuel cell technology needs. It is a highly endothermic reaction ($\Delta H^\circ = 49.4 \text{ kJ}\cdot\text{mol}^{-1}$) which consumes methanol and water steam and produces hydrogen and carbon dioxide. In addition some undesirable CO presents as a by-product. There has been a debate in literature about the mechanism of SRM. Some authors [51,52] suggested that SRM in certain extent involves methanol decomposition (MD) (14) and water gas shift (WGS) (15) reactions:



In this case, hydrogen can be obtained not only from the reaction between methanol and water steam (13) but also via direct decomposition of methanol (14). Beside this, CO from MD can react with H_2O steam via WGS reaction (15) producing additional hydrogen and carbon dioxide.

Other researchers reported [53,54,55] that mechanism of SRM is a single step process, where H_2 and CO_2 are formed from methanol directly.

Another possible mechanism for SRM is via methanol dehydrogenation to methyl format with the further decomposition to hydrogen and carbon dioxide [56,57,58]. In such pathway, firstly, methanol dehydrogenates to the methyl format and hydrogen (16). Then methyl format reacts with water steam to produce formic acid and methanol (17) with following decomposition of formic acid to hydrogen and carbon dioxide (18).



4.2.1. SRM on Pt, PtO_x and Pt-CeO₂ thin film catalyst

In order to compare SRM activity on different thin film samples, we prepared Pt, PtO_x and Pt-CeO₂ (where relative Pt/Ce atomic concentration is 0.56) composite films by using magnetron sputtering technique. We selected Pt and PtO_x catalysts due to their good oxidation properties, which is already demonstrated by CO oxidation (see *subchapter 3.3*). Also SRM on Pt-CeO₂ thin film needs to be checked to figure out the influence of the ceria in platinum-ceria composite film on the activity. Therefore 10 nm thick Pt, PtO_x and Pt-CeO₂ layers have been deposited on flat SiO₂ substrate by means of RF-DC magnetron sputtering. Preparation procedure of Pt-CeO₂ as well as determining the platinum content in such film is well described in *subchapter 4.3.4*. The SiO₂ substrate was chosen because of its stability against methanol/water vapor, which presents in the gas feed mixture. SRM reaction was performed on the prepared samples using the microreactor setup for methanol oxidation experiment (*Fig. 7b*) with following modifications. Water and methanol steam were created by bubbling the helium buffer gas through the saturator field with solution of methanol and distilled water. The molar ratio of methanol to water was adjusted to stoichiometric 1:1 (CH₃OH:H₂O – 1:1) by changing parameters such as temperature and concentrations of methanol and water inside the saturator. Total flow rate of the feed mixture was 12 sccm. Since the temperature range of SRM is 250 - 300 °C (*Table 2*), thus, we selected low temperature reaction cell for the thin film samples (*Fig. 8*). Before entering the UHV chamber the product stream was passed through a laboratory cold trap immersed in Dewar flask filled with a freezing mixture (liquid nitrogen and ethanol, T = - 80 °C) in order to remove water and unreacted methanol. Then the products were sampled through a manual metering valve and monitored on-line by QMS.

QMS current signals of main products (H₂, CO, CO₂) were converted to the relative molecular concentrations using sensitivity factors obtained experimentally by calibrations with pure gases. All experiments were performed in the temperature range between 100 and 300 °C with the heating rate of 2 °C/min. In order to eliminate the condensing of the gas feed mixture inside the cell at the beginning of measurements, sample was preheated to 100 °C before the reaction mixture was introduced. After introducing the feed mixture on the sample, such constant

temperature was kept until concentrations of products reached steady condition. Only thereafter the temperature was ramped to 300 °C.

Morphology of the samples (as prepared and after SRM reaction) is presented in *Fig. 29*. As prepared Pt/SiO₂, PtO_x/SiO₂ and Pt-CeO₂/SiO₂ samples all demonstrated flat and continuous morphology (*Fig. 29a, b, c*).

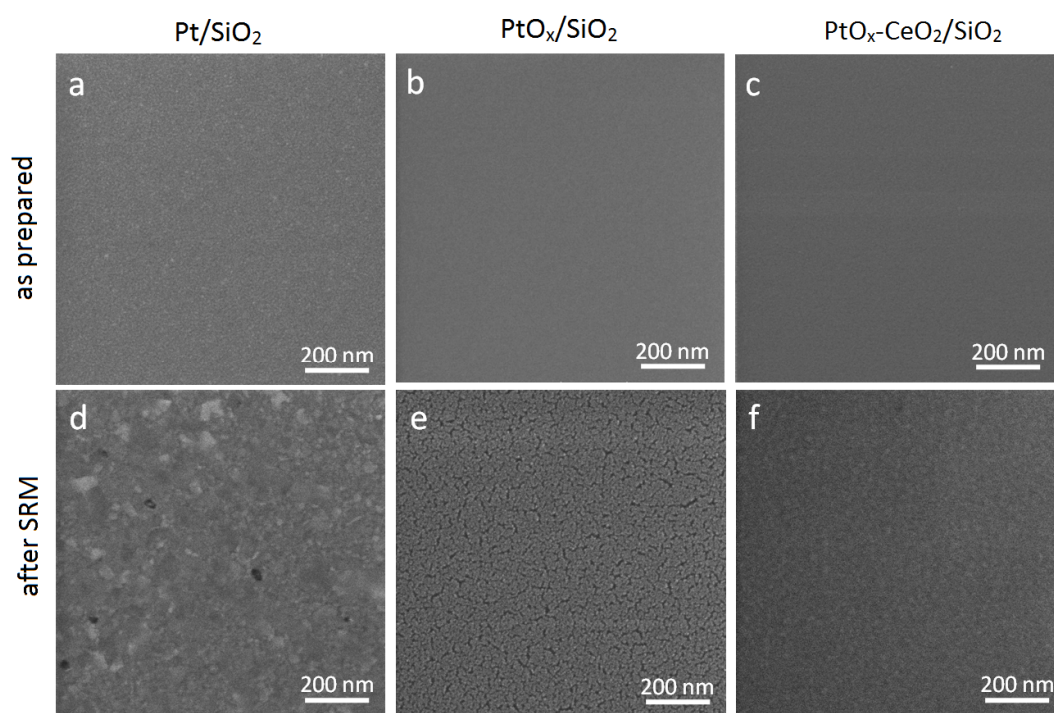


Fig. 29. SEM images of Pt, PtO_x and Pt-CeO₂ thin films deposited on SiO₂ substrates: Pt/SiO₂ as prepared (a) and after SRM reaction (d); PtO_x/SiO₂ as prepared (b) and after SRM (e); as prepared PtO_x-CeO₂/SiO₂ (c) and the same specimen after SRM (f).

After SRM reaction, morphology of Pt/SiO₂ specimen exhibited grains and patches (*Fig. 29d*) similar to the same sample after the CO oxidation reaction (*subchapter 3.3*). Platinum oxide thin film (PtO_x/SiO₂) after SRM reaction demonstrated extensive cracking of the surface with uncovered SiO₂ substrate, while the surface of Pt-CeO₂/SiO₂ specimen (after SRM) has barely visible grains sized up to 20 nm in diameter (*Fig. 29e, f*).

Fig. 30 presents the catalytic activity of Pt/SiO₂ sample, where relative concentrations of H₂, CO, and CO₂ were plotted against temperature. Since a very noisy H₂ QMS signal was obtained, we applied the adjacent averaging to the hydrogen concentration curve (black line on the graph). From the plot it can be seen that H₂ onset was detected around 250 °C, while CO started to produce approximately

at 180 °C. Hydrogen concentration was detected two times higher than CO at 300 °C. Only small amount of CO₂ (5-6 % from H₂ yield) at highest reaction temperatures was observed.

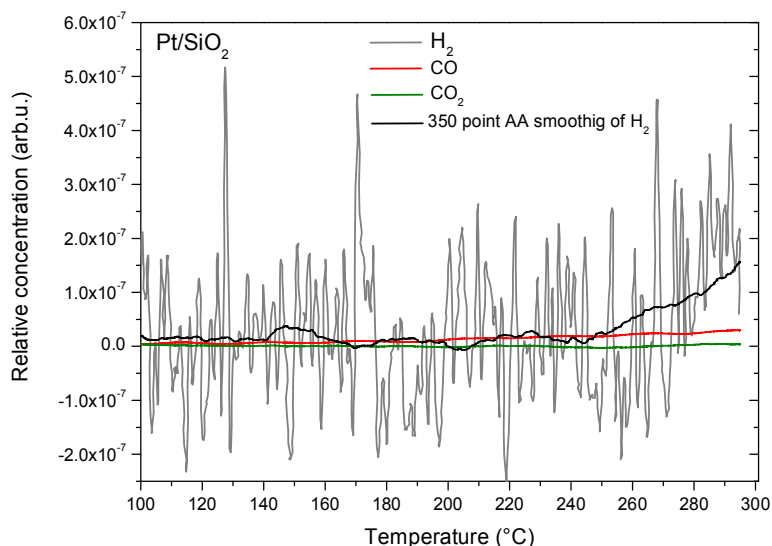


Fig. 30. SRM activity of 10 nm Pt/SiO₂ sample: relative concentrations of H₂, CO and CO₂ versus temperature. Black line represents AA smoothing of H₂ concentration curve.

SRM activity of PtO_x/SiO₂ sample is presented in Fig. 31. Hydrogen onset was observed approximately at 180 - 190 °C. Relatively low CO and CO₂ yields (around 10 times lower) compared to hydrogen one was detected at 300 °C.

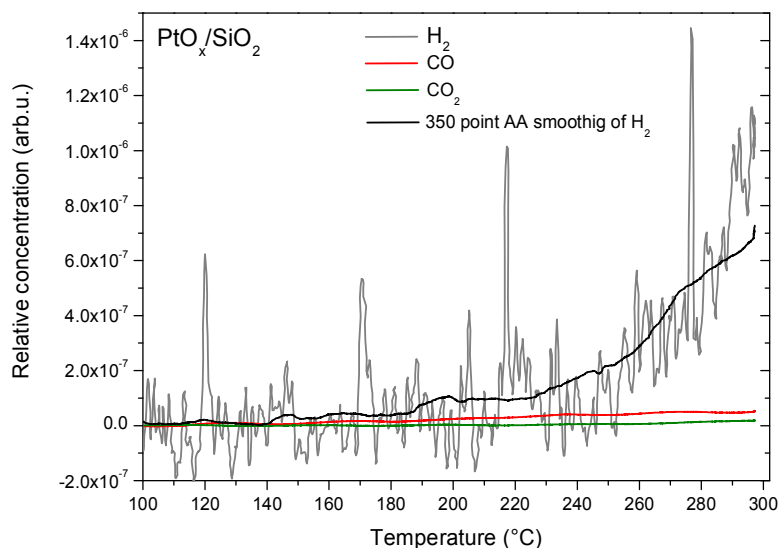


Fig. 31. SRM activity of 10 nm PtO_x/SiO₂ sample: relative concentrations of H₂, CO and CO₂ versus temperature. Black line represents AA smoothing of H₂ curve.

Fig. 32 shows the catalytic activity of Pt-CeO₂/SiO₂ sample. Here, weak overall activity was observed in the whole temperature range. The products of the reaction (H₂, CO and CO₂) were detected in insignificant concentrations compared to other samples.

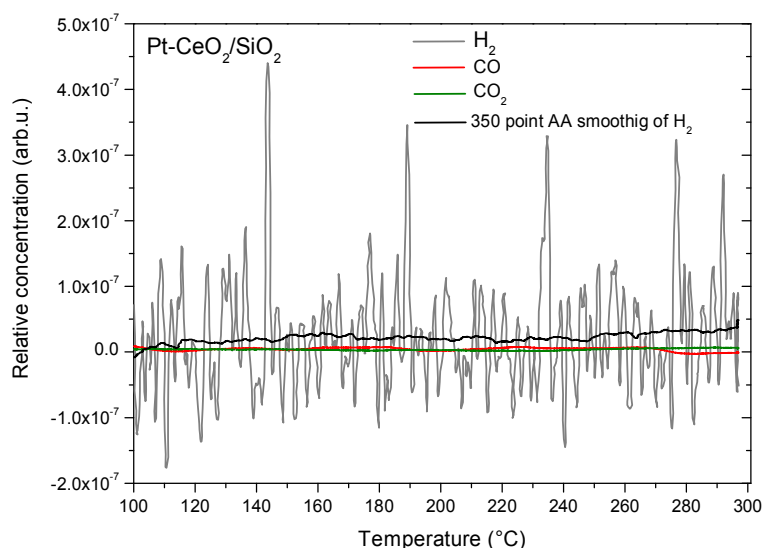


Fig. 32. SRM activity of 10 nm Pt-CeO₂/SiO₂ sample: relative concentrations of H₂, CO and CO₂ versus temperature. Black line represents AA smoothing of H₂ curve.

Since the most important product of SRM reaction is hydrogen, we plotted H₂ yields (AA smooth curves) of the analyzed samples against temperature in Fig. 33. The relative concentration of hydrogen obtained from PtO_x/SiO₂ sample was four times higher than Pt/SiO₂ at the highest reaction temperature (300 °C), while Pt-CeO₂/SiO₂ sample exhibited negligible H₂ yield.

The most common SRM pathway involves MD and WGS reaction (reactions 13 - 15). In case of SRM on deposited Pt/SiO₂ sample, we observed higher CO yield than CO₂ at 300 °C (Fig. 30). This indicates that MD process (which yields H₂ and CO) prevails over WGS (which yields CO₂ and H₂) on a deposited metallic platinum surface. Generally, precious metals exhibit weak WGS activities, due to weak oxidation of H₂O on them [59]. We supposed that WGS is inhibited on our Pt layer, hence, a low concentration of CO₂ was observed. Regarding Pt-CeO₂/SiO₂ sample (Fig. 32), low activity was detected in whole temperature range. It seems like MD reaction, as an initial part of SRM, almost does not take place on Pt-CeO₂/SiO₂ sample. Generally methanol is decomposed to water and formaldehyde (CH₂O) on ceria layer [60].

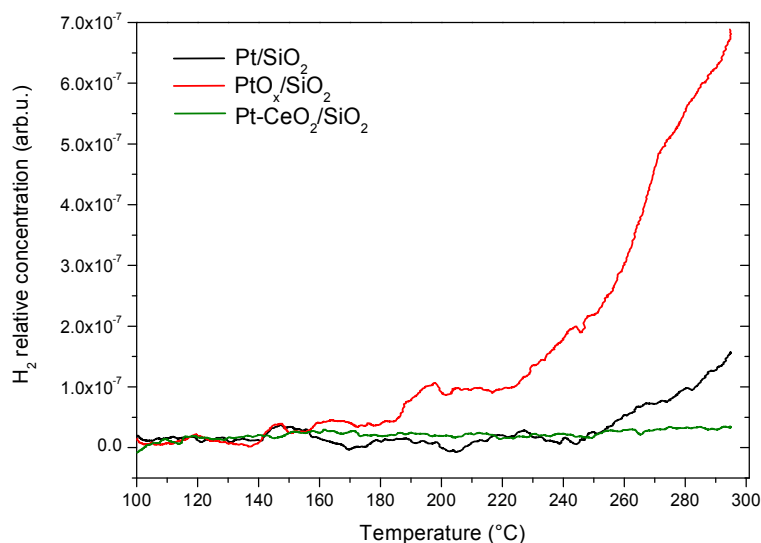


Fig. 33. Hydrogen yields comparison (AA smooth curves) of 10 nm thick Pt, PtO_x and Pt-CeO₂ catalysts deposited on SiO₂ substrate.

In case of Pt-CeO₂/SiO₂ sample, some ceria is also present on the surface (because the relative Pt/Ce atomic concentration is 0.56). Thus, we can expect the same products of MD as on ceria (H₂O and CH₂O). As a result, H₂ and CO were formed in low concentrations because of the presence of active platinum in Pt-CeO₂ composite film. Moreover, low CO yield leads to weak WGS reaction (since no CO molecules to react with H₂O), which is followed by MD at higher temperatures. In addition, active platinum can be encapsulated by ceria (or diffused from the surface to the bulk) during the heating up procedure, resulted in catalytic decline and low durability (well described in *subchapters 4.3.4 - 4.3.5*).

Regarding PtO_x/SiO₂ sample (*Fig. 31*), it contains lattice oxygen, which can be easily removed from thin film during the reaction - i.e. reduction process (previously explained in *subchapter 3.3, also see subchapter 4.3.1*). As a result, PtO_x reduces to metallic Pt which leads to the increasing of the surface area of the thin film (*Fig. 29e*). Higher surface area of the catalysts has more active sites where molecules of CH₃OH and H₂O can adsorb and react. Thus, PtO_x/SiO₂ sample exhibited four times higher hydrogen yield compared to Pt/SiO₂, while the concentrations of CO and CO₂ were lower due to the presence of lattice oxygen in PtO_x.

In this chapter, the SRM reaction on Pt/SiO₂, PtO_x/SiO₂ and Pt-CeO₂/SiO₂ samples were compared using the laboratory microreactor system. Low SRM activity exhibited Pt-CeO₂/SiO₂ sample due to weak MD process (as an initial part of SRM)

on ceria. Regarding the Pt/SiO₂ specimen, SRM reaction takes place on such sample via MD + WGS mechanism, with preference of the MD due to generally bad WGS reaction on platinum. PtO_x/SiO₂ specimen exhibits clear advantages compared to metallic platinum layer with the same thickness. We assumed that during SRM reaction platinum oxide reduces to metallic Pt, which leads to an increasing of the surface area of such film compared to metallic Pt. Thus, PtO_x/SiO₂ sample outperformed Pt/SiO₂ one in regards of the hydrogen yield.

4.3. Partial oxidation of methanol (POM)

Probably the most rational way of obtaining hydrogen from methanol for the fuel cell applications is via POM (19). POM is a heterogeneously catalyzed reaction, where methanol steam and oxygen react on the surface of the catalyst with a further producing of hydrogen and carbon dioxide:



POM reaction is exothermic ($\Delta H^\circ = -192.2 \text{ kJ}\cdot\text{mol}^{-1}$), has a high reaction rate and allows to use even air instead of oxygen compared to SRM and MD. Presence of carbon monoxide in the product stream is only one drawback of POM reaction (as well as for SRM and MD).

Mechanism of POM reaction depends on the used catalysts and selected methanol to oxygen molar ratios in gas feed mixture [61,62,63]. Generally POM includes 4 main reactions: methanol combustion (20, 21), SRM (22), MD (23) and WGS reactions (24).



POM mechanism has been proposed as two - step process: methanol combustion reaction (at low reaction temperature) followed by SRM (at higher temperature). Methanol combustion reactions (20, 21) produce water, carbon dioxide and carbon monoxide. Further water together with the methanol steam acts in the SRM reaction (22). Also MD (23) can occur independently during the POM reaction. In addition carbon monoxide, as one of the product of methanol decomposition, can react also with water (produced from methanol combustion) via WGS reaction (24).

Therefore, mechanism of the POM reaction is quite complex and includes a combination of the aforementioned reactions.

4.3.1. POM on PtO_x and Pt thin film catalysts

In previous experiment (*subchapter 4.2.1*) oxidized and metallic platinum thin films were used to convert methanol via SRM reaction. In order to study POM reaction on thin film samples, at first, we selected the same catalytically active material. Therefore the catalyst thin films (PtO_x, Pt) with an average thickness of 10 nm were prepared by means of DC magnetron sputtering. Deposition was carried out at room temperature using a 2” - diameter platinum target and DC magnetron power of 10 W. We used flat SiO₂ wafer as a substrate. The choice of the working gas (argon or oxygen) determined the growth of either metallic platinum or platinum oxide. With constant gas pressure in magnetron chamber at 4×10^{-1} Pa, the deposition rate was approximately 3 nm/min for metallic platinum and 2 nm/min for platinum oxide layers.

Methanol oxidation reaction was performed over prepared catalysts with identical conditions for each experiment using the microreactor setup illustrated in *Fig. 7b* and the sample holder for low temperature operations (*Fig. 8*). Total flow rate of the gas feed mixture was 12 sccm. Ratio of methanol to oxygen was adjusted to stoichiometric 2:1 (CH₃OH:O₂ – 2:1) by changing parameters such as the temperature of saturator and the flow rates of helium and oxygen. TPR1 and TPR2 runs have been done in 100 - 320 °C temperature region with heating rate of 2 °C/min. Other experimental conditions were the same as for SRM measurements.

The catalytic activity of PtO_x/SiO₂ sample is presented in *Fig. 34*, where TPR1 and TPR2 are compared. Hydrogen onset of TPR1 was detected around 150 - 155 °C while some CO and CO₂ was already registered at the initial reaction temperature (100 °C). In the whole reactive temperature range the ratio of CO₂ to hydrogen in the reacted gas mixture remains higher than the theoretical stoichiometry of partial oxidation of the methanol (i.e., 2:1 according to reaction (19)). This observation, along with the detection of CO (about 50% compared to CO₂ in the whole temperature range), suggests that the methanol oxidation proceeds through the more alternative reaction channels.

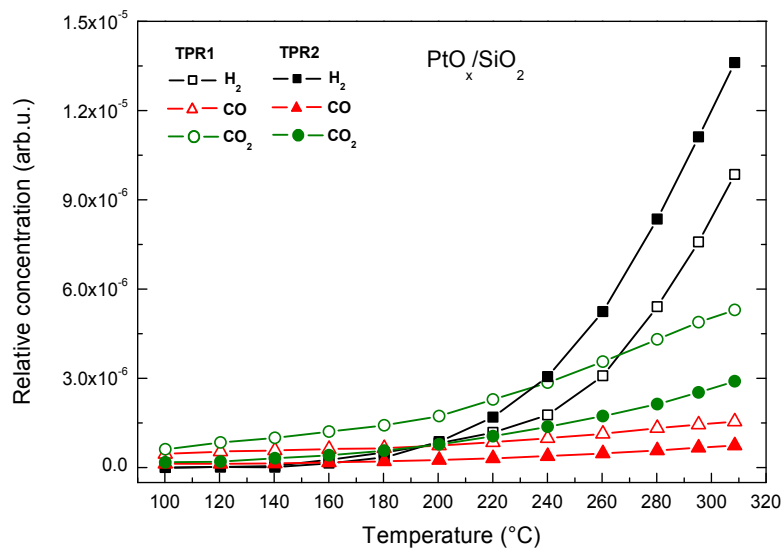


Fig. 34. Comparison of the methanol oxidation activities of TPR1 and TPR2 on 10 nm thick $\text{PtO}_x/\text{SiO}_2$ sample: relative concentrations of H_2 , CO and CO_2 plotted versus temperature (TPR1 - open symbols, TPR2 - solid symbols).

After cooling back to 100 °C the sample was subjected to another identical TPR cycle. While the hydrogen yield increased only slightly (25%) compared to the TPR1, the production of CO and CO_2 dropped drastically, keeping the same mutual ratio of about 1:2. In the end of the second cycle (320 °C), the calculated relative concentrations of H and C in the detected products matched the 4:1 stoichiometry of methanol molecule, i.e., all hydrogen is released in the form of H_2 .

The occurrence of CO and CO_2 in the products mixture at initial temperature (100 °C) indicates that the reaction route splits between 2 methanol combustion reactions (20, 21). Another combustion product is water, but we could not measure the water concentration directly due to its freezing in the cold trap. At 150 °C SRM reaction starts, consuming water and methanol, and yielding H_2 and additional CO_2 (22). Above 260 °C we observed considerable increasing of CO concentration, which indicates starting the MD reaction (23).

Fig. 35 shows a comparison of hydrogen production curves during three consecutive TPR cycles on $\text{PtO}_x/\text{SiO}_2$ specimen. The catalytic properties of the PtO_x sample seems to be stabilized between TPR1 and TPR2 cycle - further repeating the methanol oxidation procedure exhibits the same reaction selectivity with only a minor (9%) increase of absolute yields in the third cycle.

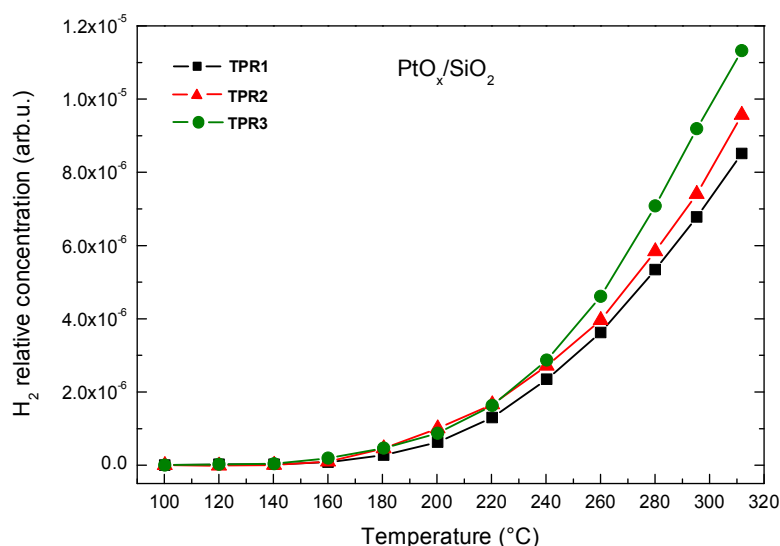


Fig. 35. Comparison of the hydrogen yield for three consecutive TPR cycles on 10 nm PtO_x/Si sample.

The physical structure and chemical composition of the sample was examined by SEM and XPS respectively. Such investigations have been done at three stages of the TPR run: before reaction (as prepared sample); at the point when it just starts to generate hydrogen (150 °C) and at the end of the TPR1 (320 °C). SEM image of the as prepared PtO_x layer exhibits flat and continuous morphology (Fig. 36a).

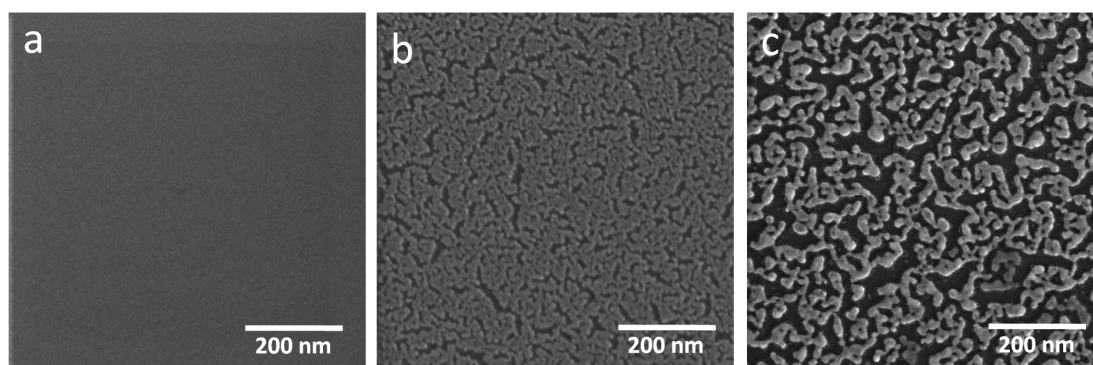


Fig. 36. SEM images of 10 nm PtO_x layer deposited on Si substrate as prepared (a), after heating up to 150 °C in reaction mixture (b), and after complete TPR cycle (heating up to 320 °C).

Pt 4f XPS spectrum of the same surface (Fig. 37a) reveals that platinum is present mainly in Pt⁴⁺ cationic state with the rest (approx. 4%) in the form of Pt²⁺. The catalyst was then inserted into the reaction cell, pre-heated to 100 °C and exposed to the reaction mixture. Upon hydrogen detection in the product stream

(150 °C) the heating was interrupted and the sample was transferred into the XPS analysis chamber. Pt 4f XPS spectra (*Fig. 37a*) of such treated sample shows that the quadruply charged platinum cations were reduced to metallic state ($\text{Pt}^{4+} \rightarrow \text{Pt}^0$) while the amount of doubly charged platinum remained unaffected. O 1s spectrum (*Fig. 37b*) of the as prepared sample exhibits an oxygen peak at BE which corresponds to polycrystalline PtO_2 (531.1 eV) and PtO (531.7 eV) phases [64,65], along with the SiO_2 peak (532.6 eV) which originates from the underlying natural oxide layer formed on SiO_2 surface.

After TPR to 150 °C the Pt oxide components practically disappear from the spectrum except for a small residuum of PtO , while SiO_2 -related peak dominates the spectrum.

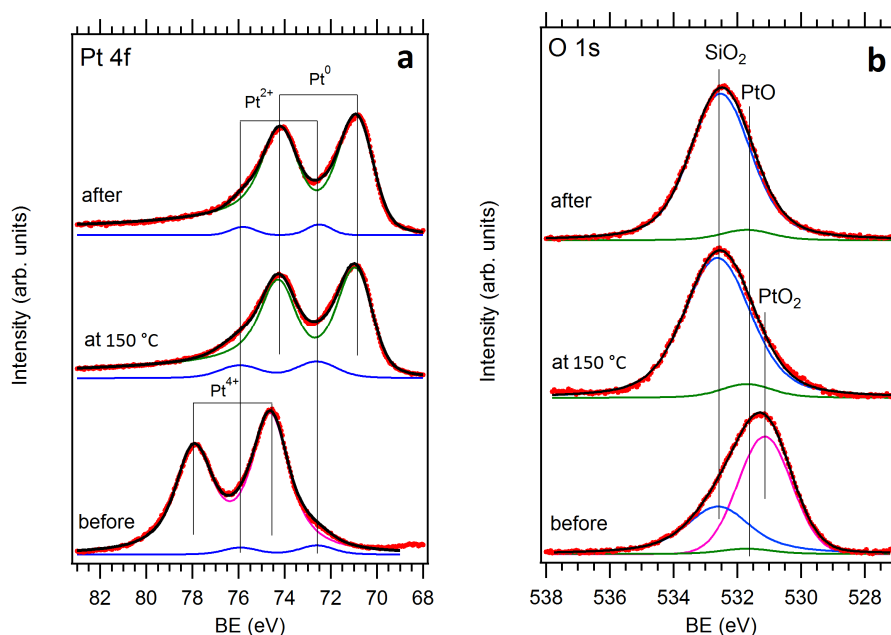


Fig. 37. Pt 4f (a) and O 1s (b) spectra of 10 nm PtO_x/Si sample before reaction, after methanol oxidation reaction to 150 °C, and after complete reaction cycle to 320 °C.

SEM image (*Fig. 36b*) exhibits intensive cracking of the platinum oxide thin film, leading to increased surface area of the deposit along with the exposure of the underlying silicon substrate. The sintering of the thin film progresses as the TPR is continued as can be seen in the SEM image after the complete reaction cycle to 320 °C (*Fig. 36c*). The chemical composition of the sample (*Fig. 37b*), however, did not exhibit any further noticeable changes above 150 °C.

The fact that the conditioned PtO_x catalyst consists mainly of the metallic platinum suggests a direct comparison with pure platinum. We sputter-deposited a Pt layer with the same thickness (10 nm) on a SiO_2 wafer and subjected it to an identical

TPR procedure as above. *Fig. 38* shows the hydrogen yield comparison of 10 nm metallic platinum and platinum oxide. The main reaction products over platinum catalyst are also H₂, CO, and CO₂ (CO and CO₂ curves not shown here) but their overall absolute reaction efficiency is noticeably lower. The poor performance of pure platinum for POM presumably results from the strong binding of CO to the metal which inhibits adsorption of both oxygen and methanol [66,67,68].

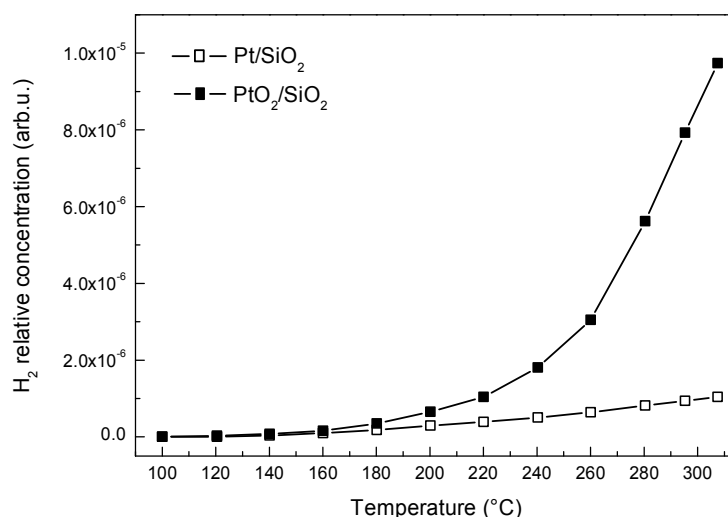


Fig. 38. Hydrogen yields comparison of Pt/SiO₂ and PtO_x/SiO₂ samples.

The SEM image of the as prepared Pt thin film (*Fig. 39a*) exhibits nearly the same flat and continuous morphology as the PtO_x layer with only a minor granularity on the scale of few nanometers. After the reaction (*Fig. 39b*), on contrary to PtO_x, no visible cracks appear within the layer, however, a sintering effect is apparent forming larger grains and patches sized tens to hundreds nanometers in diameter.

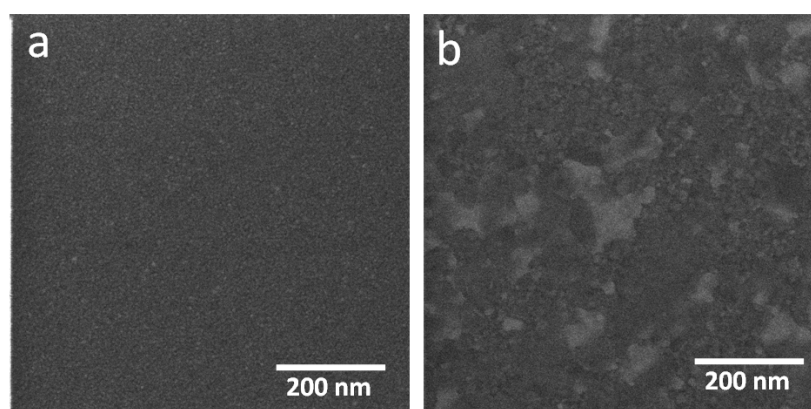


Fig. 39. SEM images of 10 nm Pt layer deposited on Si substrate before (a) and after methanol oxidation TPR to 320 °C (b).

Pt 4f XPS spectra of the 10 nm Pt/Si sample (*Fig. 40a*) demonstrates that the metallic (Pt^0) character of the surface remained unchanged after the reaction cycle, while in O 1s region (*Fig. 40b*) the oxygen peak related to SiO_2 substrate (532.6 eV) gained its intensity nearly 10-fold.

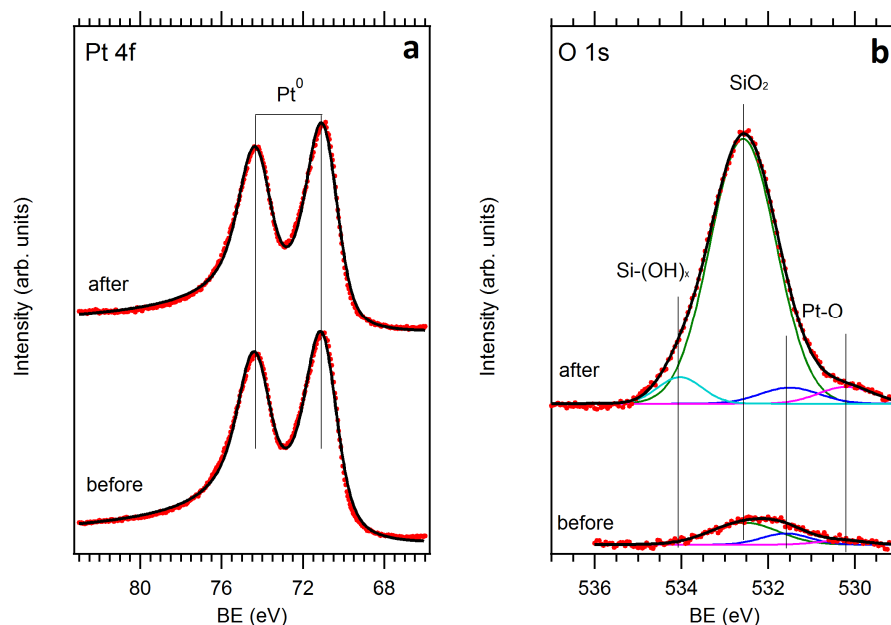


Fig. 40. Pt 4f (a) and O 1s (b) spectra of 10 nm Pt/Si sample before and after methanol oxidation TPR to 320 °C.

It is known that Pt on Si tends to form silicide's at their interface, at elevated temperatures potentially exposing Si atoms at the surface susceptible to oxidation. Nevertheless, even at temperatures as high as 550 °C metallic platinum remains as the dominant surface phase [69]. The minor components at lower BEs in O 1s spectra (530.3 eV, 531.4 eV) can be attributed to a silica-bound oxygen interacting with Pt [70] or, for the latter one, hydroxylated Si ($\text{Si}(\text{OH})_x$) [71]. The peak which appeared at 534.0 eV after the reaction most likely belongs to an oxygen covalently bound to adsorbed carbon and/or hydrocarbon residua.

According to the chemical and morphological analysis of Pt/SiO_2 and $\text{PtO}_x/\text{SiO}_2$ samples in their stabilized form (i.e. after the completed TPR), two obvious differences can be seen: sample roughness and presence of Pt^{2+} . We supposed that the higher overall activity of the PtO_x catalyst is primarily due to its enhanced surface area compared to the relatively flat Pt, while the presence of the residual Pt^{2+} is responsible for the altered chemistry of the PtO_x catalyst.

4.3.2. POM on PtO_x deposited on carbonaceous interlayers

In previous experiments we demonstrated superior POM activity of the oxidized platinum compared to the metallic one. In an attempt to obtain even higher reaction rates of PtO_x we prepared another catalyst by using the same magnetron sputtering technique in order to deposit platinum oxide onto different types of high surface area carbonaceous layers [72]. These layers were grown on flat SiO₂ (100) substrate by means of commercial modular high vacuum coating system MED020 (BALTEC). The choice of working gas (argon or nitrogen) determined the growth of either amorphous carbon (a-C) or nitrogenated amorphous carbon (CN_x) films. In addition, oxygen plasma treating procedure during 40 minutes on other a-C layer was done.

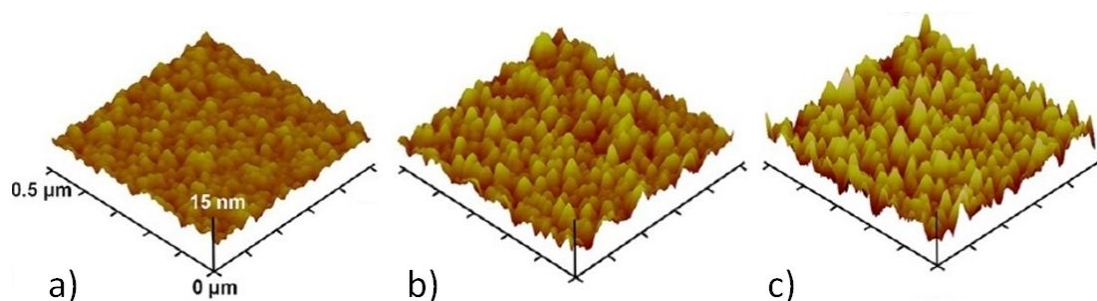


Fig. 41. AFM micrographs of carbonaceous layers deposited on silicon substrates: a-C layer (a), CN_x (b) and oxygen treated a-C_t (c) layers [72].

Accordingly, a-C, CN_x and oxygen treated a-C layers (labeled a-C_t) were prepared. Atomic force microscopy (AFM) micrographs demonstrated considerable low porosity of freshly prepared a-C layer (*Fig. 41a*) compared to the same sample after the oxygen treating procedure (*Fig. 41c*). The CN_x layer (*Fig. 41b*) exhibited porosity level close to the a-C_t specimen.

Then, we deposited 10 nm thick PtO_x thin films on aforementioned carbonaceous layers by using DC magnetron sputtering. Morphology of as prepared specimens and after TPR1 stage was observed using SEM technique (*Fig. 42*). As prepared PtO_x/a-C_t/SiO₂ sample demonstrated granular morphology with approx. 10 nm grains in size, while after TPR1 stage an extensive cracking of the surface with an uncovered carbon interlayer was observed. Also it seems like PtO_x reduced and conglomerated in small islands (*Fig. 42a, d*). As prepared PtO_x/a-C/SiO₂ sample exhibited rough morphology with slightly visible grains, while after POM reaction we

observed coalescence of PtO_x in islands (up to 100 nm) and uncovering the carbon interlayer (*Fig. 42b, e*).

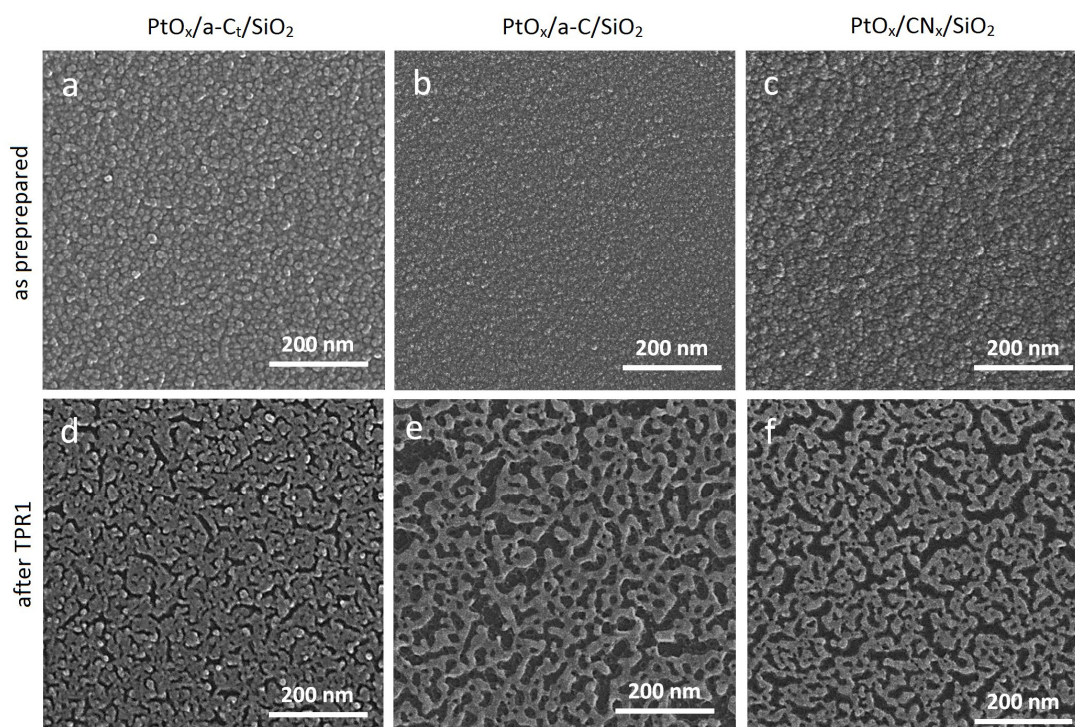


Fig. 42. SEM images of 10 nm PtO_x deposited on carbonaceous layers: $\text{PtO}_x/\text{a-C}_t/\text{SiO}_2$ as prepared (a) and after POM TPR1 (d); $\text{PtO}_x/\text{a-C}/\text{SiO}_2$ as prepared (b) and after POM TPR1 (e); $\text{PtO}_x/\text{CN}_x/\text{SiO}_2$ as prepared (c) and after POM TPR1 (f).

Regarding freshly deposited $\text{PtO}_x/\text{CN}_x/\text{SiO}_2$ sample it exhibited granular structure which has decreased size of grains (up to 5 nm) compared to $\text{PtO}_x/\text{a-C}_t/\text{SiO}_2$ specimen at same conditions (*Fig. 42c*). After POM TPR1 such sample exhibited Pt islands (about 20 nm) surrounded by carbon from interlayer (*Fig. 42b*).

POM reaction was performed on these samples on microreactor under identical conditions as in previous POM experiments. *Fig. 43a* demonstrates POM activity of $\text{PtO}_x/\text{a-C}/\text{SiO}_2$ sample. At the highest reaction temperature (320 °C) the ratio of hydrogen to CO_2 remains lower than the stoichiometry of POM (2:1) according to reaction 19. Concentration of undesirable CO reached $\frac{1}{4}$ from that of hydrogen. The $\text{PtO}_x/\text{CN}_x/\text{SiO}_2$ specimen exhibited worse products selectivity than the previous sample (*Fig. 43b*). In this case 15% higher CO_2 yield and 80% lower hydrogen one was observed, while CO yield in whole temperature range remains the same as for $\text{PtO}_x/\text{a-C}/\text{SiO}_2$.

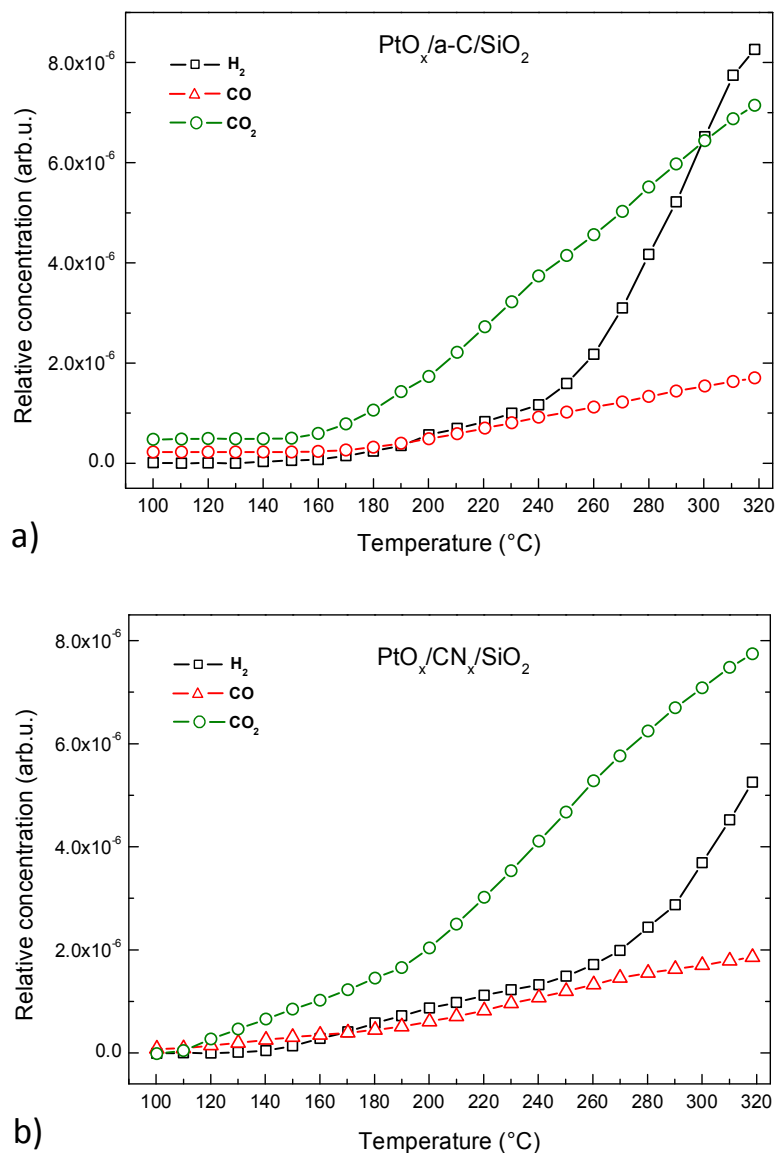


Fig. 43. Catalytic activity of 10 nm PtO_x deposited on a-C (a) and CN_x (b) interlayers: Relative concentrations of H₂, CO, and CO₂ products plotted versus temperature.

Fig. 44a represented POM activity of PtO_x/a-C_t/SiO₂ sample. During the reaction (TPR1), the ratio of hydrogen to CO₂ remains lower (approx. 30 % from the ideal POM ratio 2:1) than aforementioned stoichiometry of POM. The behavior of CO concentration curve was similar to PtO_x/a-C/SiO₂ and PtO_x/CN_x/SiO₂ samples. Since PtO_x/a-C_t/SiO₂ specimen exhibited the highest activity as well as the most advantageous ratios of products (highest H₂ and lowest CO and CO₂ yields), we decided to perform TPR2 run to check the stability of the sample. TPR2 showed similar hydrogen concentration curve as at TPR1, but about two-fold decrease the concentrations of both CO and CO₂ (Fig. 44a, solid symbols).

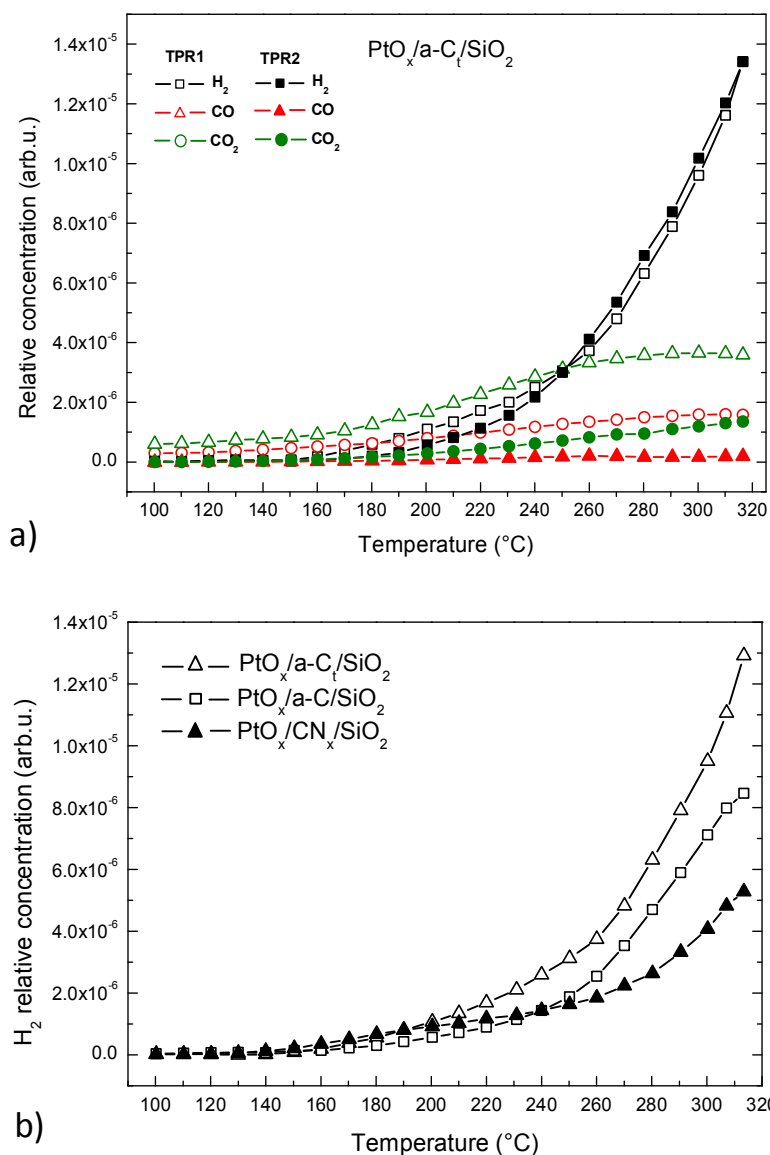


Fig. 44. Catalytic activity (TPR1 and TPR2) of 10 nm PtO_x deposited on a- C_t interlayer (a); hydrogen yields comparison of 10 nm thick PtO_x catalysts deposited on a- C_t , a-C and CN_x interlayers (b).

In general, the analyzed samples exhibited similar behavior of hydrogen production curves only differing in maximum values at 320 °C (Fig. 44b). Here, relative hydrogen concentration of $\text{PtO}_x/\text{a-C}_t/\text{SiO}_2$ sample is up to 20% and 40% higher than $\text{PtO}_x/\text{a-C}/\text{SiO}_2$ and $\text{PtO}_x/\text{CN}_x/\text{SiO}_2$ samples respectively.

Since the chemical composition of the samples supposed to be the same (platinum oxide on carbon) only the morphology slightly differs, thus, we performed the XPS analysis (before and after TPR2 stage) only on specimen with the highest activity - i.e. $\text{PtO}_x/\text{a-C}_t/\text{SiO}_2$ sample. Pt 4f XPS spectra before the reaction exhibits a presence of $\text{Pt}^{4+/2+}$ species (Fig. 45a). After the TPR2 stage we observe the reduction

of platinum oxide to the metallic platinum ($\text{Pt}^{4+} \rightarrow \text{Pt}^0$) while the Pt^{2+} species have been preserved. Similar consistent behavior is seen in the O 1s XPS region (Fig. 45b) where the SiO_2 peak dominates the spectrum over PtO_x after the reaction due to the reduction and the PtO_x thin film disintegration. The surface cracking during TPR also uncovers the a-C interlayer represented by the two-fold increase of all components of C 1s photoelectron spectra (Fig. 45c) where the main carbon peak at 284.6 eV is accompanied by other two contributions at 286.3 eV and 288.0 eV characteristic of C–O and C=O bonds, respectively, originating from oxygen plasma treatment of the carbon layer.

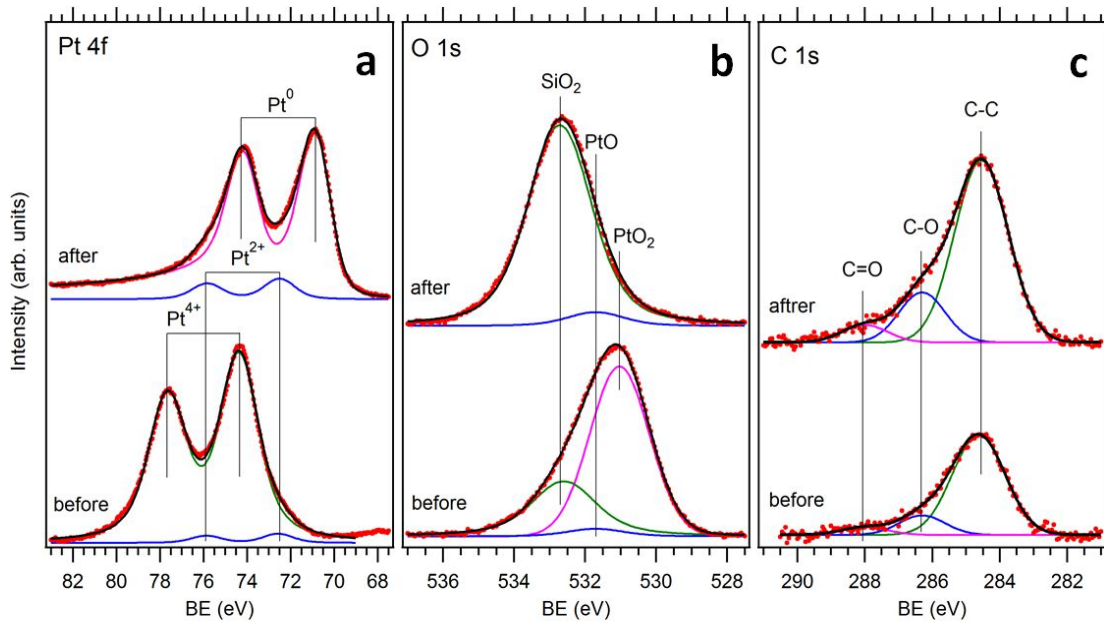


Fig. 45. Pt 4f (a); O 1s (b) and C 1s (c) spectra of 10 nm Pt/a-C/SiO₂ sample before and after the POM reaction.

As we stated before (*subchapter 4.3*), the POM reaction starts with a methanol combustion at initial temperatures, realizing H₂O, CO and CO₂. This explained the elevated concentration of CO and CO₂ on all analyzed samples at 100 °C (Fig. 43, 44a). Also, platinum oxide layer is reduced to metallic platinum ($\text{Pt}^{4+} \rightarrow \text{Pt}^0$) at low temperatures, which is accompanied with the increasing of the surface area. After the temperature reached 150 °C, SRM starts, producing hydrogen and CO₂ ($\text{CH}_3\text{OH} + \text{H}_2\text{O} \rightarrow 3\text{H}_2 + \text{CO}_2$). Above 260 °C, MD takes place yielding additional hydrogen and CO. Hydrogen production onsets are the same for each analyzed sample (150 °C), thereby SRM reaction starts from such temperatures. $\text{PtO}_x/\text{a-C}/\text{SiO}_2$ and $\text{PtO}_x/\text{CN}_x/\text{SiO}_2$ samples demonstrated visible changing the slope of hydrogen

concentration curves at 250 °C, which indicates the switching from SRM to MD reactions (*Fig. 43*). In contrary, the PtO_x/a-C_t/SiO₂ sample (*Fig. 44a*) demonstrated a smooth switching between SRM and MD - i.e. no drastically changing in the slope of H₂ concentration curves.

Initially, a-C_t interlayer exhibited the highest porosity of the surface among other carbonaceous layers (*Fig. 41c*). Thus, after deposition of platinum oxide on it, we obtained a sample with the highest surface area (*Fig. 42a*). The activity data proved, that the PtO_x/a-C_t/SiO₂ specimen produces not only more hydrogen (due to higher surface area), but also less CO₂ compared to other samples (while CO yield was similar to other specimens). Lower CO₂ yield of such sample (PtO_x/a-C_t/SiO₂) can be explained by slower reduction process of oxidized Pt, i.e. - somehow 10 nm thick PtO_x with higher surface area reduces slowly compared to the same catalysts with lower surface area (PtO_x/CN_x/SiO₂, PtO_x/a-C/SiO₂). As a result, low reduction rate of the platinum oxide leads to a low CO₂ yield in whole temperature range. By the way, TPR2 performed on PtO_x/a-C_t/SiO₂ sample (*Fig. 44a*) demonstrated two-fold decrease of CO and CO₂ yields, while hydrogen yield remained the same. This can be explained by the absence of the oxygen in thin film (platinum is already reduced) which promoted CO oxidation process at TPR1 (see *subchapter 3.3*) Moreover uncovered carbon interlayer after POM reaction (analyzed by XPS and SEM) cannot provide the methanol combustion at lower temperatures, since the methanol does not adsorb dissociatively on non-activated carbon under our experimental conditions [73,74]. Thus, the main sources of CO and CO₂ during TPR2 are SRM and MD reactions.

Carbonaceous materials used as interlayer is a good option to improve the efficiency of thin films. Grown on silicone substrate, such interlayer greatly increased the surface area of the thin film catalyst deposited on it. In this work we deposited 10 nm thick PtO_x layer on several types of carbon interlayers with a further testing of POM activity. Due to higher surface area, PtO_x/a-C_t/SiO₂ sample generally demonstrated better efficiency and selectivity of products (higher H₂ and lower CO and CO₂ yields) compared to other prepared specimens.

4.3.3. POM on PtO_x under different methanol to oxygen molar ratios

POM reactivity does not depend only on the analyzed catalyst, but also on the molar ratios of the reactants (CH₃OH and O₂) in the gas feed mixture [75,61 - 63]. So, it is important to study how oxygen content in the feed mixture affects the POM activity and selectivity. Therefore we prepared several PtO_x/SiO₂ samples (preparation conditions were same as in *subchapter 4.3.1*) and performed POM experiments under different methanol to oxygen (CH₃OH:O₂) molar ratios using the laboratory micro-reactor system. Desirable CH₃OH:O₂ molar ratios (1:1; 2:1 and 3:1) were adjusted by changing the flow rates of helium and oxygen. Also methanol decomposition MD (without O₂) and time-on-stream tests were done in order to check the behavior of MD and long-term stability on PtO_x. Two consecutive temperature programmed reactions (TPR1, TPR2) were done for each sample at conditions used in previous experiments, except the time-on-stream test.

We already checked POM activity on 10 nm thick PtO_x layer under the stoichiometric molar ratio of reactants (CH₃OH:O₂ – 2:1) and described the results in *subchapter 4.3.1*. But, before present experiment, the QMS was damaged, so we replaced it by the newest model (QMG 220, Prisma PlusTM) which is supposed to have better sensitivity than the previous one. In order to provide reliable comparison of POM reactions, we performed POM under stoichiometric molar ratio on PtO_x again. Comparison of POM activity of TPR1 and TPR2 is presented in *Fig. 46*.

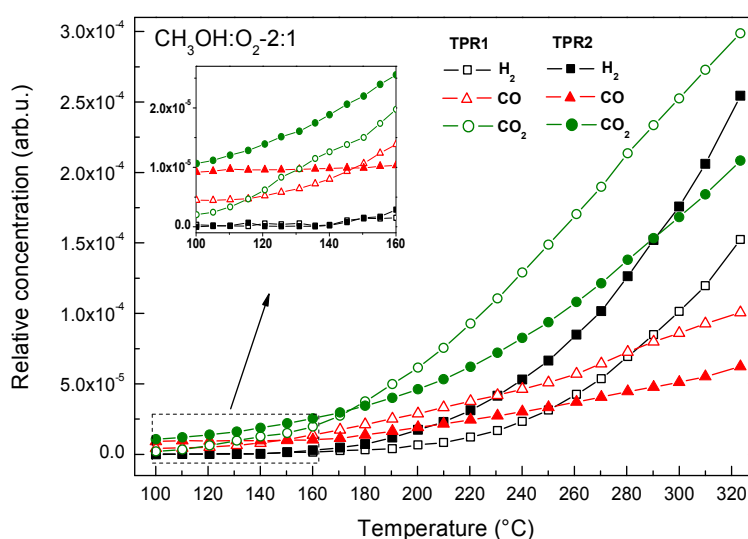


Fig. 46. Methanol oxidation activity of 10 nm PtO_x/SiO₂ sample at CH₃OH:O₂ – 2:1 molar ratio: relative concentrations of H₂, CO and CO₂ plotted versus temperature (TPR1 - open symbols, TPR2 - solid symbols); inset - zoomed part of the same graph in 100 - 160 °C.

Presents of CO and CO₂ in beginning of the reaction (100 °C) during both TPR1 and TPR2 indicates that the methanol combustion reactions ($\text{CH}_3\text{OH} + 3/2 \text{O}_2 \rightarrow 2\text{H}_2\text{O} + \text{CO}_2$; $\text{CH}_3\text{OH} + \text{O}_2 \rightarrow 2\text{H}_2\text{O} + \text{CO}$) take place at low temperature. The CO₂ concentration curve of the TPR1 exhibited poorly defined peak (see inset of *Fig. 46*) between 100 and 150 °C. Around 150 °C SRM reaction starts, which consumes methanol and water (product of methanol combustion) and yields hydrogen and CO₂. At higher temperatures (over 230 °C) a methanol decomposition (MD) occurs, which yields additional H₂ and CO. The XPS and SEM analysis of equal PtO_x/SiO₂ sample under the same POM reaction procedure has been reported in *subchapter 4.3.1*. The XPS observation showed that during TPR1 platinum oxide is already reduced at 150 °C ($\text{Pt}^{4+} \rightarrow \text{Pt}^0$). Therefore majority of lattice oxygen has been removed from the catalyst, which is accompanied with a surface roughening demonstrated by SEM (*Fig. 36*). From XPS and SEM analysis obtained on PtO_x during previous experiments we can assume that the aforementioned CO₂ “hump” between 110 and 150 °C at TPR1 on our sample (*Fig. 46*, inset) is the result of the CO oxidation process. In this case molecules of CO (as one of the products of methanol combustion) strike lattice oxygen of PtO_x and desorb from the surface in form of CO₂ (similar as in case with CO oxidation on PtO_x in *subchapter 3.3*). Interestingly, that we did not observe such elevate CO₂ production when operated with older model of QMS (*Fig. 34*). During TPR2 run the CO₂ peak disappeared in 100 - 150 °C region (*Fig. 46*, inset). It is due to the absent of the lattice oxygen, which is responsible for CO₂ formation. Since PtO_x is already reduced, it has higher surface area resulting in more adsorption position on the surface. It follows that more methanol and oxygen molecules can adsorb and react on the catalysts, which influences on higher overall CO and CO₂ concentrations (products of methanol combustion) at the beginning of TPR2 compared to TPR1. Also during TPR2, relative concentration of hydrogen was up to 60% higher compared to TPR1. This can be explained by the incomplete reduction of platinum oxide at TPR1, where some oxygen still presents in catalytic layer after 150 °C. Lattice oxygen inhibits the SRM reaction (whereby we obtain major part of hydrogen). In contrary, TPR2 takes place on reduced Pt (no lattice oxygen, higher surface area), thus, higher hydrogen yield was observed.

Fig. 47 shows POM activity of the same sample (PtO_x/SiO₂) under molar ratio of CH₃OH:O₂ – 1:1. Same reaction products (H₂, CO, CO₂) as for stoichiometric case

were detected during both TPR1 and TPR2. From the activity test we can conclude that no improvement in POM selectivity under molar ratio of $\text{CH}_3\text{OH}:\text{O}_2 - 3:1$ was observed. On the contrary, higher CO_2 and CO yields and lower H_2 were detected compared to stoichiometric case. CO_2 peak at TPR1, which appears in the same temperature region as in previous experiment, presumes aforementioned reduction process of platinum oxide layer. Since we operated with methanol to oxygen molar ratios – 1:1, there is two times more oxygen in the feed mixture compared to stoichiometric (2:1) ratio.

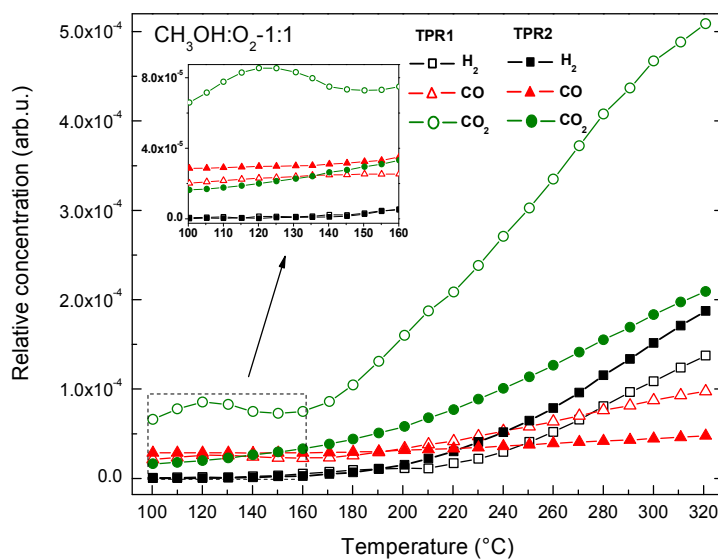


Fig. 47. Methanol oxidation activity of 10 nm $\text{PtO}_x/\text{SiO}_2$ sample at $\text{CH}_3\text{OH}:\text{O}_2 - 1:1$ molar ratio: relative concentrations of H_2 , CO and CO_2 plotted versus temperature (TPR1 - open symbols, TPR2 - solid symbols); inset - zoomed part of the same graph in 100 - 160 °C.

Thus, more methanol burns via methanol combustion reactions resulting in superior CO and CO_2 yields in the whole temperature range at both TPR1 and TPR2. TPR2 cycle takes place on already reduced platinum oxide layer ($\text{Pt}^{4+} \rightarrow \text{Pt}^0$) with increased surface area. Thus, concentrations of CO and CO_2 are higher at 100 °C (due to more pronounced methanol combustion process) compared to TPR1. Hydrogen yield of TPR2 is higher (about 40%) compared to TPR1. It is interesting that the difference of hydrogen yields between TPR1 and TPR2 under stoichiometric ratios was 60% (Fig. 46). This observation, along with more pronounced CO_2 peak suggests that the reduction of PtO_x layer takes place faster under $\text{CH}_3\text{OH}:\text{O}_2 - 1:1$ ratio – i.e. PtO_x reduces faster when more oxygen presents in gas feed mixture. This is because higher oxygen concentration in the methanol/oxygen feed mixture leads to more pronounced

methanol combustion processes. As a result, more molecules of CO (one of the products of methanol combustion) exposed the platinum oxide surface, which leads to faster reduction of PtO_x . But the excess of CO and CO_2 inhibits SRM and MD reactions, resulting in lower hydrogen yield in whole temperature range.

Previously, higher oxygen content in the reaction mixture ($\text{CH}_3\text{OH}:\text{O}_2 - 1:1$) did not improve the POM activity on PtO_x . Therefore we decided to decrease the amount of oxygen by setting methanol to oxygen molar ratios – 3:1. The following improvement of POM activity compared to stoichiometric case was observed from *Fig. 48*: higher H_2 and lower CO_2 yields together with a very low concentration of CO during both TPR1 and TPR2. Due to lower concentration of oxygen in present reaction mixture, less methanol molecules burned, resulting in lower CO and CO_2 production at initial temperatures of TPR1. After TPR1 the sample is stabilized (reduced), so TPR2 predictably runs on metallic platinum with higher surface area, thus, demonstrates better selectivity.

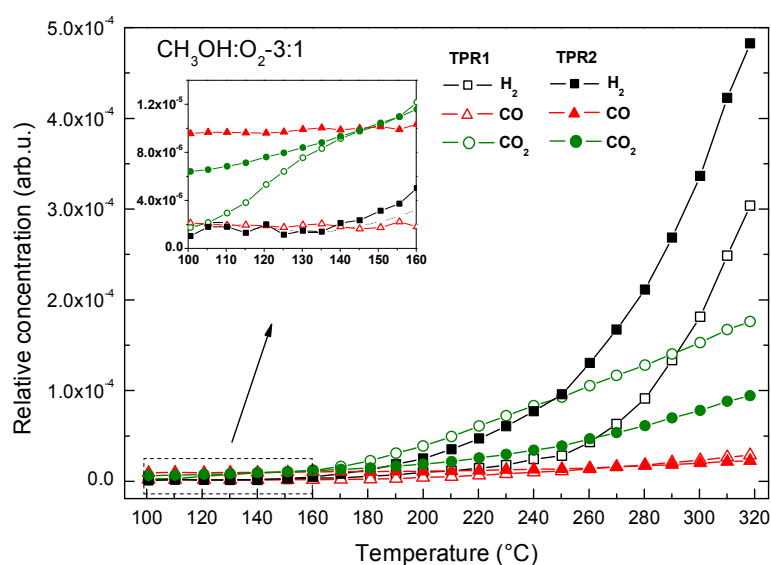


Fig. 48. Methanol oxidation activity of 10 nm $\text{PtO}_x/\text{SiO}_2$ sample at $\text{CH}_3\text{OH}:\text{O}_2 - 3:1$ molar ratio: relative concentrations of H_2 , CO and CO_2 plotted versus temperature (TPR1 - open symbols, TPR2 - solid symbols); inset - zoomed part of the same graph in 100 - 160 °C.

Regarding hydrogen yields (*Fig. 48*), TPR2 demonstrated up to 60% higher concentration compared to TPR1 at 320 °C (same behavior as for stoichiometric case). Therefore, under such ratio of reactants platinum oxide reduces with similar rate as in stoichiometric case. High selectivity toward hydrogen can be explained by more pronounced SRM and MD reactions, which are not inhibited by the products of

the combustion of methanol. Thus, methanol molecules instead of burning (as in case with 2:1 and 1:1 ratios of reactants) reacted with H₂O (SRM) and decomposed (MD) to favorable H₂ molecules.

Since low oxygen content in gas feed mixture (CH₃OH:O₂ – 3:1) improved the POM selectivity, we decided to check the methanol oxidation reaction without oxygen – i.e. methanol decomposition (MD). Generally MD on precious metals starts with an adsorption of CH₃OH molecules on the surface with further scissions of O-H bond to the methoxy (CH₃O) intermediate. Afterwards the methoxy decomposes to carbon monoxide and hydrogen [76]. On Pt(111) surface methanol adsorbs and decomposes to the aforementioned products without any intermediates [77,78]. In our case MD performs over platinum oxide layer, so we expected the similar mechanism, taking into account easy reduction of the PtO_x to metallic platinum. From Fig. 49 it is seen that MD experiment predictably generated only H₂ and CO, but the overall reaction efficiency is far less compared to POM reactions. The graph showed that the reaction starts at around 230 °C, simultaneously yielding H₂ and CO.

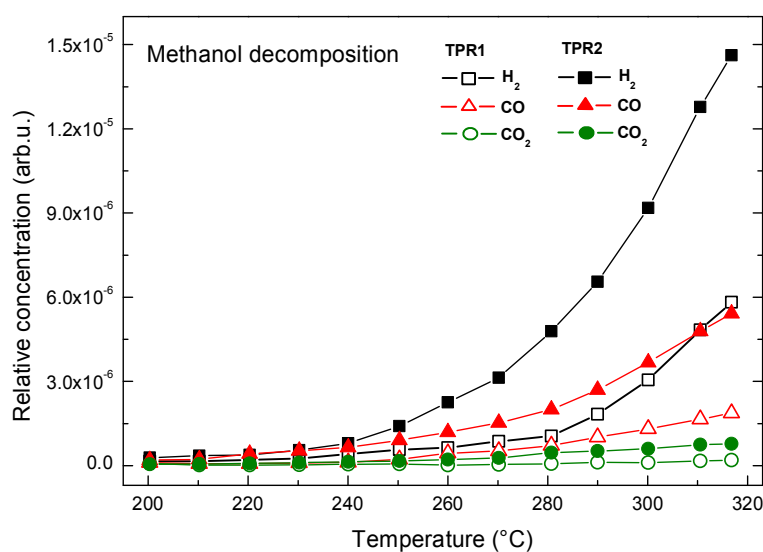


Fig. 49. Methanol decomposition on 10 nm PtO_x/SiO₂ sample: relative concentrations of H₂, CO and CO₂ plotted versus temperature (TPR1 - open symbols, TPR2 - solid symbols).

Only small concentration of CO₂ is presented at the end of TPR1. We suppose that the mechanism formation of carbon dioxide is similar with that of POM experiments. Carbon monoxide reacts with the lattice oxygen of PtO_x and produces CO₂ which can be seen on CO₂ production curve at higher temperatures of TPR1. TPR2 predictable runs on already reduced Pt surface (Pt⁰), so there is no more lattice oxygen inside.

That is why we did not analyze the CO_2 during TPR2. Furthermore, we observed higher yield of products (H_2 and CO) predictably due to the increased surface area. It is interesting that the carbon monoxide onset (240 - 260 °C) of MD experiments matched with an apparent increase of CO concentrations in POM experiments, thus, we can assume that MD reaction is a final step of POM on PtO_x thin film.

Direct comparison of hydrogen yields produced from POM and MD reactions is presented in *Fig. 50a*.

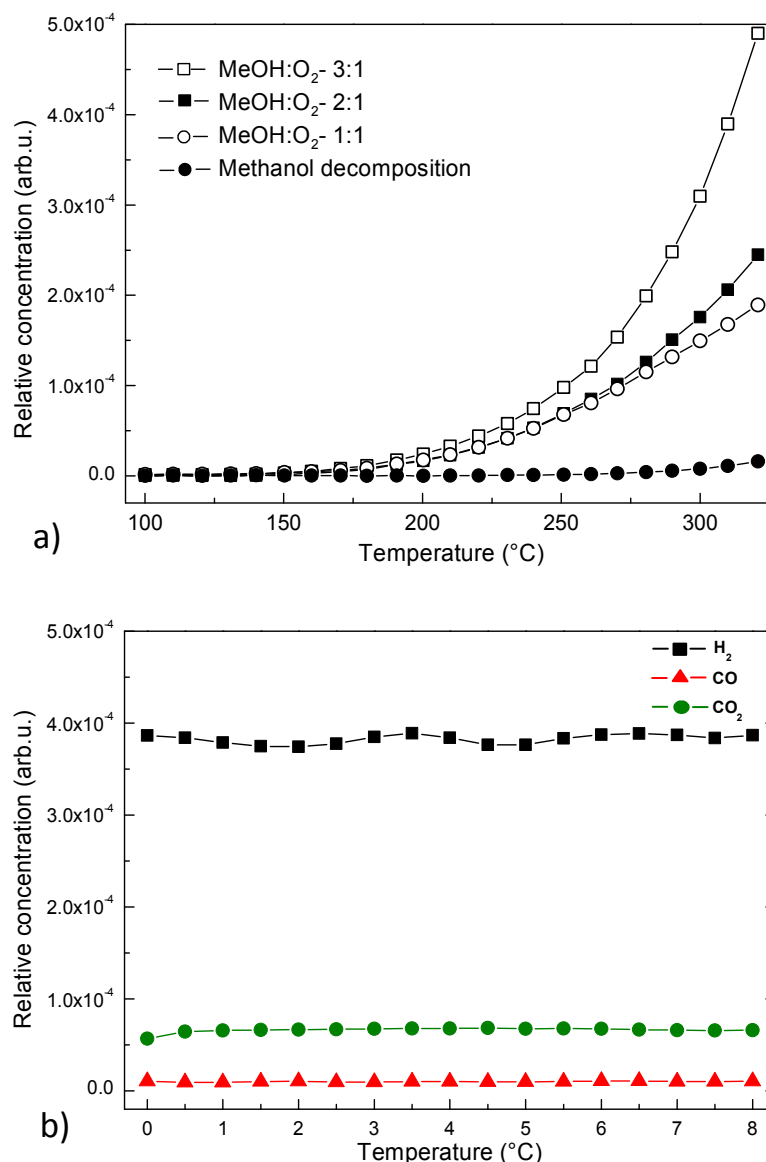


Fig. 50: a) Comparison of hydrogen yields of TPR2 for different $\text{CH}_3\text{OH}:\text{O}_2$ molar ratios on 10 nm $\text{PtO}_x/\text{SiO}_2$ sample. Methanol decomposition experiment added as a reference. b) Time-on-stream examination of 10 nm $\text{PtO}_x/\text{SiO}_2$ sample at $T = 300^\circ\text{C}$ (molar ratio of $\text{CH}_3\text{OH}:\text{O}_2 = 3:1$).

We can see that the relative concentration of H₂, generated by MD is significantly lower than the H₂ produce by POM. Regarding the POM reaction, less oxygen content in the feed gas mixture (3:1) leads to overall higher hydrogen yield.

Time-on-stream test at 300 °C (under MeOH:O₂ – 3:1) exhibited stable behavior of the platinum oxide thin film (*Fig. 50b*). We selected such high testing temperature (the highest possible for our sample holder) in order to apply a maximum thermal stress on PtO_x layer. By the way, no activity degradation during an 8 hour test was observed.

In this work, we checked POM activity on 10 nm PtO_x/SiO₂ sample under different CH₃OH:O₂ molar ratios. Also methanol decomposition and time-on-stream tests were done. From the aforementioned experiments we can conclude that the increasing concentration of oxygen in the feed mixture leads to higher CO and CO₂ and lower H₂ yields. In contrary, decreasing the oxygen flows results in better selectivity toward hydrogen and worst one toward CO and CO₂. Platinum oxide thin film catalyst prepared by magnetron sputtering technique is a good candidate for hydrogen production via POM. Being only 10 nm thick, such catalyst demonstrated good activity and stability. Moreover, operating with low concentration of oxygen in the gas feed mixture (CH₃OH:O₂ – 3:1) leads to selectivity advantages compared to the stoichiometric (2:1) ratio.

4.3.4. POM on Pt-CeO₂ layers with different Pt loading

It was shown above that Pt and PtO_x thin films show high catalytic activity for POM reaction. However, platinum is a noble metal and has a high price. In order to reduce the cost of catalyst for POM reaction it was proposed to prepare composite. Pt-CeO₂ thin films with low platinum content. Ceria was chosen as the best candidate for mixing with Pt due to its good catalytic properties (e.g. oxygen storage capacity, high WGS activity) and low cost [31]. In order to study the POM mechanism on platinum-ceria layers with high and low Pt content, platinum-ceria catalysts with thicknesses of 10 nm were deposited on flat SiO₂ substrates using magnetron sputtering technique. Additionally, reference pure CeO₂ and metallic Pt films of the same thickness were also prepared by magnetron sputtering. DC and RF magnetrons were used for depositions of Pt and CeO₂ respectively. In order to prepare Pt-CeO₂ thin films, simultaneously deposition from both RF and DC magnetrons (RF-DC

deposition) was carried out. To obtain low and high contents of platinum in Pt-CeO₂ layers, RF power was adjust to 30 W and 90 W, while DC power staying constant at 10 W.

After depositions, platinum-ceria samples were analyzed by laboratory XPS. In Fig. 51 the measured Ce 3d and Pt 4f XPS spectra are presented.

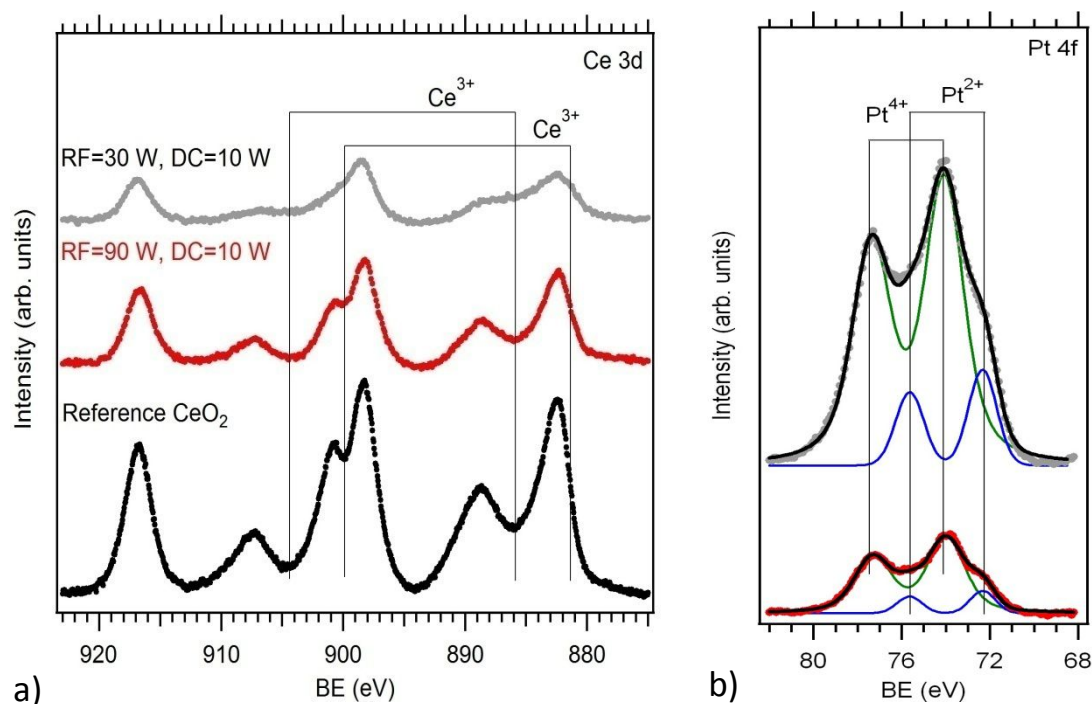


Fig. 51. Ce 3d (a) and Pt 4f (b) XPS spectra of Pt-CeO₂/SiO₂ samples prepared at RF magnetron power of 30 W (gray spectrum) and 90 W (red spectrum) while DC power kept at 10 W. For the comparison purpose, Ce 3d spectrum of the reference CeO₂ thin film was included (black spectrum).

The Pt 4f spectra showed that in both cases Pt is mainly in Pt⁴⁺ ionic state (around 80%), however, small amount of Pt²⁺ can be also seen. The Ce 3d spectra demonstrated that CeO₂ is partially reduced, and the reduction increases with increasing Pt content in the Pt-CeO₂ layers. The reduction of ceria can be seen from the appearance of two additional doublets at 881.2 eV and 885.8 eV [79]. Relative Pt/Ce atomic concentration of platinum in the Pt-CeO₂ layers calculated from the areas of the Pt 4f and Ce 3d XPS peaks were 0.15 and 0.56, respectively (Ce 3d and Pt 4f peak areas were corrected using corresponding sensitivity factors). Therefore the following four samples were prepared: Pt(0.15)-CeO₂/SiO₂ and Pt(0.56)-CeO₂/SiO₂ (where 0.15 and 0.56 are the relative Pt/Ce atomic concentration of platinum in the Pt-CeO₂ layers) as well as references CeO₂/SiO₂ and Pt/SiO₂.

Morphology of as prepared Pt/SiO₂ sample is flat and continuous as well as after the POM reaction (the same sample is well described in *subchapter 4.3.1*). As prepared both Pt(0.15)-CeO₂/SiO₂ and Pt(0.56)-CeO₂/SiO₂ samples demonstrated continuous and flat surface (*Fig. 52a*, here only Pt(0.15)-CeO₂/SiO₂ specimen shown due to its similar morphology). In contrary, morphology of the as prepared CeO₂/SiO₂ specimen is rough with sparse grains about 50 nm in diameter (*Fig. 52b*). After the POM reaction no morphology changes were observed on aforementioned samples (*Fig. 52 c, d*).

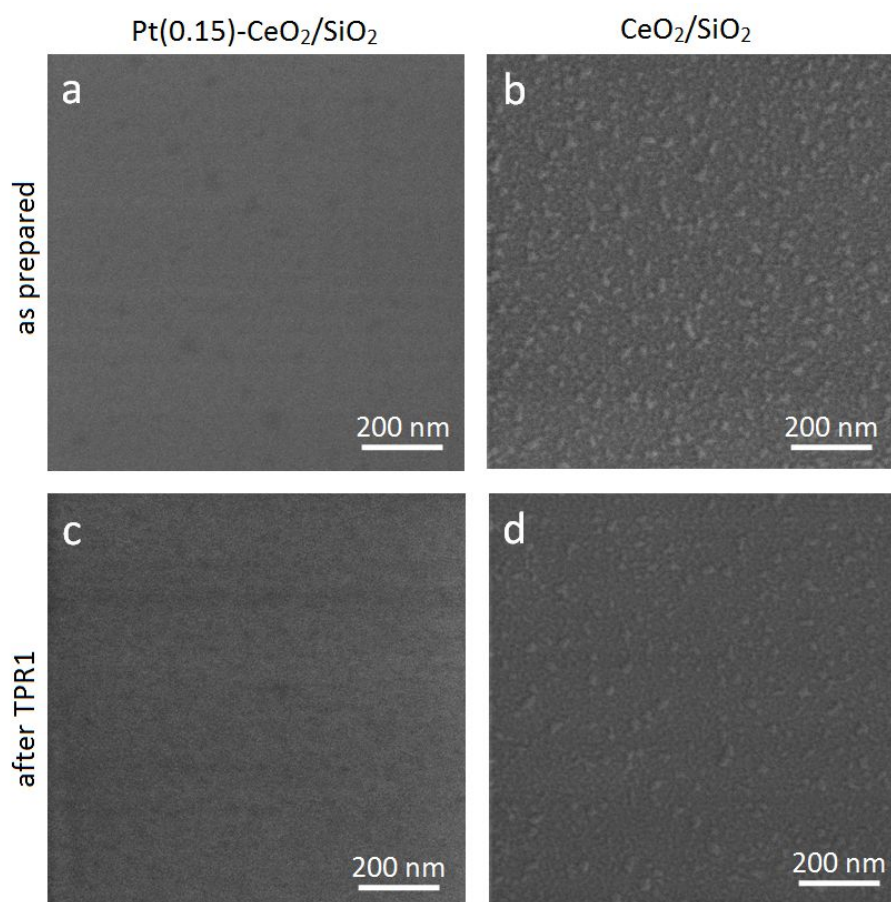


Fig. 52. SEM images of as prepared 10 nm thick Pt(0.15)-CeO₂/SiO₂ sample (a) and the same sample after POM (c); as prepared 10 nm thick CeO₂/SiO₂ (b) and after POM (d).

POM reaction over prepared specimens was performed on the laboratory microreactor system. All measurement conditions were same as for the previous POM experiments. *Fig. 53* shows the comparison of POM activities of CeO₂/SiO₂ and Pt(0.15)-CeO₂/SiO₂ samples. The Pt(0.15)-CeO₂/SiO₂ catalyst shows up to 60% higher hydrogen yield and up to 40% lower CO one at highest reaction temperatures

(320 °C). Also 1.5 times more CO₂ were detected on such sample compared to the CeO₂/SiO₂ specimen at 320 °C.

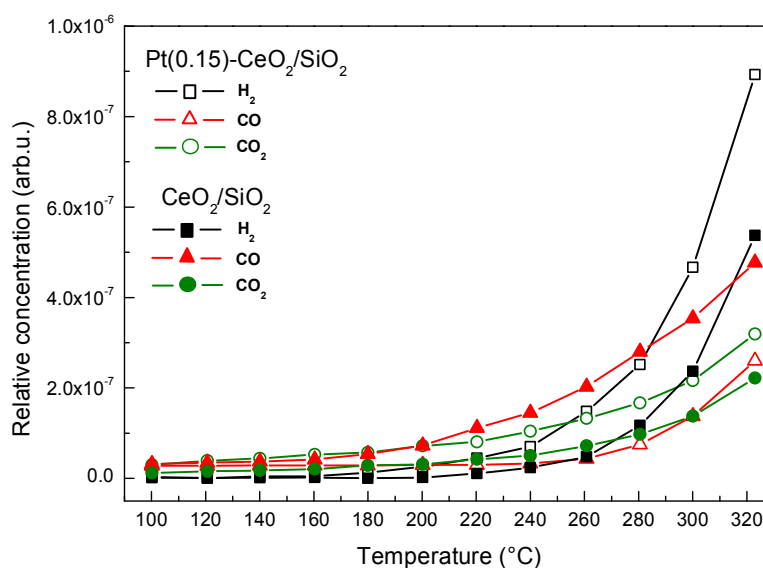


Fig. 53. Comparison of POM activities of Pt(0.15)-CeO₂/SiO₂ and CeO₂/SiO₂ samples: relative concentrations of H₂, CO, and CO₂ plotted versus temperature.

Fig. 54 shows the comparison of POM activities of Pt(0.56)-CeO₂/SiO₂ and Pt/SiO₂ samples. The Pt(0.56)-CeO₂/SiO₂ specimen produced the same hydrogen yield as the Pt/SiO₂ below 260 °C.

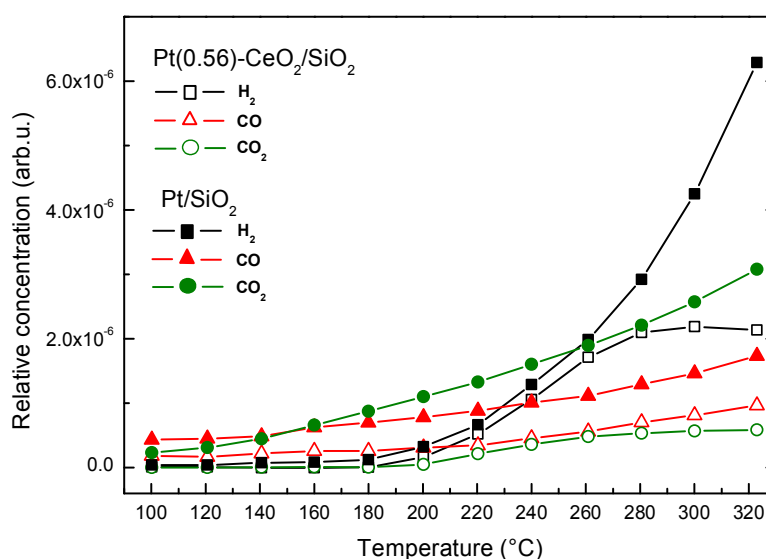


Fig. 54. Comparison of POM activities of Pt(0.56)-CeO₂/SiO₂ and Pt/SiO₂ samples: relative concentrations of H₂, CO, and CO₂ plotted versus temperature.

Above 260 °C, the hydrogen concentration curve of Pt(0.56)-CeO₂/SiO₂ reached saturations (i.e. H₂ concentration does not change with the increasing of the temperature), while the hydrogen concentration of Pt/SiO₂ sample continues to grow. At the highest reaction temperature the Pt/SiO₂ sample exhibits 3 times bigger hydrogen yield than Pt(0.56)-CeO₂/SiO₂. Regarding the CO and CO₂ production yields, platinum-ceria thin film has advantages: 2 times lower CO and 3 times lower CO₂ yields in whole temperature range.

Fig. 55 shows the direct comparison of hydrogen yields from the aforementioned samples. From the graph it can be seen that CeO₂/SiO₂ sample demonstrated only 14% of hydrogen yield obtained on Pt/SiO₂ at the end of TPR (320 °C). Hydrogen yield of the Pt(0.15)-CeO₂/SiO₂ specimen is two times less compared to the Pt(0.56)-CeO₂/SiO₂.

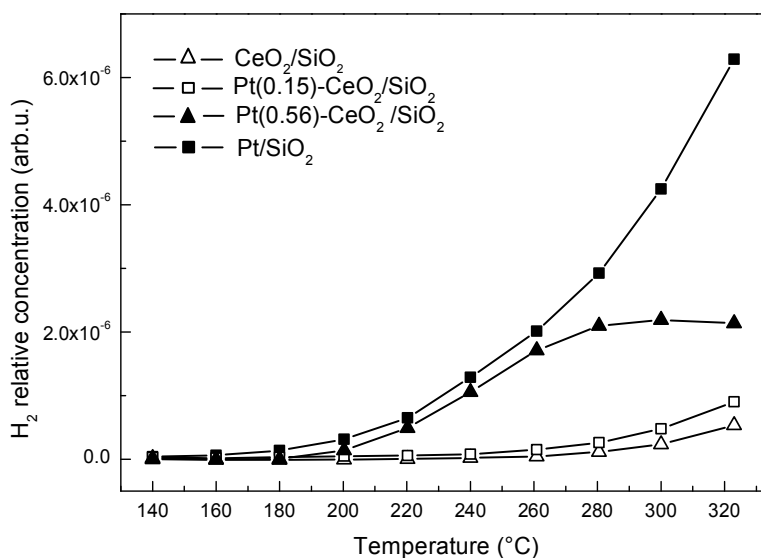


Fig. 55. Hydrogen yields comparison of Pt(0.15)-CeO₂/SiO₂, Pt(0.56)-CeO₂/SiO₂ as well as references CeO₂/SiO₂ and Pt/SiO₂ samples.

Regarding the POM route on Pt/SiO₂ sample (Fig. 54), methanol burns via combustion reactions yielding water, CO and CO₂ at low temperatures (100 - 150 °C). Then, SRM starts, yielding H₂ (150 °C onset) and CO₂. Over 260 °C MD occurs and produces additional hydrogen and CO. During the POM on the CeO₂/SiO₂ sample (Fig. 53), methanol combustion reaction (CH₃OH + O₂ → 2H₂O + CO) is weak due to low CO and H₂O yields detected at initial temperature. As a result, lower amount of water is involved in SRM to produce hydrogen at higher temperatures. As we stated before, SRM reaction includes MD and WGS. Since MD takes place hardly

on ceria layer (it decomposes to water and CH_2O [60]) this leads to considerably low hydrogen yield and shifting hydrogen onset over $200\text{ }^\circ\text{C}$ compared to Pt/SiO_2 sample. Only above $260\text{ }^\circ\text{C}$, hydrogen started to produce mostly through WGS reaction (18), because of its relatively good WGS activity on ceria [80].

The $\text{Pt}(0.15)\text{-CeO}_2/\text{SiO}_2$ sample shows similar activity as the $\text{CeO}_2/\text{SiO}_2$ one, but different selectivity (*see Fig. 53*). In this case, the presence of platinum in $\text{Pt}(0.15)\text{-CeO}_2/\text{SiO}_2$ specimen resulted in more pronounced methanol combustion process at initial temperatures, which yields CO , CO_2 and H_2O . Also shifted hydrogen onset (from $175\text{ }^\circ\text{C}$ to $150\text{ }^\circ\text{C}$) and higher (up to 60%) hydrogen yield at $320\text{ }^\circ\text{C}$ indicate more pronounced SRM reaction (due to more H_2O from methanol combustion reactions) compared to $\text{CeO}_2/\text{SiO}_2$ specimen.

POM reaction on $\text{Pt}(0.56)\text{-CeO}_2/\text{SiO}_2$ sample demonstrated comparable overall efficiency to Pt/SiO_2 one (*Fig. 54*). Two times less CO and CO_2 at initial temperatures ($100\text{ }^\circ\text{C}$) observed on $\text{Pt}(0.56)\text{-CeO}_2/\text{SiO}_2$ specimen suggests that only half of the supplied methanol converts via methanol combustion reactions compared to Pt/SiO_2 sample. This can be explained by poor methanol combustion reaction on ceria, which is occupied about half of the surface of $\text{Pt}(0.56)\text{-CeO}_2/\text{SiO}_2$ sample. Below $260\text{ }^\circ\text{C}$ hydrogen onsets and behavior of H_2 concentration curves are same for both samples, so we observed similar SRM process. Above $260\text{ }^\circ\text{C}$, the concentration of H_2 and CO_2 reached saturations, while the CO concentration curve continues to grow on $\text{Pt}(0.56)\text{-CeO}_2/\text{SiO}_2$. In contrary Pt/SiO_2 specimen exhibited increasing of concentrations of all products (H_2 , CO and CO_2) in whole temperature range.

In order to investigate the stable behavior of H_2 and CO_2 concentration curves observed above $260\text{ }^\circ\text{C}$ on $\text{Pt}(0.56)\text{-CeO}_2/\text{SiO}_2$ sample, TPR2 run was done on it after cooling down the specimen (*Fig. 56*). During TPR2 a two-fold decrease of hydrogen yield was observed at $320\text{ }^\circ\text{C}$. Also less CO (up to 25%) and CO_2 (up to 20%) concentrations in whole temperature range were detected. Such activity decline can be explained by diffusion of platinum from the upper layers into the bulk of the Pt-CeO_2 film during the heating up procedure [81]. This process resulted in slowdown of H_2 and CO_2 yields i.e. SRM reaction was inhibited due to more ceria appearing on the surface of thin film. As a result, the activity of $\text{Pt}(0.56)\text{-CeO}_2/\text{SiO}_2$ sample during TPR2 decreased to the level of $\text{Pt}(0.15)\text{-CeO}_2/\text{SiO}_2$, where ceria content is higher (*Fig. 53*).

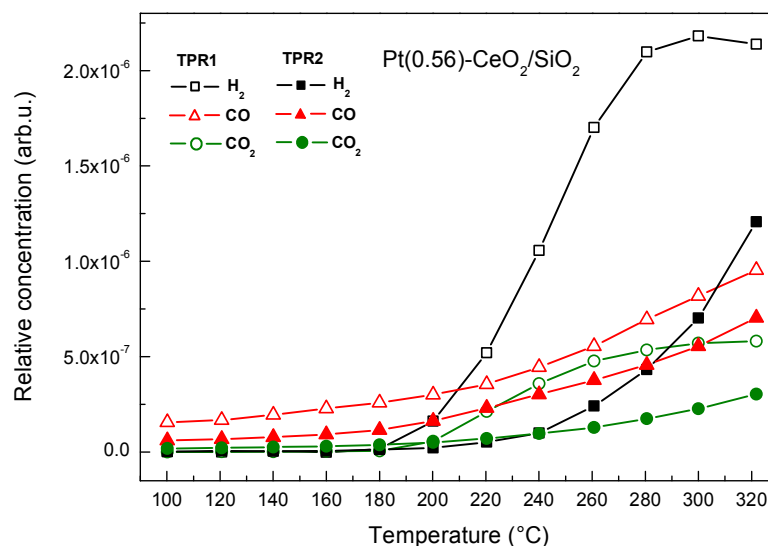


Fig. 56. Comparison of POM activities of TPR1 and TPR2 on Pt(0.56)-CeO₂/SiO₂ sample: relative concentrations of H₂, CO and CO₂ plotted versus temperature (TPR1- open symbols, TPR2 - solid symbols).

10 nm thick Pt-CeO₂ layers showed various activities for POM reaction, depending on the platinum content. When the Pt content is low (Pt(0.15)-CeO₂/SiO₂ sample) the activity is similar to pure ceria layer with same thickness. If the Pt content is high (Pt(0.56)-CeO₂/SiO₂), we observed better activities compared to pure platinum catalyst with the same thickness (same H₂ yield, lower CO and CO₂ ones), but only below 260 °C. Above 260 °C, platinum diffused from the surface into the bulk of the Pt-CeO₂ film resulted in the activity decrease. However, using the Pt(0.56)-CeO₂ thin films for POM reaction in 100 - 260 °C temperature region leads to an economical advantage (2 times less platinum content, i.e. - cheaper catalyst) and better overall activity compared to pure Pt.

4.3.5. POM on very thin Pt/CeO₂, Pt-CeO₂ and Pt layers

In previous experiments it was shown that the activity decrease of 10 nm thick Pt(0.56)-CeO₂ catalyst above 260 °C can be due to the diffusion of platinum from the surface into the depth of Pt-CeO₂ thin film. Since chemical reaction takes place on the upper monolayer of the catalysts it was decided to check the POM activity on Pt and Pt-CeO₂ thin films with thicknesses of around nanometer. Other goal was to confirm the possibility of diffusion of the 1 nm thick Pt layer into 10 nm thick CeO₂ interlayer during the reaction. Therefore we deposited Pt and CeO₂ thin films on SiO₂ substrate using magnetron sputtering technique. First, 10 nm thick CeO₂ layer has been grown

on SiO₂ substrate followed by deposition of the 1 nm Pt on it. Also 1 nm thick Pt and Pt-CeO₂ layers (simultaneously deposited from Pt and CeO₂ target) were grown on SiO₂ substrates. Hence, the following three samples were prepared: Pt(1 nm)/CeO₂(10 nm)/SiO₂, Pt-CeO₂(1 nm)/SiO₂ and Pt(1 nm)/SiO₂ as a reference. POM reaction (TPR1 and TPR2 cycles) was performed on prepared samples under the same conditions as for previous experiments. Also samples were analyzed by XPS and SEM techniques before and after the reaction.

All freshly prepared specimens exhibited flat and continuous morphology (Fig. 57a, b, c) only Pt(1 nm)/CeO₂(10 nm)/SiO₂ sample has more rough surface because of the 10 nm ceria interlayer (see previous *subchapter*, Fig. 52b).

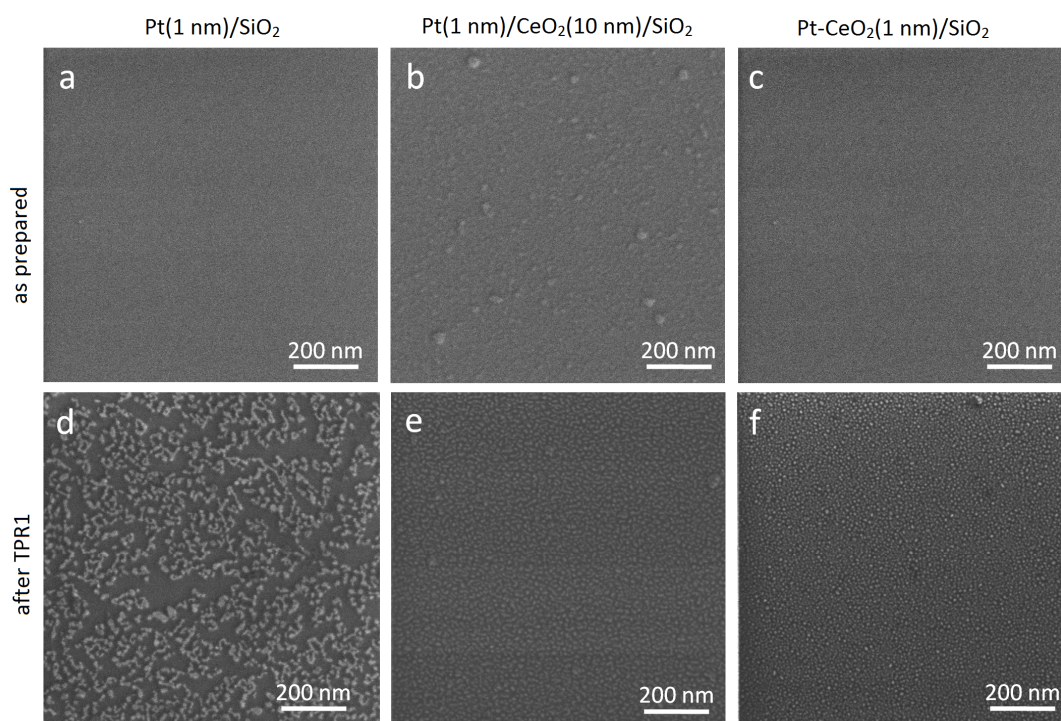


Fig. 57. SEM images of Pt(1 nm)/SiO₂ sample as prepared (a) and after POM TPR1(d); Pt(1 nm)/CeO₂(10 nm)/SiO₂ as prepared (b) and after POM TPR1 (e); Pt-CeO₂(1 nm)/SiO₂ as prepared (c) and after POM TPR1 (f).

Morphology of Pt(1 nm)/SiO₂ sample after POM TPR1 exhibited coalescence of Pt into small islands (approx. 10 nm in diameter). In addition, the SiO₂ substrate becomes visible on approx. half of the analyzed surface (Fig. 57d). The Pt(1 nm)/CeO₂(10 nm)/SiO₂ sample after TPR1 exhibited granular surface structure with 20 nm grains in diameter (Fig. 57e). Similar morphology after TPR1 stage

exhibited Pt-CeO₂(1 nm)/SiO₂ thin film (Fig. 57f), but differs in higher density of grains, which has more rounded shape.

POM activity on Pt(1 nm)/CeO₂(10 nm)/SiO₂ sample demonstrated in Fig. 58. H₂, CO and CO₂ were detected as the main reaction products during both TPR1 and TPR2.

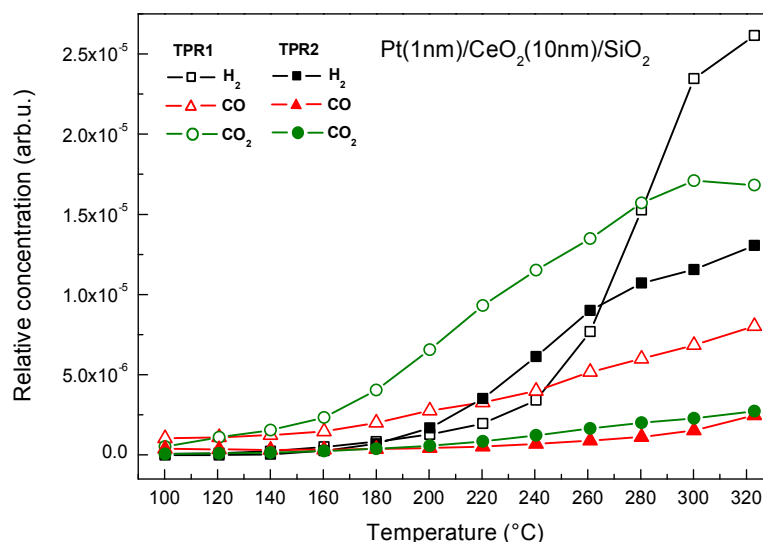


Fig. 58. POM activity of the Pt(1 nm)/CeO₂(10 nm)/SiO₂ sample: relative concentrations of H₂, CO and CO₂ plotted versus temperature (TPR1 - open symbols, TPR2 - solid symbols).

In the end of TPR1 (320 °C) the ratio of hydrogen to CO₂ remains lower than the stoichiometry of POM (2:1) described in *subchapter 4.3*. At TPR2, overall efficiency of such thin film decreased: two times lower concentrations of H₂ and CO at 320 °C have been observed. The CO and CO₂ yields were almost the same at TPR2 in whole temperatures range, while during TPR1 a relative CO₂ concentration was detected two times higher than CO.

Ce 3d XPS spectrum of the as prepared Pt(1 nm)/CeO₂(10 nm)/SiO₂ sample (“Pt/CeO₂” spectrum in Fig. 59a) demonstrated that the deposition of 1 nm of Pt on stoichiometric ceria leads to its partial reduction (same as in Fig. 51, previous chapter). It can be also seen that after the first TPR cycle the reduction of ceria increased even more (“after TPR1” spectrum in Fig. 59a). After the second TPR cycle the ceria atoms re-oxidized back to the previous state (“after TPR2” spectrum in Fig. 66a). The Pt 4f spectra showed only the decreasing intensity of metallic platinum peak (Pt⁰) after TPR1 and TPR2 (Fig. 59b).

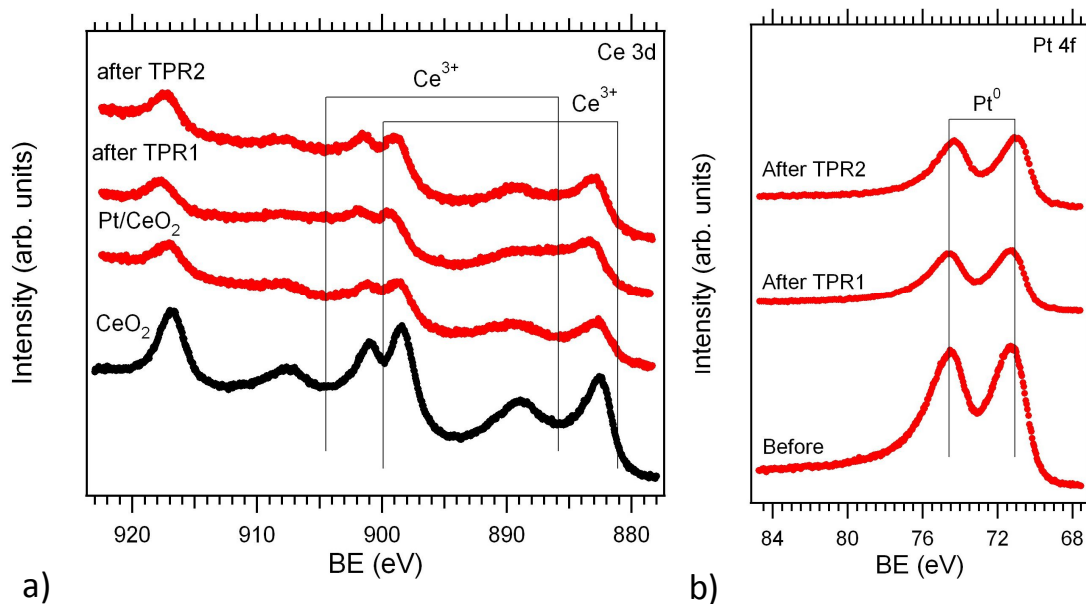


Fig. 59. Ce 3d (a) and Pt 4f (b) spectra of Pt(1 nm)/CeO₂(10 nm)/SiO₂ sample at different conditions: before the reaction, after the TPR1 and after the TPR2. For the comparison purpose, Ce 3d spectrum of reference CeO₂ thin film was included (black spectrum in (a)).

From the activity plots we can conclude that the activity degradation of Pt(1 nm)/CeO₂(10 nm)/SiO₂ sample during TPR2 (Fig. 58) is the result of the disappearance of the active platinum from the surface of the thin film. Regarding XPS analysis, decreasing of the intensity of Pt⁰ peak after TPR1 (Fig. 59b) suggests that the surface Pt seems like coalesced in clusters and then encapsulated by CeO₂ [81,82]. Moreover, surface morphology of such sample after TPR1 became grained (Fig. 57e), that confirms the possibility of coalescence of Pt with following encapsulation of it by ceria. Since, ceria is not as active as platinum for POM (see previous *subchapter*), we monitored lower overall efficiency during TPR2.

POM activity of Pt(1 nm)/SiO₂ sample (Fig. 60) demonstrated almost similar concentrations of products at both TPR1 and TPR2 except the concentration of CO₂, which was detected in two times higher during TPR1. Also at TPR1 we observed increased of the H₂ concentration in the temperature region between 175 and 240 °C (i.e. hydrogen “hump”).

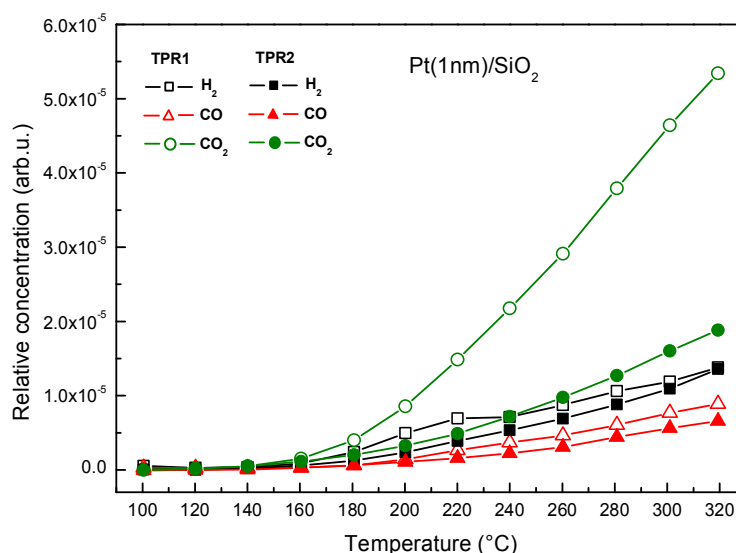


Fig. 60. POM activity of Pt(1 nm)/SiO₂ sample: relative concentrations of H₂, CO and CO₂ plotted versus temperature (TPR1 - open symbols, TPR2 - solid symbols).

The XPS spectra (wide scans) of the Pt(1 nm)/SiO₂ sample (as prepared and after TPR1 cycle) are presented in Fig. 61. They showed visible Pt⁰ doublet before the reaction. After TPR1 the metallic platinum peak drastically decreased, while the O 1s was increased (Si 2p was slightly increased too).

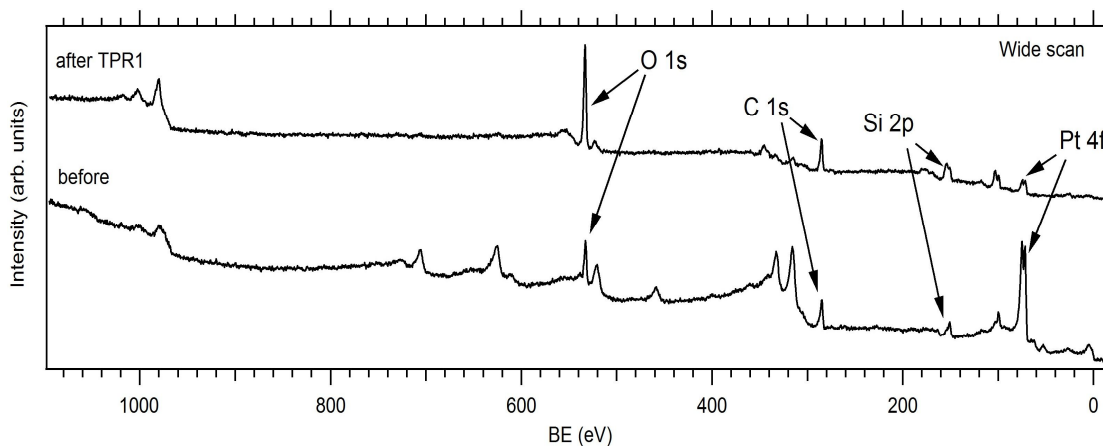


Fig. 61. XPS spectra (wide scan) of Pt(1 nm)/SiO₂ sample: before (bottom spectrum) and after TPR1 stages (top spectrum).

The Pt(1 nm)/SiO₂ specimen during the TPR2 stage demonstrated stable behavior – i.e. concentrations of products very similar to TPR1 cycle (Fig. 60). Since only pure metallic platinum was deposited, surface morphology of the as prepared specimen is flat and continuous. But after TPR1 cycle Pt conglomerated in small islands with a visible SiO₂ substrate (Fig. 57a, d). In addition, XPS analysis showed

the increase of oxygen and silica peaks (both originated from SiO₂ substrate) after the TPR1, while Pt⁰ doublet was decreased. From XPS and SEM analysis we assumed that the aforementioned H₂ “hump” in POM activity data during TPR1 (*Fig. 60*) can be associated with morphology changes of the specimen i.e. coalescence of Pt in islands. Such process is accompanied with the losing the active surface area of the catalyst thin film and stabilizing the Pt surface within 175 - 240 °C region. Thus H₂ concentration did not increase linearly below 250 °C. Less CO₂ yield during TPR2 can be explained by losing the active Pt surface where methanol burns to H₂O, CO and CO₂ at the initial temperature of the reaction (see *subchapter 4.3.1*).

The Pt-CeO₂(1 nm)/SiO₂ sample demonstrated a good stability during both TPRs (*Fig. 62*). In this case almost the same H₂ yields for TPR1 and TPR2 were observed. During TPR2 the concentrations of CO and CO₂ were two times lower in whole temperature range compared to TPR1.

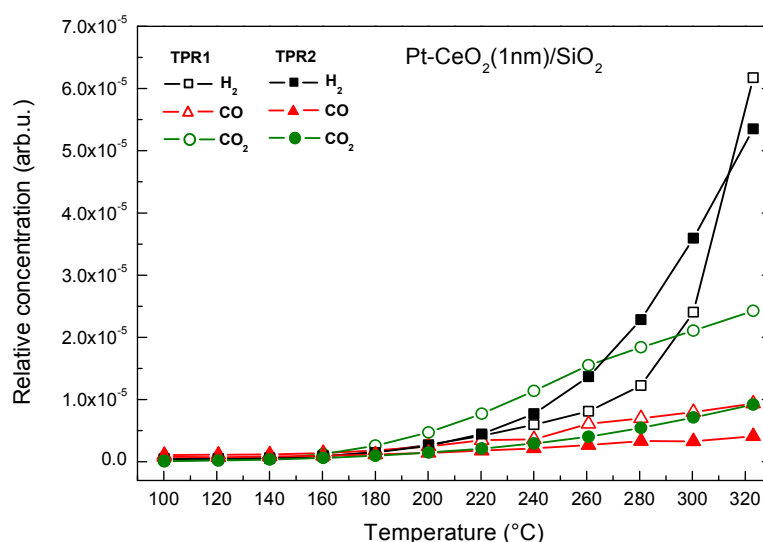


Fig. 62. Methanol oxidation activity of Pt-CeO₂(1 nm)/SiO₂ sample: relative concentrations of H₂, CO and CO₂ plotted versus temperature (TPR1 - open symbols, TPR2 - solid symbols).

Ce 3d and Pt 4f XPS spectra of the as prepared and after TPR2 cycles Pt-CeO₂(1 nm)/SiO₂ sample are presented in *Fig. 63*. The relative atomic concentration of Pt in Pt-CeO₂ layer is calculated from areas of the Pt 4f and Ce 3d XPS spectra of the as prepared sample was found to be Pt/Ce = 0.85 (Ce 3d and Pt 4f peak areas were corrected using corresponding sensitivity factors).

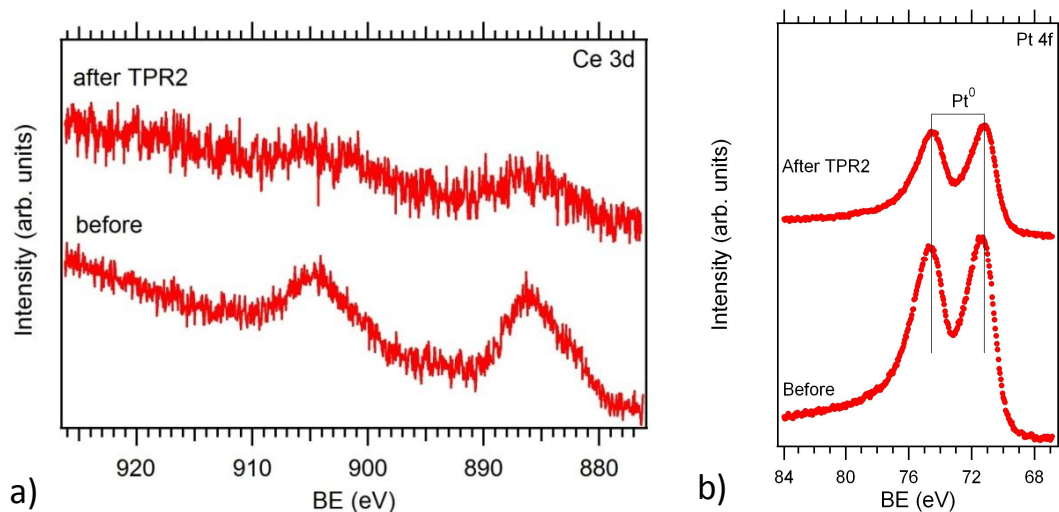


Fig. 63. Ce 3d (a) and Pt 4f (b) spectra of Pt-CeO₂(1 nm)/SiO₂ sample before the reaction and after the TPR2.

From the Ce 3d spectrum we can notice that the as deposited layer contains cerium completely in 3+ ionic state. The reduction is caused by the interaction of Pt (concentration of which is very high) with ceria and also by the interaction of the very thin Pt-CeO₂ layer with the silica substrate [83]. The Ce 3d spectra demonstrated a decrease in intensity of CeO₂ doublets after TPR2 that could be the result of coalescence of Pt-CeO₂ film in grains. The Pt 4f spectra showed the metallic Pt in both before and after TPR2 cases, however after TPR2 Pt 4f spectrum also exhibited decreasing of the metallic platinum doublet. Activity data exhibited the similar concentration of products on Pt-CeO₂(1 nm)/SiO₂ sample during both TPR1 and TPR2 - i.e. the catalyst is stable (Fig. 62). Since such layer is only 1 nm thick and it has high Pt content (Pt/Ce = 0.85), it is less probable for Pt to diffuse into the depth of the thin film, in contrary to 10 nm thick Pt-CeO₂(0.56)/SiO₂ sample, where Pt content is lower (see previous *subchapter*). As a result no activity degradation was observed during TPR2, only lower relative concentrations of CO and CO₂ i.e. - better selectivity. Surface morphology of the as prepared Pt-CeO₂(1 nm)/SiO₂ sample is flat and homogeneous, but after TPR1 it becomes grained (Fig. 57c, f). XPS spectra (Fig. 63) showed less pronounced ceria and platinum (Pt⁰) peaks after TPR1, which can be explained by the coalescence of the thin Pt-CeO₂ film into bigger islands. An interesting finding is that we did not observe such granular structure on Pt(1 nm)/SiO₂ sample after TPR1. This means that the only presence of ceria in a very thin Pt-CeO₂(1 nm)/SiO₂ specimen (Pt/Ce = 0.85) leads to the formation of a granular

surface structure, in contrary to ceria free sample (Pt(1 nm)/SiO₂) where Pt was coalesced into small islands with uncovered SiO₂ substrate (*Fig. 57d*).

Direct comparison of hydrogen yields of the aforementioned samples during TPR2 is presented in *Fig. 64*. Both Pt(1 nm)/SiO₂ and Pt(1 nm)/CeO₂(10 nm)/SiO₂ specimens show similar hydrogen yields at highest reaction temperature (320 °C).

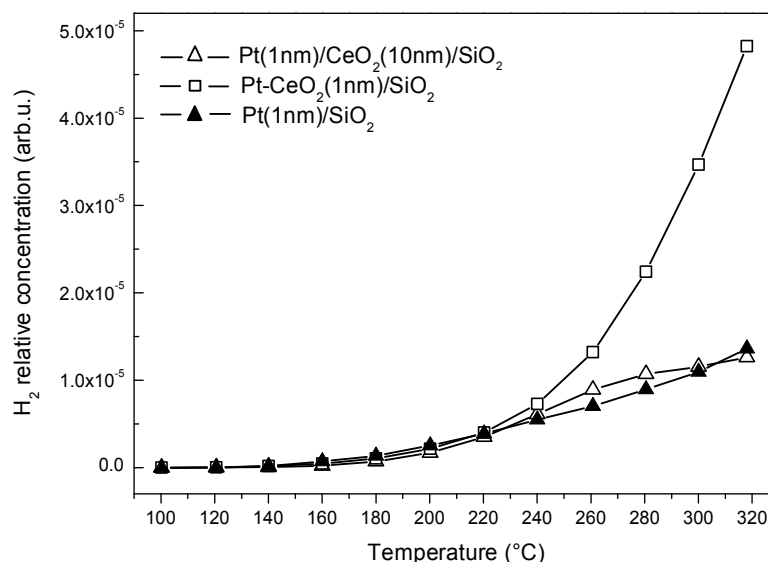


Fig. 64. Comparison of hydrogen yields over Pt(1 nm)/CeO₂(10 nm)/SiO₂, Pt-CeO₂(1 nm)/SiO₂ and reference Pt(1 nm)/SiO₂ samples.

During the TPR1 these samples have lost part of active platinum surface in different manners. Linear increasing of the H₂ concentration curve of Pt(1 nm)/SiO₂ specimen (in *Fig. 64*) indicates that such sample was already stabilized during TPR1, where Pt film conglomerated in islands below 250 °C and became stable at higher reaction temperature (*Fig. 60*). Regarding the Pt(1 nm)/CeO₂(10 nm)/SiO₂ sample, we observed the coalescence of Pt together with the following encapsulation by ceria during TPR1. Non linear behavior of hydrogen production curves of Pt(1 nm)/CeO₂(10 nm)/SiO₂ sample in *Fig. 64* indicates that such specimen still is not stabilized enough. We are expecting more pronounced encapsulating process of Pt with further repeating the TPR procedure, so that the activity will be decreased more. The hydrogen yield of the Pt-CeO₂(1 nm)/SiO₂ sample is 5 times higher than the aforementioned specimens. In this case the active surface area was preserved during TPR1, due to the present ceria in platinum-ceria composite film. In addition there is some synergetic effect between Pt and ceria [84] in 1 nm thick Pt-CeO₂ layer

resulting in better selectivity (lower CO and CO₂ yields) during both TPR1 and TPR2 (*Fig. 62*) compared to ceria free specimen.

In this chapter we showed that the unstable catalytic behavior of Pt(1 nm)/CeO₂(10 nm)/SiO₂ sample is due to the coalescence of Pt with the following encapsulation by CeO₂ during TPR1. Regarding the Pt-CeO₂(1 nm)/SiO₂ sample it demonstrated activity and selectivity advantages over Pt(1 nm)/SiO₂. It is due to the presence of ceria in Pt-CeO₂ composite film, which protects such film from coalescence in islands, thus, the active surface area has been preserved. As a result such specimen showed 5 times more hydrogen yield. Moreover, due to synergetic of the composite Pt-ceria surface less CO and CO₂ concentrations were observed. We can conclude that adding small amounts of ceria to the 1 nm thick platinum film is a good option to improve the already high active platinum thin film catalyst for a hydrogen production via POM.

5. Conclusions

In present work two important chemical reactions were investigated: CO oxidation and oxidation of methanol. Such reactions were performed on novel REOs powder catalysts as well as on magnetron sputtered platinum based thin film samples using laboratory microreactor system. It is important that the activity tests were done at high pressure condition which is close to a real catalytic usage. Many interesting processes that occur on the surface of catalysts during the reactions are described in this work. Such investigation can be useful for industrial catalysis, which makes present thesis work more valuable.

The first part of the thesis is devoted to investigation of CO oxidation reaction on platinum thin film catalysts and nanopowder REOs. First, we performed CO oxidation reaction on Pt and PtO_x deposited on different substrates: SiO₂, G-foil and C interlayer. It was shown that the activity of PtO_x does not depend on the type of the substrate, while metallic Pt supported by G-foil and especially by C interlayer exhibited activity decrease compared to the Pt supported by SiO₂. It is due to conglomeration of Pt in islands, which resulted in opening the inert substrates, thus, a lower activity was observed. In contrary PtO_x deposited on either substrate demonstrated almost the same activity, due to the reduction of the oxide surface and forming the granular morphology, which is found to be independent of the support types. Since CO oxidation activity on Pt and PtO_x is similar, platinum oxide has an advantage such as less amount of active platinum compared to the Pt layer with the same thickness. The next chapter is about CO oxidation on REOs nanopowder catalysts. Such catalysts were prepared by a novel sol-gel method. In this case, active REOs material was dispersed within the inert alumina matrix. The best CO conversion demonstrated by ceria stabilized with alumina, due to significantly higher SSA. Moreover, the ceria content in such catalyst is 20% (wt) which is advantage from an economical point of view compared to pure ceria. Next experiments were CO oxidation study on samaria nanoparticles prepared from different precursors (Sm₂O₃, Sm(NO₃)₃ and Sm(OH)₃) and calcined at four different temperatures (500, 600, 900 and 1000 °C). All prepared samples demonstrated similar activities except Sm(NO₃)₃ calcined at 500 °C, which demonstrated relatively high CO conversion (18%). Also we observed the activity decrease on samples calcined at higher temperature, mostly due to the decreasing of surface area.

The second part of the thesis is devoted to the methanol oxidation study on platinum based thin film catalysts. First, SRM reaction on Pt, PtO_x and Pt-CeO₂ thin films deposited on SiO₂ wafer were performed. In this case activity and selectivity were better on the platinum oxide thin film (higher H₂ and lower CO and CO₂ yields), due to expected higher surface area compared to pure platinum with the same thickness. The Pt-CeO₂ thin film exhibited almost no activity, due to the weak MD process on ceria, which is an initial part of the SRM reaction. Then the POM experiments on the PtO_x and the Pt deposited on the SiO₂ substrate have been done. Activity and selectivity were better in case of PtO_x thin film. SEM and XPS analysis proved that the enhanced activity of PtO_x layer is the result of the reduction of platinum oxide to metallic platinum (Pt⁴⁺ → Pt⁰), which leads to the increasing of the surface area of such thin film. Moreover PtO_x layer is activated by the reaction mixture in the beginning of the POM reaction (it was already reduced at 150 °C). After that, we tried to improve the activity of PtO_x layer via its deposition on carbonaceous interlayers that have a high surface area. Among used interlayers PtO_x deposited on a-C_t interlayer demonstrated better activity and selectivity due to initially higher porosity of such substrate. The next experiment was POM on PtO_x thin films under different CH₃OH:O₂ molar ratios in the gas feed mixture. From these experiments, it was found that the operating with oxygen lean feed mixture (CH₃OH:O₂ – 3:1) leads to activity and selectivity advantages compared to oxygen rich mixture (CH₃OH:O₂ – 3:1). Next series of the experiments were POM on Pt-CeO₂ thin films with low (Pt/Ce = 0.15) and high (Pt/Ce = 0.56) relative atomic concentrations of platinum. POM activities of these films were compared with references, such as pure Pt and CeO₂ films with the same thickness. CeO₂/SiO₂ and Pt(0.15)-CeO₂/SiO₂ samples demonstrated weak POM activity. It is due to less intensive methanol combustion process (which is an initial part of the POM reaction) on ceria layers at low reaction temperatures (100 - 150 °C). In contrary Pt-CeO₂(0.56)/SiO₂ sample exhibits preferable yields of products over pure Pt/SiO₂ specimen (similar H₂ yield and low CO and CO₂ yields), but only in 100 - 260 °C temperature region. At higher temperatures platinum diffused inside ceria interlayer, resulting in an activity decrease. However, using the Pt-CeO₂(0.56) thin film catalyst for POM below 260 °C leads to activity and economic advantages compared to reference the Pt thin film with the same thickness. Final experiments of POM were carried on Pt(1 nm)/CeO₂(10 nm)/SiO₂, Pt-CeO₂(1 nm)/SiO₂ and reference

Pt(1 nm)/SiO₂ samples. The Pt(1 nm)/CeO₂(10 nm)/SiO₂ specimen lost its activity after the repeat of TPR procedure, due to the coalescence of active Pt in clusters with further encapsulation by ceria. Overall efficiency and selectivity of the Pt-CeO₂(1 nm)/SiO₂ sample was improved much over the reference Pt(1 nm)/SiO₂ one. It is because of the presence of ceria (Pt/Ce = 0.85) in Pt-CeO₂ composite layer, which leads to a formation of the granular structure and prevents the active Pt from coalescing into islands.

Bibliography

- [1] P. J. Kelly and R. D. Arnell, "Magnetron sputtering: a review of recent developments and applications," *Vacuum*, vol. 56, no. 3, pp. 159–172, 2000.
- [2] M. P. Seah, "A review of the analysis of surfaces and thin films by AES and XPS," *Vacuum*, vol. 34, no. 3–4, pp. 463–478, 1984.
- [3] "Experiment B1: X-Ray photoelectron spectroscopy (XPS)."[Online]. Available: http://www.physik.fu-berlin.de/studium/praktika-forward/fp_master_SoSe2011/doc/Ma4_XPS1.pdf.
- [4] I. G. Florentina and B. Ion, "The effects of air pollutants on vegetation and the role of vegetation in reducing atmospheric pollution, the impact of air pollution on health, economy, environment and agricultural sources," In *Tech*, 2011.
- [5] A. Faiz, C. S. Weaver, and M. P. Walsh, "Air pollution from motor vehicles," *The World Bank*, 1996.
- [6] J. A. Raub, M. Mathieu-Nolf, N. B. Hampson, and S. R. Thom, "Carbon monoxide poisoning - a public health perspective," *Toxicology*, vol. 145, no. 1, pp. 1–14, 2000.
- [7] Manufacturers of Emission Controls Association, "Clean air facts. The catalytic converter: technology for clean air," 2006.
- [8] M. Nishibori, W. Shin, N. Izu, T. Itoh, and I. Matsubara, "CO oxidation performance of Au/Co₃O₄ catalyst on the micro gas sensor device," *Catal. Today*, vol. 201, no. 1, pp. 85–91, 2013.
- [9] A. Szychowska, M. Wróbel-Jedrzejewska, I. Chylak, I. Kocemba, and J. Rynkowski, "Investigation of CO oxidation by NO with application of semiconductor gas sensors," *Polish J. Environ. Stud.*, vol. 17, no. 3, pp. 421–425, 2008.
- [10] D. J. Knapp, "Design and performance of a sealed CO₂ laser for industrial applications," *J. Phys. Conf. Ser.*, vol. 274, 2011.
- [11] J. J. Baschuk and X. Li, "Carbon monoxide poisoning of proton exchange membrane fuel cells," *Int. J. Energy Res.*, vol. 25, no. 8, pp. 695–713, 2001.
- [12] A. K. Santra and D. W. Goodman, "Catalytic oxidation of CO by platinum group metals: from ultrahigh vacuum to elevated pressures," *Electrochim. Acta*, vol. 47, no. 22–23, pp. 3595–3609, 2002.
- [13] N. Lopez, T. V. W. Janssens, B. S. Clausen, Y. Xu, M. Mavrikakis, T. Bligaard, and J. K. Nørskov, "On the origin of the catalytic activity of gold nanoparticles for low-temperature CO oxidation," *J. Catal.*, vol. 223, no. 1, pp. 232–235, 2004.

- [14] Y. J. Mergler, A. van Aalst, J. Van Delft, and B. E. Nieuwenhuys, "CO oxidation over promoted Pt catalysts," *Appl. Catal. B Environ.*, vol. 10, no. 4, pp. 245–261, 1996.
- [15] M. Schubert, "CO oxidation over supported gold catalysts—'inert' and 'active' support materials and their role for the oxygen supply during reaction," *J. Catal.*, vol. 197, no. 1, pp. 113–122, 2001.
- [16] P. Bera, A. Gayen, M. S. Hegde, N. P. Lalla, L. Spadaro, F. Frusteri, and F. Arena, "Promoting effect of CeO₂ in combustion synthesized Pt/CeO₂ catalyst for CO oxidation," *J. Phys. Chem. B*, no. 107, pp. 6122–6130, 2003.
- [17] P. Atkins and J. de Paula, "*Atkins' Physical Chemistry, Eighth Edition*", 2006.
- [18] R. J. Baxter and P. Hu, "Insight into why the Langmuir–Hinshelwood mechanism is generally preferred," *J. Chem. Phys.*, vol. 116, no. 11, p. 4379, 2002.
- [19] P. Mars and D. W. van Krevelen, "Oxidations carried out by means of vanadium oxide catalysts," *Chem. Eng. Sci.*, vol. 3, pp. 41–59, 1954.
- [20] P. J. Berlowitz, C. H. F. Peden, and D. W. Goodman, "Kinetics of CO oxidation on single-crystal Pd, Pt, and Ir," no. 22, pp. 5213–5221, 1988.
- [21] S. M. McClure and D. W. Goodman, "New insights into catalytic CO oxidation on Pt-group metals at elevated pressures," *Chem. Phys. Lett.*, vol. 469, no. 1–3, pp. 1–13, 2009.
- [22] M. Comotti, W.-C. Li, B. Spliethoff, and F. Schüth, "Support effect in high activity gold catalysts for CO oxidation," *J. Am. Chem. Soc.*, vol. 128, no. 3, pp. 917–924, 2006.
- [23] S. D. Lin, M. Bollinger, and M. A. Vannice, "Low temperature CO oxidation over Au/TiO₂ and Au/SiO₂ catalysts," *Catal. Letters*, vol. 17, no. 3–4, pp. 245–262, 1993.
- [24] H. P. Bonzel and R. Ku, "Mechanisms of the catalytic carbon monoxide oxidation on Pt (110)," *Surf. Interface Anal.*, vol. 33, pp. 91–106, 1972.
- [25] C. R. Henry, "Surface studies of supported model catalysts," *Surf. Sci. Rep.*, vol. 31, no. 7–8, pp. 231–325, 1998.
- [26] V. Johánek, M. Václavů, I. Matolínová, I. Khalakhan, S. Haviar, and V. Matolín, "High low-temperature CO oxidation activity of platinum oxide prepared by magnetron sputtering," *Appl. Surf. Sci.*, vol. 345, pp. 319–328, 2015.
- [27] X. Du and T. E. Graedel, "Global in-use stocks of the rare earth elements: a first estimate," *Environ. Sci. Technol.*, vol. 45, no. 9, pp. 4096–4101, 2011.

- [28] T. Mori, R. Buchanan, D. R. Ou, F. Ye, T. Kobayashi, J.-D. Kim, J. Zou, and J. Drennan, "Design of nanostructured ceria-based solid electrolytes for development of IT-SOFC," *J. Solid State Electrochem.*, vol. 12, no. 7–8, pp. 841–849, 2008.
- [29] X. Zheng, X. Zhang, X. Wang, S. Wang, and S. Wu, "Preparation and characterization of CuO/CeO₂ catalysts and their applications in low-temperature CO oxidation," *Appl. Catal. A Gen.*, vol. 295, no. 2, pp. 142–149, 2005.
- [30] B. Neumann, T. M. Gesing, A. Rednyk, V. Matolin, A. E. Gash, and M. Bäumer, "Sol–gel preparation of alumina stabilized rare earth oxo- and xerogels and their use as oxidation catalysts," *J. Colloid Interface Sci.*, vol. 422, pp. 71–78, 2014.
- [31] M. P. Rosynek, "Catalytic properties of rare earth oxides," *Catal. Rev. Sci. Eng.*, vol. 16(1), pp. 111–154, 1977.
- [32] G. Adachi and N. Imanaka, "The binary rare earth oxides," *Chem. Rev.*, vol. 98, no. 4, pp. 1479–1514, 1998.
- [33] J. Gao, Y. Zhao, W. Yang, J. Tian, F. Guan, Y. Ma, J. Hou, J. Kang, and Y. Wang, "Preparation of samarium oxide nanoparticles and its catalytic activity on the esterification," *Mater. Chem. Phys.*, vol. 77, no. 1, pp. 65–69, 2003.
- [34] G. A. M. Hussein, D. J. Buttrey, P. de Santo, A. A. Abd-Elgaber, H. Roshdy, and A. Y. Z. Myhoub, "Formation and characterization of samarium oxide generated from different precursors," *Thermochim. Acta*, vol. 402, no. 1–2, pp. 27–36, 2003.
- [35] K. Nakanishi, "Infrared Absorption spectroscopy – practical," *Holden-Day Inc.*, 1962.
- [36] J. B. Wang, W.-H. Shih, and T.-J. Huang, "Study of Sm₂O₃-doped CeO₂/Al₂O₃-supported copper catalyst for CO oxidation," *Appl. Catal. A Gen.*, vol. 203, no. 2, pp. 191–199, 2000.
- [37] J. B. Wang, D.-H. Tsai, and T.-J. Huang, "Synergistic catalysis of carbon monoxide oxidation over copper oxide supported on samaria-doped ceria," *J. Catal.*, vol. 208, no. 2, pp. 370–380, 2002.
- [38] EURELECTRIC "Preservation of Resources" Working Group's "Upstream" Sub-Group in collaboration with VGB, "Efficiency in electricity generation," 2003.
- [39] J. Larminie and A. Dicks, "Fuel cell systems explained, second edition," 2003.
- [40] EG & G Thechnical Services, Inc., "Fuell cell handbook, seventh edition," *U.S. departament of energy*, 2004.

- [41] J. O'M. Bockris, "Hydrogen economy in the future," *Int. J. Hydrogen Energy*, vol. 24, no. 1, pp. 1–15, 1999.
- [42] M. L. Cubeiro and J. L. G. Fierro, "Selective production of hydrogen by partial oxidation of methanol over ZnO-supported palladium catalysts," *J. Catal.*, vol. 179, no. 1, pp. 150–162, 1998.
- [43] S. Velu, K. Suzuki, and T. Osaki, "Selective production of hydrogen by partial oxidation of methanol over catalysts derived from Cu-Zn-Al-layered double hydroxides," *Catal. Letters*, vol. 62, no. 2–4, pp. 159–167, 1999.
- [44] F.-W. Chang, H.-Y. Yu, L. Selva Roselin, and H.-C. Yang, "Production of hydrogen via partial oxidation of methanol over Au/TiO₂ catalysts," *Appl. Catal. A Gen.*, vol. 290, no. 1–2, pp. 138–147, 2005.
- [45] C. Lee, H.-K. Yoon, S.-H. Moon, and K. J. Yoon, "Methanol decomposition over supported palladium and platinum," *Korean J. Chem. Eng.*, vol. 15, no. 6, pp. 590–595, 1998.
- [46] Z. Sio, C. Z. Sio, I. A. Fisher, and A. T. Bell, "A mechanistic study of methanol decomposition over Cu/SiO₂," *J. Catal.*, vol. 184, pp. 357–376, 1999.
- [47] Y. Matsumura, K. Tanaka, N. Tode, T. Yazawa, and M. Haruta, "Catalytic methanol decomposition to carbon monoxide and hydrogen over nickel supported on silica," *J. Mol. Catal. A Chem.*, vol. 152, no. 1–2, pp. 157–165, 2000.
- [48] J. Agrell, H. Birgersson, and M. Boutonnet, "Steam reforming of methanol over a Cu/ZnO/Al₂O₃ catalyst : a kinetic analysis and strategies for suppression of CO formation," *J. Power Sources*, vol. 106, pp. 249–257, 2002.
- [49] R. Pérez-Hernández, D. Mendoza-Anaya, A. G. Martínez, and A. Gómez-Cortés, "Catalytic steam reforming of methanol to produce hydrogen on supported metal catalysts," DOI: 10.5772/49965, 2012.
- [50] W. Cao, G. Chen, S. Li, and Q. Yuan, "Methanol-steam reforming over a ZnO-Cr₂O₃/CeO₂-ZrO₂/Al₂O₃ catalyst," *Chem. Eng. J.*, vol. 119, no. 2–3, pp. 93–98, 2006.
- [51] E. Santacesaria and S. Carrá, "Kinetics of catalytic steam reforming of methanol in a CSTR reactor," *Appl. Catal.*, vol. 5, no. 3, pp. 345–358, 1983.
- [52] J. C. Amphlett, M. J. Evans, R. F. Mann, and R. D. Weir, "Hydrogen production by the catalytic steam reforming of methanol: Part 2: Kinetics of methanol decomposition using girdler G66B catalyst," *Can. J. Chem. Eng.*, vol. 63, no. 4, pp. 605–611, 1985.

- [53] K. Geissler, E. Newson, F. Vogel, T.-B. Truong, P. Hottinger, and A. Wokaun, "Autothermal methanol reforming for hydrogen production in fuel cell applications," *Phys. Chem. Chem. Phys.*, vol. 3, no. 3, pp. 289–293, 2001.
- [54] B. A. Peppley, J. C. Amphlett, L. M. Kearns, and R. F. Mann, "Methanol–steam reforming on Cu/ZnO/Al₂O₃. Part 1: The reaction network," *Appl. Catal. A Gen.*, vol. 179, no. 1–2, pp. 21–29, 1999.
- [55] S. P. Asprey, B. W. Wojciechowski, and B. A. Peppley, "Kinetic studies using temperature-scanning: the steam-reforming of methanol," *Appl. Catal. A Gen.*, vol. 179, no. 1–2, pp. 51–70, 1999.
- [56] C. J. Jiang, D. L. Trimm, M. S. Wainwright, and N. W. Cant, "Kinetic mechanism for the reaction between methanol and water over a Cu-ZnO-Al₂O₃ catalyst," *Appl. Catal. A Gen.*, vol. 97, no. 2, pp. 145–158, 1993.
- [57] K. Takahashi, N. Takezawa, and H. Kobayashi, "The mechanism of steam reforming of methanol over a copper-silica catalyst," *Appl. Catal.*, vol. 2, pp. 363–366, 1982.
- [58] J. P. Breen and J. R. H. Ross, "Methanol reforming for fuel-cell applications: development of zirconia-containing Cu–Zn–Al catalysts," *Catal. Today*, vol. 51, no. 3–4, pp. 521–533, 1999.
- [59] T. Bunluesin, R. J. Gorte, and G. W. Graham, "Studies of the water-gas-shift reaction on ceria-supported Pt, Pd, and Rh: Implications for oxygen-storage properties," *Appl. Catal. B Environ.*, vol. 15, no. 1–2, pp. 107–114, 1998.
- [60] J. Zhou and D. R. Mullins, "Rh-promoted methanol decomposition on cerium oxide thin films," *J. Phys. Chem. B*, vol. 110, no. 32, pp. 15994–16002, 2006.
- [61] B. Aibibula and S. F. Zaman, "Gold based catalyst preparation and reaction pathway on partial oxidation of methanol to produce hydrogen reaction," *Int. J. Eng. Res. Technol.*, vol. 3, no. 12, pp. 812–814, 2014.
- [62] F.-W. Chang, H.-Y. Yu, L. S. Roselin, H.-C. Yang, and T.-C. Ou, "Hydrogen production by partial oxidation of methanol over gold catalysts supported on TiO₂-MO_x (M=Fe, Co, Zn) composite oxides," *Appl. Catal. A Gen.*, vol. 302, no. 2, pp. 157–167, 2006.
- [63] L. Alejo, R. Lago, M. A. Peña, and J. L. G. Fierro, "Partial oxidation of methanol to produce hydrogen over Cu-Zn-based catalysts," *Appl. Catal. A Gen.*, vol. 162, no. 1–2, pp. 281–297, 1997.
- [64] T. L. Barr, "An ESCA study of the termination of the passivation of elemental metals," *J. Phys. Chem.*, vol. 82, no. 16, pp. 1801–1810, 1978.
- [65] J. J. Blackstock, D. R. Stewart, and Z. Li, "Plasma-produced ultra-thin platinum-oxide films for nanoelectronics: Physical characterization," *Appl. Phys. A Mater. Sci. Process.*, vol. 80, no. 6, pp. 1343–1353, 2005.

- [66] L. Grabow, Y. Xu, and M. Mavrikakis, "Lattice strain effects on CO oxidation on Pt(111).," *Phys. Chem. Chem. Phys.*, vol. 8, no. 29, pp. 3369–3374, 2006.
- [67] J. C. Davies, R. M. Nielsen, L. B. Thomsen, I. Chorkendorff, Á. Logadóttir, Z. Lodziana, J. K. Nørskov, W. X. Li, B. Hammer, S. R. Longwitz, J. Schnadt, E. K. Vestergaard, R. T. Vang, and F. Besenbacher, "CO desorption rate dependence on CO partial pressure over platinum fuel cell catalysts," *Fuel Cells*, vol. 4, no. 4, pp. 309–319, 2004.
- [68] J. L. Gland, "Carbon monoxide oxidation on the kinked Pt(321) surface," *J. Vac. Sci. Technol. A Vacuum, Surfaces, Film.*, vol. 1, no. 2, p. 1070, 1983.
- [69] J. Shi, D. Kojima, and M. Hashimoto, "The interaction between platinum films and silicon substrates: Effects of substrate bias during sputtering deposition," *J. Appl. Phys.*, vol. 88, no. 3, p. 1679, 2000.
- [70] P. Legare, L. Hilaire, and G. Maire, "Interaction of polycrystalline platinum and a platinum silicon alloy with oxygen - an XPS study," *Surf. Sci.*, vol. 141, pp. 604–616, 1984.
- [71] A. U. Alam, M. M. R. Howlader, and M. J. Deen, "Oxygen plasma and humidity dependent surface analysis of silicon, silicon dioxide and glass for direct wafer bonding," *ECS J. Solid State Sci. Technol.*, vol. 2, no. 12, pp. 515–523, 2013.
- [72] M. Dubau, J. Lavková, I. Khalakhan, S. Haviar, V. Potin, V. Matolín, and I. Matolínová, "Preparation of magnetron sputtered thin cerium oxide films with a large surface on silicon substrates using carbonaceous interlayers," *ACS Appl. Mater. Interfaces*, vol. 6, no. 2, pp. 1213–1218, 2014.
- [73] L. Wang, Y. Song, A. Wu, Z. Li, B. Zhang, and E. Wang, "Study of methanol adsorption on mica, graphite and ITO glass by using tapping mode atomic force microscopy," *Appl. Surf. Sci.*, vol. 199, no. 1–4, pp. 67–73, 2002.
- [74] E. Schröder, "Methanol adsorption on graphene," *J. Nanomater.*, vol. 2013, pp. 1–6, 2013.
- [75] D. F. McCrede, R.W. McCabe, "Kinetics and reaction pathways of methanol oxidation on platinum," *J. Phys. Chem.*, vol. 90, pp. 1428–1435, 1986.
- [76] K. Franaszczuk, E. Herrero, P. Zelenay, and A. Wieckowski, "A comparison of electrochemical and gas-phase decomposition of methanol on platinum surfaces," *J. Phys. Chem.*, vol. 96, no. 13, p. 7, 1992.
- [77] B. A. Sexton, "Methanol decomposition on platinum (111)," *Surf. Sci.*, vol. 102, no. 1, pp. 271–281, 1981.
- [78] K. D. Gibson and L. H. Dubois, "Step effects in the thermal decomposition of methanol on Pt(111)," *Surf. Sci.*, vol. 233, no. 1–2, pp. 59–64, 1990.

- [79] V. Matolín, M. Cabala, V. Cháb, I. Matolínová, K. C. Prince, M. Škoda, F. Šutara, T. Skála, and K. Veltruská, “A resonant photoelectron spectroscopy study of Sn(O_x) doped CeO₂ catalysts,” *Surf. Interface Anal.*, vol. 40, no. 3–4, pp. 225–230, 2008.
- [80] L. S. Ferreira and J. O. Trierweiler, “Ceria in catalysis: from automotive applications to the water–gas shift reaction,” *IFAC Proc. Vol.*, vol. 7, no. part 1, pp. 405–410, 2009.
- [81] J. G. Chen, J. E. Crowell, and J. J.T. Yates, “The metal-metal oxide interface: a study of thermally-activated diffusion at the Ni/Al₂O₃ interface using electron spectroscopies,” *Surf. Sci.*, vol. 185, pp. 373–393, 1987.
- [82] R. W. Balluffi and J. M. Bkakey, “Special aspects of diffusion in thin films,” *Thin Solid Films*, vol. 25, no. 2, pp. 363–392, 1975.
- [83] M. Vorokhta, I. Matolínová, M. Dubau, S. Haviar, I. Khalakhan, K. Ševčíková, T. Mori, H. Yoshikawa, and V. Matolín, “HAXPES study of CeO_x thin film-silicon oxide interface,” *Appl. Surf. Sci.*, vol. 303, pp. 46–53, 2014.
- [84] Y. Zhang, “Effect of preparation method on platinum–ceria catalysts for hydrogen iodide decomposition in sulfur–iodine cycle,” *Int. J. Hydrogen Energy*, vol. 33, no. 2, pp. 602–607, 2008.

List of Tables

Table 1. Specific surface area of the alumina stabilized ceria and praseodymia aerogels and reference ceria and praseodymia calcined at different temperatures	29
Table 2. Methanol reforming reactions.....	41

List of Abbreviations

AC	Alternating Current
AG	Aerogel
AFM	Atomic Force Microscopy
BE	Binding Energy
BSE	Backscattered Electron
DC	Direct Current
E-R	Eley-Rideal
FC	Fuel Cell
GLAD	Glancing Angle Deposition
HC	Hydrocarbons
IR	Infrared
ND	Normal Deposition
L-H	Langmuir-Hinshelwood
MvK	Mars van Krevelen
MD	Methanol Decomposition
PEMFC	Proton Exchange Membrane Fuel Cell
PPM	Parts Per Million
POM	Partial Oxidation of Methanol
QMS	Quadruple Mass Spectrometer
RF	Radio Frequency
REO	Rare Earth Oxide
SCCM	Standard Cubic Centimeter
SE	Secondary Electron
SEM	Scanning Electron Microscopy
SOFC	Solid Oxide Fuel Cell
SRM	Steam Reforming of Methanol
SSA	Specific Surface Area
TEM	Transmission Electron Microscopy
TPR	Temperature Programmed Reaction
UHV	Ultra High Vacuum
WGS	Water Gas Shift
XPS	X-ray Photoelectron Spectroscopy